THESIS
3
0305
6220 8745

LIBRARIES
MICHIGAN STATE UNIVERSITY
EAST LANSING, MICH 48824-1048

This is to certify that the
thesis entitled

AN IN VITRO INVESTIGATION OF MC3T3-E1 OSTEOBLAST PROLIFERATION AND DIFFERENTIATION ON HYDROXYAPATITE BASED TISSUE-ENGINEERED SCAFFOLDS

presented by

Rebecca Ann McMullen

has been accepted towards fulfillment
of the requirements for the

Master of Science degree in Materials Science Engineering

Melissa Baumann
Major Professor's Signature

September 27, 2004
Date

MSU is an Affirmative Action/Equal Opportunity Institution

PLACE IN RETURN BOX to remove this checkout from your record.
TO AVOID FINES return on or before date due.
MAY BE RECALLED with earlier due date if requested.

DATE DUE	DATE DUE	DATE DUE
07 28 10		

6/01 c:/CIRC/DateDue.p65-p.15

AN *IN VITRO* INVESTIGATION OF MC3T3-E1 OSTEOBLAST PROLIFERATION AND DIFFERENTIATION ON HYDROXYAPATITE BASED TISSUE-ENGINEERED SCAFFOLDS

By

Rebecca Ann McMullen

A THESIS

Submitted to
Michigan State University
in partial fulfillment of the requirements
for the degree of

MASTER OF SCIENCE

Department of Chemical Engineering and Materials Science

2004

ABSTRACT

AN *IN VITRO* INVESTIGATION OF MC3T3-E1 OSTEOBLAST PROLIFERATION AND DIFFERENTIATION ON HYDROXYAPATITE BASED TISSUE-ENGINEERED SCAFFOLDS

By

Rebecca A McMullen

Calcium phosphate (CaP) bioceramics have long been used for bone applications. The more favored and most researched of the CaP bioceramics are hydroxyapatite (HA) and β-tricalcium phosphate (βTCP). This study details the techniques used for fabricating dense (dS) and porous foamed (pf) HA scaffolds by uniaxial pressing and foam processing, respectively, and the methods for evaluating MC3T3-E1 osteoblast (OB) proliferation and differentiation on these scaffolds. Cell proliferation was observed on both the dS and pf scaffolds over 72 hours by immunofluorescent imaging and by cell number on dS surfaces. Both approaches demonstrated decreased proliferation on dense HA compared to polystyrene (PS) control, which is consistent with findings that suggest HA suppresses OB proliferation. Differentiation was identified on day 14 by the presence of alkaline phosphatase (AP) enzyme activity on the scaffolds. By visual observation, more AP activity was observed on the dS scaffolds than the pf scaffolds. After sintering the pf scaffolds, a second phase was observed along the grain boundaries. Powder x-ray diffraction and Fourier transform infrared spectroscopy scans indicate βTCP as the nucleated second phase. Further studies are required to understand the effects of the nucleated βTCP phase on the degree and timing of OB mineralization.

I dedicate this work to my parents, Jim and Gwen McMullen for their unconditional love, encouragement and never-ending support.

In loving memory of Peg McMullen

ACKNOWLEDGMENTS

For the exhausted efforts that have been put forth to complete this thesis, it is my honor to acknowledge two distinguished faculty, Dr. Melissa Baumann and Dr. Laura McCabe, who have continuously challenged me to push the limits. A special thank you to Dr. Baumann, for your guidance and wisdom throughout this degree, and to Dr. McCabe for the insight you have provided on all my cell challenges.

With great joy I acknowledge my colleagues Ian Smith, Jackie Allar, Jeff Meganck, Sara Pschigoda, Christine Hunt, Trisha Pochert and Derek Baars. Thank you all for your support. Ian, I thank you for the discussions, and all of your help. You have always come to my aid when I have needed you most. And, who could forget your extraordinary sense of humor that always made lab experiences interesting. To Jackie, Jeff and Sara, I extend my words of appreciation to you all for the inspirational brainstorming sessions. I offer a special thanks to Christine and Trisha, for the countless hours of help with cells and in developing the tissue culture manual.

The success of my thesis would not have been possible if it weren't for Regina Irwin and Moushumi Hossain. Thank you both for the many times you have come to my rescue when there were cell issues.

A special thanks to my friends Byron and Marcia Wingerd for the many discussions and words of encouragement. You are a blessing in my life.

Nancy Albright, without you so many things would not have been possible.

And, a heartfelt thanks for the ongoing support of my parents, my brother Brian, Grandma and Grandpa Henley, Grandpa McMullen, my aunt Judy, and my friends and family!

TABLE OF CONTENTS

LIST OF TABLES

LIST OF FIGURES

Images in this thesis are presented in color

LIST OF TERMINOLOGY*

- A -

Actin – a contractile myofibril protein that binds myosin cross bridges (a protein that forms thick filaments in the muscle fibers) and is located in muscle filaments and cytoskeleton microfilaments

Alkaline Phosphatase – an enzyme uses as a osteoblast differentiation marker

Angiogenesis – the formation of new blood vessels; vascularization

Aspirate – the removal of fluid by vacuum suction

- C -

Cancellous (Trabecular) Bone – the porous, spongy bone tissue

Collar – a barrier that surrounds an engineered scaffold used to ensure cellular adherence to the scaffold surface and not the polystyrene culture well

Confluent – a condition when cells have overgrown and are running together

Cortical (Compact) Bone – dense, structural bone

Crystal Violet – an RNA stain often used to measure cell attachment and growth

Culture – the growth of living tissue cells in special medium conducive for growth
Primary culture – cells obtained by a direct transfer from a natural source to artifical medium
Secondary culture – cells derived from a primary culture
Subculture – one derived from an existing culture

Cytotoxic – an agent that possesses a destructive behavior in certain cells

- D -

Differentiation – the development of a specialized form, character or function of a cell, differing from the original type

DNA – deoxyribonucleic acid; a double-stranded helical structure composed of linked genomic sequences

Dry Mass – the mass of a scaffold free of moisture

- F -

Feed – changing old culture medium with fresh media

Foam – ceramic processing technique that uses a chemical agent to induce formation of gas bubbles and thus resulting in a porous body

- G -

Genotoxic – an agent known to be damaging to DNA, and thus causing gene mutation or cancer

Grain – an individual crystal found in a polycrystalline metal or ceramic

Green Compact – a weak ceramic scaffold where the ceramic particles have not been chemical fused by heat treatment

- H -

Hemacytometer – a tool used to count cells by phase contrast microscopy

Histology – the microscopical study of tissue structure, composition and function

Histomorphology – a qualitative study of tissue shape and structure

Hoechst – a immunofluorescent DNA stain

- I -

Immunofluorescence – method that uses specific antibodies to label with a fluorescent dye

Incubate – to place in optimal conditions for development; proper temperature and humidity for growth

In vivo – within the living body

In vitro – an artificial environment

- L -

Lamellar Bone – normal type of adult bone organized in layered lamellae

- M -

Medium (culture medium) – a nutrient substance used for the cultivation of living cells

Motility – the ability for cells to spontaneously move

- O -

Osseous – the nature or quality of bone; bony

Osteoblast – the bone cell associated with the production of bone

Osteoclast – the bone cell associated with the resorption of bone

Osteocyte – mature osteoblast trapped in the bone matrix

Osteogenesis – the development of bones

Osteoconductive – allows for bone ingrowth and vascularization of a graft

Osteoinductive – the ability to cause pluripotential cells from a nonosseous environment to differentiate and form bone

- P -

Plate – to prepare a culture medium in a culture dish

Proliferation – the reproduction or multiplication of cells

Phase Diagram – a graphical reference that depicts the chemical composition under various temperature and pressure conditions

- R -

RNA – Ribonucleic acid, single stranded nucleic acid that takes part in genetic transcription

RTPCR – Reverse transcriptase polymerase chain reaction; technique used in sequencing genes and making genetic copies

- S -

Saturated Mass – the mass of a saturated scaffold (with water) where excess water on the surface has been removed by gently rolling the scaffold on a clean Kim wipe

Seed – to add cells to culture medium

Sintering – a diffusion driven process in which chemical bonds are formed between powder aggregates, at elevated temperatures without melting

Slurry – a particle suspension in an electrolyte solution

Split – dividing the cells of a culture into additional cultures

Stain – artificially coloring a substance to aid in examination of tissues or cells by microscopy

Sub-cloning – the development of a mutant cell arising in a cell clone

Suspended Mass – the mass of a scaffold fully saturated and suspended in water

- T -

Trafficking – the communication and the movement of cell factors within the cytosol

Trypsinize – the act of detaching cells from a substrate by an enzyme that cleaves the peptide bonds; trypsin is such enzyme

- W -

Woven Bone – bony tissue found during embryonic development, the healing of fractures, and in some pathological states such as hyperparathyroidism and Paget disease.

---

* Definitions were taken from the following sources:

1. Dorlands Illustrated Medical Dictionary 29th Edition. WB Saunders Co, Philadelphia 2000.
2. Callister WD. Materials Science and Engineering, An Introduction 4th Edition. John Wiley & Sons, Inc. New York 1997.
3. Luciano VS. Human Physiology, The Mechanisms of Body Function. McGraw Hill New York. 2001
4. Merriam-Webster's Collegiate Dictionary 10th Edition. Merriam-Webster, Inc. Springfield Massachusetts 2000.

CHAPTER 1

INTRODUCTION

According to archeological findings dating as far back as the 4th and 5th centuries BC, ancient cultures have used materials such as ox teeth, shells, coral, ivory, wood and metals, to replace missing bones and teeth.[1] Today, technological advancements in materials research have opened the door to new possibilities for bone repair and replacement. These materials include metals, polymers, corals, calcium phosphates (CaP) of natural and synthetic origin, bioactive glasses, and composite materials.[1] Although some of these materials are commercially available for the use in fixation devices, total joint replacements, dental implants and maxillofacial reconstruction, they are not ideal, and are often associated with bone morbidity and fibrous encapsulation.[2]

1.1 Current Bone Substitute

Treating post-traumatic skeletal damage is a medical challenge. In some cases, realignment of the bone and the use of a fixation device is sufficient for natural healing and restoration of natural bone. However, in many cases, via injury or degenerative disease, the defect size is too great for natural healing to occur, and the use of a bone graft, or bone transplant, is needed to fill the bone defect and induce bone healing. All current bone grafts vary slightly in biological function and essential components. Allografts and autografts of either cancellous or cortical bone are currently the most predominant types of bone-grafts.

1.1.1 Allogeneic Bone-Grafting

Allograft bone is excised from cadavers, treated to remove the organic components and then used to repair extensive bone defects.[1] Allogeneic tissue is available as cortico-cancellous particulates, whole bone segments or demineralized bone matrices (DMB). Whole bone segments and cortico-cancellous particulates refer to the form in which the graft is received, as whole segments or as a finely ground particulate, respectively.

Whole bone segments are made of cortical allogeneic tissue, devoid of cells. While bone segments are osteoconductive and provide immediate structural support, they have poor osteoinductive properties, a high risk of an immune reaction and a risk of transmitting infectious diseases.[3] Whole allograft segments are preserved by deep-freezing or freeze-drying. Deep-freezing stores the graft segments at extremely low temperatures. Under these conditions, the grafts retain their material properties and can be transplanted immediately after thawing.[3] Freeze-drying incorporates a dehydration technique to preserve the graft segments.[3] However, even after rehydration, the grafts can become friable and weak in both bending and tension.[3]

Demineralized bone (DMB) matrix is one common preparation of allogeneic bone. In preparing DMB, allogeneic bone is crushed or pulverized until a uniform particle size is obtained. Refinement techniques, most of which have been patented by corporations and tissue banks, are used to demineralize the particles. These particles are then either left in the particulate form or further processed into a demineralized matrix. DMB matrices demonstrate osteoconductive and osteoinductive properties. These

matrices are quick to revascularize and are a suitable host for bone marrow, but are not structurally supportive.

Allograft tissues of all types are limited by the lack of availability, complex shapes, large sizes and high costs. Allografts, although devoid of organic matrix, are problematic, in that there is a lack of histocompatibility as well as a potential for transferring infectious diseases. [1, 3, 4]

1.1.2 Autologous Bone-Grafting

When available, autograft tissue is most commonly used. Autologous tissue has an 80 to 90% success rate with minimal risk of immune rejection.[5] This graft-tissue exhibits some osteoconductive, osteoinductive and osteogenic properties. Unfortunately, there is a limited supply of available donor tissue, and the donor sites are often associated with morbidity and long-term complications. In addition, anatomical constraints of the donor site restrict the ability to repair abnormally shaped defects and most defects requiring grafts are extensively abnormal in both shape and size.

There are two different types of bone tissues available for the use of autologous bone grafting; cortical bone and cancellous bone. Cancellous bone, or trabecular bone, is most commonly harvested from the posterior iliac crest. Bone density is a ratio of the bone mass to bone volume, and is commonly expressed as a percentage or a fraction of one. Bone porosity is denoted as one minus the density. Cancellous bone is approximately 40% dense and contains many different bone cells including osteoblasts, osteoclasts and osteocytes. Cancellous bone is quick to revascularize, resorb and is an optimal space filler under non-load bearing conditions.

Cortical bone, also referred to as compact bone, provides mechanical strength and structural support for load bearing conditions because of its 80% bone density. Cortical bone-grafts exhibit minimal osteoinductive properties but are osteoconductive and demonstrate osteogenic tendencies. Therefore, autologous cortical bone-grafts are used for large area defects that require immediate structural support.

Cortical grafts are categorized into two types; vascularized and nonvascularized.[3] Nonvascularized cortical grafts tend not to resorb or revascularize thus providing greater initial strength.[3] On the other hand, vascularized cortical grafts demonstrate limited structural support in comparison to nonvascularized grafts.[3] However, with vascularized grafts, the resorption and revascularization stimulate a faster and more natural healing process.[3] Donor sites for cortical bone include the iliac crest, ribs and fibula.[3] Although cortical bone grafts do provide limited structural support, additional support by means of either an internal or external fixation device is still required.

Although autografts are the clinically preferred donor tissue, the disadvantages include; high cost, donor site morbidity, limited availability, size limitations and trauma to the patient.[1] In addition, patients suffering from extreme bone deficiencies or degenerative bone diseases are no longer candidates for this method of treatment. Degenerative bone diseases include, but are not limited to, osteoporosis, osteogeneous imperfecta and cancer. Additionally, research has shown progressive deterioration of bone occurs with increased age.[6, 7] Osteoporosis, a serious bone disease affecting elder generations, is the result of extremely low bone density due to the loss of bone calcium. The decreasing bone density further deteriorates bone strength, making bones brittle and extremely vulnerable to fracture.[6-8] Although osteoporosis affects both genders, women

are more severely afflicted due to the hormonal changes associated with menopause.[6-10]

The clinical techniques for bone repair currently used today fail to incorporate medical treatments, which would aid in the battle of degenerative bone diseases, while simultaneously repairing the extensive defect. There is also a need to research and develop orthopaedic implants, designed to be mechanically stable, despite the harsh environmental conditions *in vivo*. With bone tissue in high demand for use in transplantations, there continues to be interest among researchers in the development of alternative solutions. Synthetically engineered bone tissue is one such promising alternative.

1.2 Tissue Engineering Bone

Engineering bone involves the successful integration of four key components: 1) an osteoconductive matrix or scaffold capable of establishing a 2) vascularized network that encourages the 3) adhesion, attachment, and migration of osteogenic cells, as well as the 4) adhesion of extracellular matrix proteins, cytoskeleton proteins and adhesion molecules.[11] These four key components will be discussed in depth. However, the focus of this paper is on the design and processing of osteoconductive CaP scaffolds, and the *in vitro* response of bone-forming osteoblast cells to these scaffolds.

1.2.1 Osteoconductive Scaffolds

Tissue engineered scaffolds have many advantages. Engineered scaffolds can be fabricated into complex shapes and sizes without the limitation of availability. These scaffolds are also histocompatible, with minimal risk of disease transmission. The ideal engineered scaffold would (1) have good biocompatibility without immunological or foreign body response,[12, 13] (2) bioactively form a direct, strong bond between the scaffold and bone, [1, 9, 12, 13] (3) consist of a 3-dimensional interconnecting network of macro- and micropores to support cell migration while facilitating bone tissue regeneration and vascularization,[1, 9, 12-15] (4) biodegrade at a rate that matches the rate of cell and tissue ingrowth,[9, 12] (5) be mechanically strong and (6) be easily fabricated.[12] Thus, there are many design parameters to consider in fabricating engineered bone tissue.

1.2.1.1 Calcium Phosphates

Calcium phosphate (CaP) bioceramics have been used for decades in many medical applications, such as implant coatings and filler materials. More recently, CaP bioceramics have shown promise as an engineered bone scaffold, an alternative to auto- or allografts. These bioceramics are biocompatible, bioactive, resorbable, and osteoconductive; they induce a positive interfacial bond and cellular ingrowth, encouraging mineral deposition and new bone formation.[1, 16] Hydroxyapatite (HA) and β - tricalcium phosphate (βTCP) are the more favored and most researched of the CaP bioceramics.[1, 9, 13, 17]

The composition and stability of CaP is greatly influenced by the sintering temperature and partial vapor pressure conditions at which the material is sintered.[13]

Under ambient conditions, HA is not stable during the high temperature phase. However, de Groot *et al.* demonstrated that by inducing a 500 mmHg partial vapor pressure of water while sintering, a pure HA phase is stable at high temperatures as a line compound. Their studies also showed that the amount of water vapor present during sintering affects the sintering temperature.[13] Therefore, under high temperature conditions, HA is usually found in the biphasic forms of HA + α-tricalcium phosphate (αTCP), HA + calcium oxide (CaO) or HA + tetracalcium phosphate (Ca_4P).

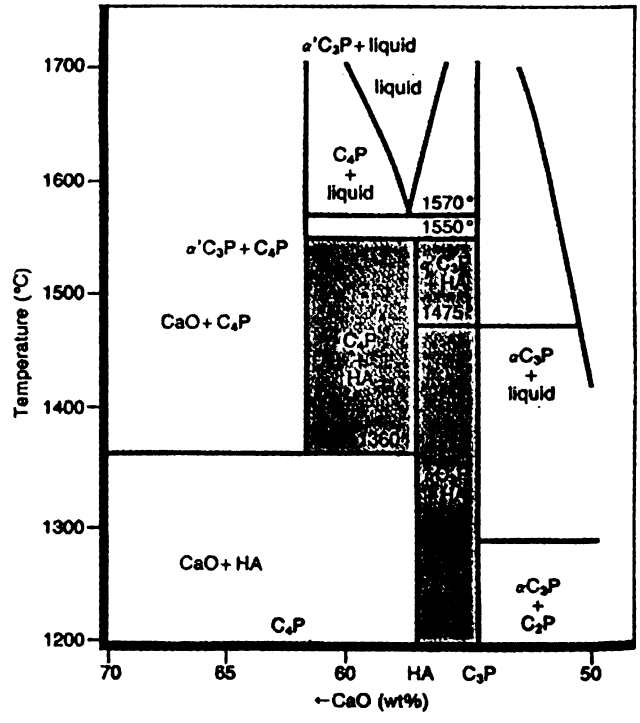

Figure 1: Calcium phosphate phase diagram in the presence of a partial pressure of water.[13]

β-tricalcium phosphate (βTCP) is not stable at high temperatures greater than 1200°C where it transforms into αTCP. At room temperature, however, HA is one of only two stable CaP phases.[13, 18] Thus, at room temperature it has been demonstrated that various CaP phases transform into HA. Fishers-Brandies *et al.* also observed the transformation

of βTCP into HA under physiologic conditions.[19] By controlling the temperature, Ca/P ratio and vapor pressure during sintering one can obtain a wide range of well-defined CaP products.[13]

Numerous sintering temperatures have been reported for HA ranging from 1100°C to 1360°C. Krajewski *et al.* established an optimum sintering temperature for HA ranging from 1100°C to 1150°C,[20] based on the presence of bone growth. Later findings by Yuan *et al.* confirmed that bone formation was found in HA scaffolds sintered at 1100°C, while only a bone-like tissue was detected in HA sintered at 1200°C.[17] Yuan *et al.* later showed HA apatite crystals to have a lower crystallinity when sintered at lower temperatures, and thus a more active bone formation.[21] Hing *et al.* concluded that changes in the degree of crystallinity and phase purity can lead to variations in the scaffold solubility.[22] It has been well established that cell proliferation, attachment, phenotypic expression and tissue response are directly influenced by the CaP composition, solubility, porosity and surface topography.[1, 23, 24] Therefore, variations in the CaP phase present have a strong influence on the cellular response.[22] Bone formation was, however, induced in HA scaffolds sintered at 1200°C when implanted in dogs.[21] Although this demonstrates that the sintering temperature has little effect in bone formation when placed *in vivo*, it is very difficult to make comparisons and draw conclusions based on the diversity of the implantation sites, implantation techniques and animal species.[23]

HA, βTCP, HA / βTCP composite referred to as biphasic CaP (BCP), and unsintered CaP, or calcium deficient apatite, are the CaP bioceramics commercially available for medical applications.[1] There are numerous techniques for processing CaP

scaffolds. Slip casting and uniaxial pressing are two common methods for processing dense CaP ceramics, which may or may not incorporate the use of a binder.[25,26] The fabrication of porous scaffolds is commonly achieved through the use of polymeric sponges, gel casting techniques or foaming agents.[17, 21, 27-30] Foaming agents include polyoxyethylene lauryl ether, $NaHCO_3$ and citric acid, $CaCO_3$ and citric acid, NH_4HCO_3 and citric acid, and H_2O_2.[17, 21, 27, 28] These polymeric foaming agents are assumed to be fully removed during the sintering process, without altering the HA characteristics.[28] However, traces of these elements or impurities within the biomaterial are potential carcinogens, and can be genotoxic as well as cytotoxic.[31] Müller *et al.* demonstrated that common chemical analysis techniques often fail to detect many impurities and trace elements therefore, understanding potential toxicities and toxic concentrations is imperative.[31]

One alternative to eliminating potential toxicities in the CaP is by fabricating scaffolds with a binderless, non-toxic foaming agent, such as H_2O_2.[21] Yuan *et al.* observed bone formation at 3 and 6 months within HA scaffolds processed in a similar manner.[21] The elimination of a toxic binder is highly favorable, and thus using H_2O_2 as a foaming agent is one of the most popular methods for porous scaffold production.[27]

1.2.1.1.1 Hydroxyapatite (HA)

Synthetic HA, $Ca_{10}(PO_4)_6(OH_2)$, commonly produced by wet precipitation synthesis, closely approximates the composition of natural bone.[1, 12, 32-36] The apatite mineral found in bone is an impure form of HA with other ions such as Mg^{+3}, CO_3^{2-} and F^- present.[16] Studies have shown that bone binds to other metals such as Al, B, Cd, Cr,

Pb, Si and Sr, and when this occurs can have multiple effects on the skeletal system.[37] Some of these effects include loss of bone mineral density and mineral content, an altered bone metabolism, a decrease in calcium adsorption and an increase in calcium resorption.[37] The effects of Ti, Co and Cr have been studied and found to increase bone cytokines, which increases the inflammatory response making them unfavorable candidates for implants.[37] To date, most metallic dental implants, total hip replacements and total knee replacements are commonly fabricated out of Co-Cr, and Ti alloys.[2] In a study conducted by Wang *et al.,* an increase in bone cytokines was found to be a potential cause of osteolysis (the loosening in total joint arthroplasty).[38] Therefore, implants designed using HA to stimulate a bioactive response, develop an adherent hydroxycarbonate apatite (HCA) layer that provides a bonding interface with surrounding tissue capable of resisting substantial mechanical forces.[39] HA is often used to coat surfaces of metallic implants to aid in the formation of a strong implant-bone tissue interface. Similarly, HA coated implants promote faster bone adaptation and reduced healing times.[32]

HA is the most stable phase of CaP, and thus *in vivo* results find a slow degradation rate via physicochemical dissolution.[15] For this reason, HA implants can be designed with a high structural integrity thus having the ability to withstand loads comparable to normal physiologic bone forces. However, a successful implant is defined as the ability of the synthetic implant to progressively regenerate into bone within normal healing time (average of 6 months). Recent research shows strong correlations between the healing time and material degradation. To achieve a structurally supportive HA implant, the implant must be manufactured to a material density of 80 to 100%. However,

at these high densities, not only is the *in vivo* degradation rate of the HA extremely slow, but there is limited cellular ingrowth, and an inconsistency of cellular growth along the bone/HA interface.

1.2.1.1.2 Tricalcium Phosphates

TCP is another favored member of the CaP family. The TCP phase is broken into two sub-phases, αTCP and βTCP. Both phases have the chemical composition $Ca_3(PO_4)_2$, differing only in their specific gravity, x-ray diffraction results (XRD) and their rates of biodegradability. αTCP is stable at temperatures above 1200°C below which βTCP is the stable TCP.[13] In addition, when αTCP was implanted in adult dogs for up to 150 days, Yuan *et al.* observed no bone formation as compared to bone formation found on HA and βTCP.[17]

βTCP is biocompatible and osteoconductive, with a Ca:P ratio of 1.5.[1] Although βTCP stimulates a limited bioactive response, it is not as stable as HA, degrades rather quickly, and is not ideal for an implant needing structural stability.[39] In addition to the lack of material strength, this rapid rate of biodegradation often occurs before the cellular components are capable of laying an organic matrix that starts the process of mineral deposition and bone regeneration. Pure βTCP bone implants are rapidly broken down by macrophages and carried away by the lymph system prior to the occurrence of bone repair.[13, 40]

The challenge at hand is to develop a scaffold that maximizes bone ingrowth and mineral deposition, while maintaining structural integrity during concurrent bone

remodeling. However, recent studies of biphasic calcium phosphate (BCP), an HA and βTCP composite, show that combining the structural properties of HA with the resorbability of βTCP results in a time controlled degradation with simultaneous regeneration of newly formed bone.[16]

1.2.1.2 Porosity

Porosity is a vital part of both cortical and cancellous bone. Although an increased porosity weakens the mechanical stability of the scaffold, pores of a specific size, shape and interconnectivity are vital for cellular adhesion, attachment, growth, migration, and overall bone formation. Interconnecting porous scaffolds provide a vascularized network that 1) allows for cellular attachment, migration, expression and ingrowth, 2) ensures adequate nutrient diffusion to the cells and 3) acts as a waste removal system.[1] Thus, porosity is a vital part of natural bone and an important design criterion for bone tissue engineering scaffolds.

There are two different types of pores that make up the total porosity; micropores and macropores. Micropores are created from an incomplete sintering of the ceramic particles and typically have a diameter less than 75 μm. Macropores, which are induced into the material to obtain a desired porosity, have a diameter of 150-400 μm and are primarily for cellular ingrowth.[39] Interconnections are the pathways between the macro- and micropores that allow for the flow of cells and nutrients, and for vascularization, thus playing a critical role in encouraging bone ingrowth.[41]

Macroporosity plays an important role in bone physiology. Cortical bone, responsible for the structural integrity of the skeletal system, has a pore size ranging from

1 to 100μm, whereas the nutrient-rich trabecular bone has a pore size ranging from 200 to 400 μm.[1] Macroporosity is also a critical factor in cell attachment, migration and growth in an engineered scaffold. A minimum pore size range of greater than 150 μm has been determined necessary for healthy and sufficient bone ingrowth.[18] Although a pore size of 10 μm allows for cell migration, a macroporosity greater than 100 μm has a direct influence on bone formation.[41] At this pore size, osteogenesis is induced and bone is able to grow into the interconnections and maintain vascularity for long-term viability.[39, 42] Pore size has been shown to affect cell/scaffold interactions; pores ranging in size from 15 to 50 μm are sufficient for fibrous tissue ingrowth.[15]

The pore size, ideal for encouraging osteoblast migration, attachment and proliferation, ranges from 100 to 400 μm.[41, 43, 44] Macropores in this size range have been shown to promote bone tissue ingrowth while providing mechanical interlocking stability.[12] Yoshida *et al.* concluded that the larger the pores, the earlier bony ingrowth will occur into the porous HA.[42] Research presented by Yuan *et al.* builds upon previous work, which notes the importance of macroporosity in new bone formation. However, Yuan *et al.*, conclude that while macro pore size is important within the range 100 – 400 μm, the critical factor in bone formation is the concomitant degree of microporosity.[21] Micropores greatly increase the surface area for protein adsorption, because surface area facilitates ion exchange.[21] With more proteins absorbed, the easier it is to form a bone-apatite layer that can in turn, facilitate bone formation.[21]

To optimize biological efficiency for bone applications, control of the mean pore and interconnection sizes is required.[43] The degree of interconnectivity is also thought to be more critical in determining bony ingrowth than macropore size.[45] Research by Flautre

et al. found an interconnection size of 130 μm promoted cellular and tissue activity inside pores.[43] If the interconnection density is too small in relation to the pore size, such that the interconnections are < 30 μm, then fibrous connective tissue invades the ceramic, without bone tissue differentiation.[43] Fibrous tissue invades and colonizes the pores at a faster rate than osseous tissue, and once fibrous tissue has invaded the pores, bone ingrowth is inhibited.[45] In a study conducted by Lu *et al.*, porous HA and βTCP scaffolds with interconnecting pores ranging in size from 30 to 100 μm were investigated. After 28 days, an interconnection size of 60 μm was most frequently observed in both HA and βTCP scaffolds.[41] In the same study, HA and βTCP scaffolds were implanted in rabbits for 12 and 36 weeks.[41] The degree of vascularization was higher in βTCP than HA, and the mean size and density of the interconnections significantly increased with time.[41] Thus, for resorbable materials, the pore and interconnection density plays a more critical role than pore size, because over time, the pore sizes are modified by scaffold degradation.[41]

Porous ceramic implants are advantageous because of their material inertness combined with their ability to form a mechanically stable interface as bone infiltrates the pores.[9] There have been a number of studies dealing with the ideal pore morphology for bone ingrowth and based on the results, one can conclude that the microstructure of the porous scaffolds (volume, density, pore size, grain size, interconnections and surface topography) plays an important role in the mechanical strength, degradation and bony ingrowth of the material.[41]

1.2.1.3 Mechanical Properties

Biomaterials, such as titanium alloys and stainless steels, used for many bone and joint applications have mechanical properties far superior to those of bone.[46] However, based on Wolff's Law, stress shielding, caused from implants having much greater mechanical strengths, results in bone resorption, and is therefore not conducive to implant longevity.[37] There continues to be a need for further research as to the design of biomaterials with mechanical properties closely matched to those of bone and with the capacity to be bioactive and stimulate bone ingrowth.[46]

The mechanical strength of the engineered matrix is dependent on the total volume of micropores and macropores. Porous ceramic implants are brittle so with a conflicting need for both porosity and mechanical strength, there is limited use for porous scaffolds when used in load bearing situations, unless sufficient surgical stabilization is also present.[12] Ryskewitch demonstrated with a simple exponential equation (Equation 1) that an increase in porosity results in a rapid decrease in the mechanical strength of the material.[39]

$$\sigma = \sigma_0 e^{-cp}, \quad (1)$$

were σ is strength, σ_o is strength at zero porosity, c is constant and p is porosity.[39] de Groot later developed equations for both the compressive (Equation 2) and tensile (Equation 3) strengths of porous HA and βTCP,

$$\sigma_c(V_p) = 700\, e^{-5Vp}\ (\text{MPa}) \quad (2)$$

relating the compressive strength (σ_c) to the exponential of the total volume occupied by both micro- and macropores (V_p), and the tensile strength to the microporosity volume (V_{mp})

$$\sigma_t(V_{mp}) = 220\, e^{-20 V_{mp}}\ (\text{MPa}).^{10, 13, 39} \quad (3)$$

Both the compressive modulus and ultimate compressive strength are highly sensitive to the density and pore isotropy.[45] Hing *et al.* characterized porous HA and found the mechanical properties of porous synthetic HA to be highly dependent on how it was processed and the final microstructure.[22]

Cortical bone is reported to have a mechanical strength ranging from 69 to 110 MPa, and an elastic modulus ranging from 12 to 18 GPa.[1, 47] These values are often used as a guideline when modeling engineered bone after cortical bone. Jarcho *et al.* reported that the mechanical strength of dense HA ranges from the 79 to 106 MPa.[48] The same study suggests the strength of porous HA needs to approximate 42 MPa. However this value is expected to vary significantly depending on the degree of porosity, the pore size, shape and the pore distribution.[1, 48] Metsger and co-workers also demonstrated a significant decrease in the ultimate compressive strength of HA when porosity was incorporated into the scaffold. Dense HA was found to have an ultimate compressive strength of 70 MPa, where a 50% porous scaffold resulted in an compressive strength of only 9.3 MPa.[49] As evident from this work, porous scaffolds are often not mechanically strong enough for load bearing applications, unless additional surgical stabilization is present.

In an attempt to engineer stronger scaffolds, many groups have experimented with HA composites. HA and bioglass composites have been shown to demonstrate flexural

strength and fracture toughness. Roeder *et al.* incorporated single crystal whiskers into the scaffold as another way to increase strength, while Barralet *et al.* varied the sintering atmosphere to tailor the HA microstructure.[42, 50-53]

Bone is composed of 65% inorganic matrix (bone mineral apatite), and 35% organic matrix (collagen, cells, proteins etc.).[1] Clarke and co-workers fabricated composite scaffolds incorporating organic collagen and calcium phosphate with material properties similar to those of bone.[46] When SerP, a bone specific phosphoprotein, was added to the composite scaffold, the ultimate tensile strength of the composite was further enhanced.[46] Enhancing mechanical strength of an implant by incorporating an organic matrix into the osteoconductive scaffolds is a promising step in the design and development of tissue engineered bone.

1.2.1.4 Resorption

Even the incorporation of an organic matrix will fail to enhance the mechanical strength of aging porous ceramic scaffolds due to *in vivo* environmental conditions. Therefore, to optimize the long-term success of an engineered porous bone scaffold, and to accommodate the inevitable aging process, designing the bone implant to naturally resorb back into the body would be beneficial.[4, 16] Ideally, the designed degradation of the engineered scaffold would be a time-controlled process that simultaneously replaces the resorbed material with newly formed bone.[16] Although, completely resorbable scaffolds are ideal, the challenges include matching the resorption rate to the body tissue repair rate, and maintaining the scaffold strength and stability.[39]

The breakdown of an engineered scaffold occurs by 1) physical dissolution of the material based on material solubility, which is influenced by the composition and material characteristics (porosity, surface area, crystallinity, surface topography and particle size) and 2) biological degradation, a cell mediated degradation based on environmental conditions, such as pH fluctuations and metabolic activity.[1, 15, 41] Governed by the material solubility, physicochemical dissolution initiates at the neck region of the sintered powder.[13] In addition to dissolution at the neck region, Koerten and co-workers observed degradation and crack formation at the grain boundaries.[54]

The small, degraded particles, generated from either physicochemical dissolution or biological degradation, are often digested intracellularly or carried away to neighboring tissues such as the lymph nodes. Therefore, resorbable materials must be metabolically acceptable in order for large quantities of the resorbed material to travel through the critical organs and systems of the body.[39]

In an extensive review on bioceramics, Hench discussed how relatively small changes in composition of a biomaterial can dramatically affect whether it is bioinert, bioactive or bioresorbable.[39] This was consistent with the findings of Yong *et al.* in that highly crystalline bioceramics are extremely slow to resorb, often considered non-bioresorbable.[12] Sintered synthetic HA is a highly crystalline bioceramic and in a study conducted by Doi *et al.*, the resorbability of dense HA and sintered carbonate apatite was compared to the resorbability of bone apatite.[55] The dissolution behavior of these materials, investigated under acidic conditions, (pH 5.0 at 37°C), established similar composition changes between bone apatite and sintered carbonate apatite over the same

time frame.[55] When these materials were subjected to neonatal osteoclasts, resorption was observed on the bone apatite and sintered carbonate apatite, but not on the HA.[55]

Lu *et al.* investigated the biodegradation mechanisms of CaP bioceramics, and found *in vivo* biodegradation to be rapid for βTCP and CaP bone cement, but slower for HA scaffolds.[56] Their research concluded that newly formed bone was in direct contact with HA and βTCP bioceramics at 3 weeks, and there was no direct contact with the bone cement.[56] Another study conducted by Wiltfang *et al.* found the *in vivo* resorption of βTCP and αTCP to be comparable; although αTCP was associated with an inflammatory cellular reaction.[57] It has been demonstrated that βTCP tends to resorb faster than HA. Biphasic calcium phosphate bioceramics (BCP) incorporate the favorable resorption properties of βTCP with the mechanical strength of HA, and, as seen by LeGeros and de Groot *et al.,* who with slight adjustments in the HA to βTCP ratio, controlled the biodegradation of BCP scaffolds.[1, 13] Ito and co-workers enhanced the scaffold strength while decreasing the resorbability and solubility of βTCP by binding zinc ions to the βTCP powder.[58] Zinc, an essential trace element, has been shown to promote bone formation *in vitro* and *in vivo*, and inhibit osteoclastic bone resorption *in vitro* when zinc containing βTCP was cultured with cells.[58]

The surface area to volume ratio of the engineered scaffold also influences the rate of degradation.[13] After long periods of time *in vivo*, biological conditions contribute to the resorption of the material and thus small amounts of degradation can lead to a large increase in surface area. Degradation of the ceramic scaffold materials occurs quicker with a larger surface area, therefore porous scaffolds tend to degrade more rapidly than dense scaffolds. The ideal bone implant would be designed with a degradation rate timed

with the rate of new bone regeneration therefore not sacrificing mechanical properties. Although research shows surface area plays an important role in scaffold degradation, it is a pivotal property, along with other surface properties, that governs the incorporation of an organic matrix.

1.2.1.5 Surface Properties

Material surface properties of engineered scaffolds, such as surface area, surface roughness, surface chemistry, surface charge and grain size, play a critical role in the adhesion of proteins, growth factors, amino acids and other biochemical factors, when placed either *in vitro* or *in vivo.*[10] The adhesion of these proteins, growth factors, amino acids, and biochemical factors prepare the scaffold for cellular adhesion, which in turn affects the tissue architecture, cell migration, proliferation, differentiation, motility and trafficking. Subtle changes in surface topography, surface chemistry and surface energy are detectable on a cellular level and can have significant variability in cell adhesion, migration, growth etc.[4]

1.2.1.5.1 Surface Topography

Surface topography is a term used to encompass the physical surface characteristics such as surface roughness, surface area and grain size. These are all important factors that directly affects the cellular response.[59-69] Deligianni *et al.* investigated human bone marrow cells on HA discs polished with SiC paper (180, 600 and 1200 grit), and found cell adhesion, proliferation and detachment strength were improved as the surface

roughness increased.[62] This cellular behavior was also noted on Ti surfaces with an increasing surface roughness.[65-67] Cells cultured on both HA and Ti surfaces, polished unidirectionally with coarse paper, would attach to the scaffolds orientated within the parallel grooves of the polished surface, whereas the cells cultured on sandblasted surfaces showed no particular orientation.[59, 63, 65] When comparing the unidirectionally polished surfaces to sandblasted surfaces, Anselme *et. al* observed a lower cellular adhesion and proliferation on the sandblasted surfaces. In addition, the cells cultured on the sandblasted surfaces failed to reach confluency during the course of the study as compared to the polished surfaces. Boyan *et al.* also observed the cell numbers to decrease with increasing surface roughness, but found alkaline phosphatase activity and osteocalcin production (markers of osteoblast differentiation, Refer to 1.2.2 Osteogenic Cells) to increase significantly with an increase in surface area when cultured *in vitro* on Ti.[65]

In comparison to a flat, polished surface, increasing surface roughness also means an increase in surface area, and thus an improvement in both short and long-term cellular response is attributed to a greater adsorption of adhesive molecules and proteins. Sisk and co-workers demonstrated an increase in transforming growth factor-β1 (TGF-β1) production in cells cultured on rougher surfaces as well as a greater percentage of the TGF-β1 stored in the ECM.[70] After culturing J774A.1 murine macrophage cells on commercially pure Ti of various surface roughness, Takebe *et al.* observed an increase in bone morphogenetic protein–2 (BMP-2) expression with an increase in surface roughness.[60] It is also believed that the responsiveness of some osteoblast cell lines to

hormones and integrins is mediated by an increase in surface roughness.[65] These adhesive biomolecules will be discussed in detail later on.

Webster *et al.* postulated that surface grain size on nanophase ceramics is an important surface feature for the adsorption of proteins that enhances osteoblast adhesion.[71] They found an increased osteoblast adhesion on nanophase HA with an averaged grain size of 67 nm when compared to two conventional processed HA powders (via precipitation method stirred at 90°C for 1 and 3 hours) with an averaged grain size of 132 and 179 nm, respectively.[71] Osteoclasts were also shown to increase adhesion to both alumina and HA nanophase grain sizes (<100 nm) as compared to conventional HA powders.[24] In addition, both nanophase alumina and HA demonstrated a statistically significant (p<0.01) increase in concentrations of vitronectin and denatured collagen.[71] Fibronectin and albumin concentrations were found to be similar for both nanophase and conventional of both alumina and HA.[71]

Cell orientation and cell morphology are also affected by surface topography. Cellular orientation is most noted when the surface has been prepared with grooves of varying sizes. Anselme *et al.* investigated the effect of grooved titanium on osteoblast cell growth finding the grooved surface with the greatest R_a (surface roughness parameter) value, but with a small microroughness within the grooves of 10-100 μm to have the greatest orientation of osteoblasts.[72] Lu and co-workers also analyzed the effects of osteoblast behavior on microgrooved surfaces.[73] Both HA and titanium surfaces grooved with identical micropatterns of six different widths (4, 8, 16, 24, 30 and 38 μm) and three different depths (2, 4, and 10 μm) were studied.[73] Although they found no

significant differences in the orientation angle of the various microgrooved surfaces, significant cell morphology changes were observed.[73]

Cell morphology involves alterations to cell size and cell shape as a result of the surrounding environment. The cellular skeleton consists of actin filaments, providing the cell with structural stability and support. Takebe *et al.* observed an increase spreading of J774A.1 murine macrophage cells with an increase surface roughness.[60] This follows the findings of Wojciak-Stothard *et al.* that the amount of F-actin present within a cytoskeleton increases with an increased roughness, resulting in rapid cellular shape changes.[74] These results parallel the findings of Lu and co-workers when investigating microgrooved HA and titanium. The greater the groove depth and narrower the width, the stronger the effect on the SaOS-2 cell shape, whereby the cells demonstrated a greater elongation along the HA or Ti groove.[73] The importance of cell shape has been attributed to other cell functions such as growth, gene expression, protein secretion, and metabolic functions.[75]

Although only a few cellular reactions were discussed as a result of surface topography, such as increased adhesion, morphology changes, cytoskeletal changes, and orientation, surface topography can encourage other cellular reactions as well.[11, 60, 62, 71-77] Some of these reactions include, alteration in gene expression, acceleration of cellular migrations and activation of phagocytosis.[76] While all these reactions are governed by surface topography, many are also governed by surface chemistry, surface charge and surface energy.

1.2.1.5.2 Surface Charges

Surface charges play an important role in bone-implant interfacial bonding. Although their role is not well understood, research suggests a correlation between these electrical signals and the regulations of new bone formation and remodeling.[78, 79] Zeta (ξ) potential, often measured by particle electrophoresis, is the charge interactions between particles, and is directly related to surface charge.[78, 80] ξ-potential measurements are one exception to studying the interactive mechanisms of bioactive ceramics and surrounding tissues and fluids *in vitro*.[81] It has been hypothesized that the ξ-potential of bioactive ceramics was related to the surface reactivity, a governing factor in the material osteoconductivity.[81] Ducheyne *et al.*, demonstrated that the ξ-potential was related to the surface reactivity of the bioceramic, observing significant variations between stoichiometric and Ca-deficient hydroxyapatite.[81] However, it was Kowalchuk *et al.*, that confirmed the relationship between surface reactivity and osteoconductivity when in the presence of bone extracellular fluid.[78] It has been suggested that the relationship between the surface reactivity and osteoconductivity is a result of the electrokinetic potential produced when bone extracellular fluid flows along charged surfaces, and thus encouraging bone growth.[81-83]

Others have taken a more direct approach to studying the affects of surface charge by polarizing scaffold surfaces. Ueshima *et al.* cultured bacteria, *staphylococcus sp* and *Escherichia coli (E. coli),* on electronically polarized HA discs.[84] Some bacteria are known to adhere to implant surfaces, coating them with secretions that hinder the natural defense system to fight off infections, and decrease the effectiveness of the antibiotics. A study conducted by Ueshima *et al.* indicated bacterial adhesion for both bacteria, was

accelerated on the negatively charged surface (N-surface) and decelerated on the positively charged surface (P- surface).

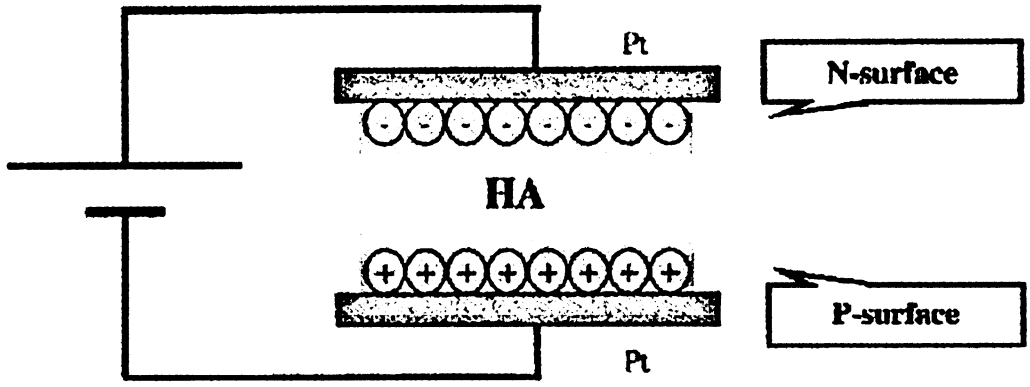

Figure 2: Schematic setup for polarizing HA disc.[84]

The surface charges have been shown to affect cellular and protein adhesion. Ohgaki *et al.* investigated adhesion of 1) L929, mouse derived connective tissue cells, 2) MC3T3-E1, mouse-derived bone forming osteoblast cells, and 3) SK-N-SH, human-derived neuroblastoma cells, to electronically charged HA thin films and HA ceramics.[85] Electronically charged thin films were advantageous in this study because they allowed for direct observation of the cells via a phase contrast microscope. Similar to the bacteria study; the N-surface induced both adhesion and growth of L929, MC3T3 E1 and SK-N-SH cells. The polarization of the N-surface not only affected the cellular adhesion but also contributed to highly orienting the SK-N-SH cells. The P-surface was shown to inhibit cell growth of all three types of cells.

In contrast, Kobayashi *et al.* and Nakamura *et al.* investigated the *in vivo* cellular response to polarized HA scaffolds.[86, 87] Scaffolds were implanted in the femoral and tibial diaphyses of male beagles and harvested at 3, 7, 14 and 28 days. Kobayashi *et al.*,

having investigated only the negatively charged surfaces, observed that the negative surfaces directed the new bone to arrange into highly oriented layers, in addition to enhancing protein and cellular adhesion.[86] Carrying this study one step further, Nakamura *et al.* investigated both the negative and positive surfaces *in vivo,* where it was found that both surfaces enhance bone deposition, thus suggesting that the polarized surface charge, regardless of polarity, promotes bone ingrowth and initiates bone reconstruction.[88]

Biochemical factors are also influenced by the surface charge and are critical for cell adhesion. Calcium (Ca^{2+}) and Sodium (Na^{+}) are key ions in cell-cell junctions (intercellular communication junctions). These junctions influence cellular adhesion and growth. Ca^{2+} and Na^{+} ions increased on a negatively charged matrix surface.[85] These ions assist in cell-to-cell interactions and could explain why there is a greater proliferation of cells on the N-surface. Ca^{2+} also attracts cell adhesive proteins such as fibronectin, osteonectin and integrins. Anionic groups such as HPO_4^{2-}, which are attracted to the P-surface, act as anti-adhesive molecules.[85]

Although the work done using polarized HA surfaces is interesting, it fails to explain the molecular interactions between the bioceramics and the surrounding fluids, a governing factor in the adhesion of cells. In addition, HA is naturally associated with a negative charge, and researchers have demonstrated the osteoinductive and osteoconductive properties of HA.[1, 9, 13, 17, 39, 89] HA not only has shown to encourage cellular adhesion, but also accelerates cellular differentiation, the early stage of mineral deposition. Therefore, studying the interactive mechanisms of bioactive ceramics to the surrounding tissues and fluids, by understanding ξ - potentials, is needed to better grasp the importance of and the effects of surface charge as an implant design criterion.

The design of the osteoconductive matrix plays an important role in cellular adhesion and tissue response. Therefore, designing a scaffold to accommodate all the critical material characteristics, composition, porosity, pore size, resorption, surface topography and surface energy, is complex and challenging, and many of the factors are not well understood. However, with the addition of osteogenic cells to the osteoconductive scaffold, there are even more factors that are not well characterized. It has been clearly shown that the addition of these cells enhances new tissue formation and improves implant longevity.

1.2.2 Osteogenic Cells

There is a continuous turnover of bone coupled by a reaction between the two main cellular systems found in bone; bone-resorbing osteoclasts and bone-forming osteoblasts. Although the physiological interactions of both of these systems are closely related, they have distinctly separate origins. Osteoblasts originate from the bone marrow mesenchymal cell lineage and osteoclasts originate from hempoietic cell lineage.[37] Osteoclasts play an important role in the resorption of biodegradable, engineered scaffolds, but it is the osteoblasts and osteoblast precursor cells that facilitate the generation of new bone tissue.[90]

All cells originate from a stem cell. Stem cells are defined as a cell with self-renewal capacity and the ability to repopulate into any cell lineage.[10] However, Morrison *et al.* noted that the recent definition of a stem cell has become more ambiguous because different people are giving it distinctive meanings.[91] In the hierarchy of cell differentiation, true stem cells differentiate into multipotential or precursor cells, which

are restricted to bi- or tripotential differentiation, and in turn, restricted to monopotential progenitors. Today, multipotential cells are often erroneously referred to as stem cells. The so-called mesenchymal stem cells (MSCs) are such an example. These multipotential cells are capable of differentiating into multiple cell phenotypes including osteoblasts, keratinocytes, chondroblasts, myoblasts and adipocytes.[10, 34, 92] Originating from the bone marrow stroma that has differentiated along osteogenic pathways, committed osteopregenitor cells are restricted to the development of osteoblasts and the formation of new bone tissue.[10, 93]

There are many different osteoblast precursor or osteoblast cell lines used in research. Primary cells are directly obtained from the source by enzymatic digestion. Often multiple cell types are collected when obtaining primary cells. Therefore, specific cell types must subsequently be isolated and sub-cultured. Cell lines are secondary cultures derived from a primary culture. The majority of the osteoblast cell lines originate from isolations of fetal or newborn rodent or chick embryonic calvariae.[10] The ability to proliferate the osteoblasts into large cell cultures is one advantage to using fetal or newborn animal osteoblasts. Another advantage of using fetal or newborn animal osteoblasts is the low numbers of chondrocytes present in calvariae membranes. The disadvantage to using these cells however, is the behavior of the osteoblasts from immature animals may not be representative of adult human osteoblast behavior.

There are many different osteoblast-like cell lines. Some of the common mouse derived cell lines include MC3T3-E1 cells (derived from newborn mouse calvariae), murine KUSA/A1, and KS483 (mouse preosteoblastic subclone).[10, 87, 94-96] MC3T3-E1 is an osteogenic cell line that shows the characteristics of immature committed osteoblasts,

identifiable by the expression of characteristic osteoblast markers under specific conditions.[10] Noted for their high alkaline phosphatase activity in the resting state, MC3T3-E1 cells also express bone sialoprotein and osteocalcin in advanced differentiation stages.[10, 87] KS483 cells, another mouse osteogenic subclone, are noted for their tendency to secrete vascular endothelial growth factor–A (VEGF-A) in a differentiation-dependent manner.[96] SaOS-2 and MG63 are commonly observed human osteoblast-like cell lines.[10, 97, 98] Others have reported using K8 cells (derived from a murine osteosarcoma) or UMR106.01 (isolated rat osteosarcoma).[10, 99] These cells are obtained from malignant tissue and therefore may also be misrepresentations of normal human, adult osteoblast behavior.

Osteoblast development has been well characterized as having various stages of proliferation and differentiation along with several well-established markers to indicate these stages. The development sequence for an osteoblast is depicted below.

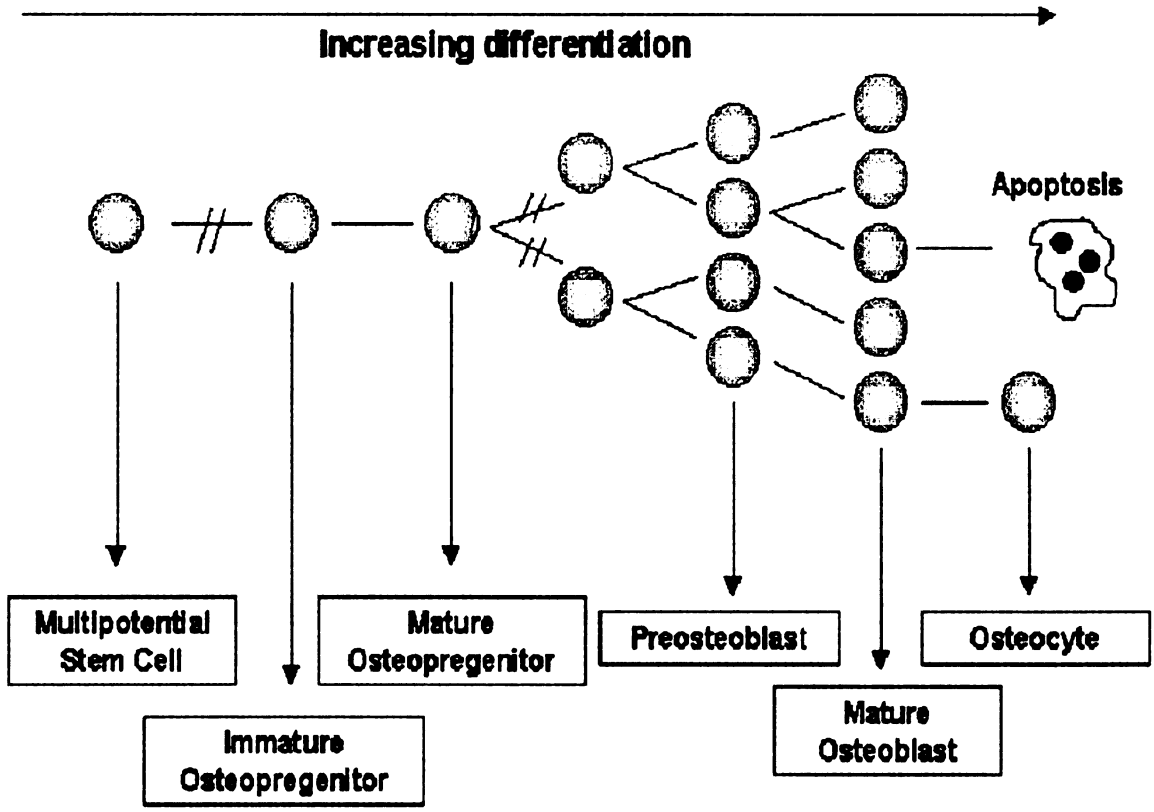

Figure 3: Osteoblast development sequence.[10, 37]

In vitro primary cultures require a stimulus, such as dexamethasome, to differentiate immature osteopregenitor cells. The deposition of Type 1 collagen is one of the earliest known osteoblast markers observed as early as the osteopregenitor stages and continues through development of a mature osteoblast.[37] The early stages of osteoblast growth are thought to be suppressed on HA and TCP scaffolds due to an increased synthesis of prostaglandin-E2.[23, 26] Cerroni and co-workers also showed a reduction in the proliferation of MC3T3-E1 cells on coralline HA.[15]

Alkaline phosphatase (AP) enzyme is another common marker of osteoblast differentiation, commonly observed during the preosteoblast and mature osteoblast stage. Regulated by factors that affect cells both genomically and non-genomically, AP activity

increases during osteoblast maturation and then decreases after the onset of mineralization.[23, 37] Various levels of AP activity are believed to reflect different degrees of differentiation.[23] HA and TCP are believed to accelerate osteoblast differentiation, as seen by an early increase in AP activity.[23, 26] Although AP staining is a widely accepted method for identifying mature osteoblasts, recent findings suggest AP activity is not as stage specific as previously suspected.[37] Osteocalcin is a protein only produced in mature osteoblasts and thus is often considered a better marker for mature osteoblast differentiation.[37]

Osteoinduction is the ability to cause multipotential cells from a non-bony environment to differentiate into bone-forming osteoblasts.[4] There is much discussion on whether CaP bioceramics are osteoinductive, with many suggesting these biomaterials are not, although recent findings suggest some CaP bioceramics are osteoinductive, and osteoinductive tendencies might be an intrinsic property of CaP biomaterials.[1, 21, 90, 100] However, osteoinductive properties can be inducted in CaP biomaterials with the addition of osteogenic cells, growth factors, and bone morphogenic proteins (BMPs), which have shown to play an important role in reconstructing bone defects.[21, 101]

1.2.3 Biological Molecules

The term cellular 'adhesion', when discussed in relation to biomaterials incorporates the attachment phase and the adhesion phase. The attachment phase is a short-term, rapidly occurring linkage that forms between the cells and the biomaterial. These physicochemical bonds commonly occur by ionic and van der Waals forces.[11] The physicochemical bonds formed during the attachment phase are highly dependent on the

material surface properties including surface chemistry, surface roughness, surface energy and charge, as well as the scaffold porosity.[11, 41, 59, 68, 71, 102] Webster and co-workers demonstrated that nanophase biomaterials, with a grain size <100 nm, increased the adhesion of osteoblasts.[71]

The adhesion phase is a longer-term occurrence involving biological molecules such as extracellular matrix proteins, cell membrane proteins and cytoskeleton proteins. These biological molecules promote the action of transcription factors that regulate gene expression by interacting with each other and inducing signaling transduction pathways.[11] It is the signaling occurring within and between the cells that begins the formation of the organic matrix of bone.

1.2.3.1 Extracellular Matrix Proteins

Bone is comprised of both an organic and inorganic matrix. The inorganic matrix primarily consisting of crystalline hydroxyapatite, makes up 60 to 70% of the bone weight.[37] The remaining 30 to 40% of the bone weight comes from the organic matrix, also referred to as the extracellular matrix (ECM).[37] The ECM found in bone is composed of both collagenous and non-collagenous proteins. The collagenous proteins are comprised of 90% ECM, of which type I collagen is the most abundant (97%).[11, 37] The remaining 3% is composed of type IV collagen.[11] Collagen is a gelatinous, structural protein that exhibits a triple-helix confirmation.[103] Non-collagenous proteins make up the remaining 10% of the extracellular matrix, which consist of osteocalcin, osteonectin, bone sialoproteins, proteoglycans, osteopontin, fibronectin, growth factors (GF) and bone morphogenic proteins (BMPs).[11] Most of these osteoblast-produced proteins play a role

in the adhesion of cells to biomaterials. In addition, the survival of the osteoblast is dependent on the GF associated with the ECM.[104]

Biomaterial characteristics play an important role in the adhesion of biomolecules. Surface characteristics govern not only how biomolecules adhere, but also the orientation of the absorbed molecules.[44] CaP biomaterials have a high affinity for these proteins, absorbing statistically larger quantities than Ti or stainless steel implants, making these biomaterials ideal carriers of extracellular proteins.[14, 32] In addition, Yuan *et al.* demonstrated that the more proteins absorbed into the biomaterial surface, the easier it was to form an apatite layer and possibly facilitate bone formation.[4]

BMPs are a part of the larger transforming growth factor β (TGF-β) superfamily. There are many different types of BMPs. However, BMP-2, BMP-4 though BMP-7 and BMP-9 are believed to be bone-inducing molecules. RhBMP-2 (recombinent human BMP) is believed to be involved in inducing differentiation of osteoblast precursor cells into mature osteoblast-like cells.[14]

1.2.3.2 Cell Membrane Proteins

The adhesive properties of many of the extracellular proteins have been attributed to the Arg-Gly-Asp (RGD) amino acid sequence.[19, 37, 67] This sequence is specific to extracellular membrane proteins and is recognized by cell membrane receptors. There are four main families of cell membrane proteins; integrins, cadherins, selectins, and immunoglobulins.[11, 37, 67, 105] Of these four main families, only the role of integrins and cadherins are currently understood, with respect to osteoblastic cells. However, selectins and immunoglobulins are believed to play a role in the cellular adhesion.

Integrins are cell-to-substrate adhesive molecules that form receptors for biomolecules like fibronectin, osteopontin, bone sialoproteins, thrombospondin, type I collagen and vitronectin. Integrins are central players for many adhesion related occurrences.[37, 105] These structurally related molecules are also responsible for connecting to the cell scaffolding and cytoskeleton. Consisting of two protein subunits, the alpha (α) and beta (β) chains span the cell membrane so that parts of each protein sub-unit protrudes from the cell to collaborate with ligands and other biomolecules to form receptors with the substrate, through focal adhesions (cytoskeletal proteins discussed in 1.2.3.3).[37, 105] Parts of the alpha and beta chains also extend into the cell cytoplasm, anchoring to the cell cytoskeleton, and causing the cytoskeleton to organize and take on a definite structure.[67] Integrins consist of 16 known alpha sub-units and 8 known beta sub-units, forming a total of 22 known integrins.[67] $\alpha5\beta1$, an integrin sub-unit, was one of the first adhesion receptors to be discovered.[32] This sub-unit binds to the fibronectin ligand and the RGD amino acid sequence, and is known to enhance osteoblast differentiation.[37] $\alpha v\beta3$, a vitronectin receptor, plays a key role in osteoclast adhesion, but is also believed to have some effects on osteoblast adhesion.[32, 37] $\alpha1\beta1$, $\alpha2\beta1$, $\alpha3\beta1$ integrins are expressed by osteoblast cells and bind to collagen ligands. Of these integrins, $\alpha2\beta1$ is associated with osteoblasts differentiation and $\alpha3\beta1$ is associated with the adhesion to collagen, fibronectin, and extracellular matrix proteins that are expressed by osteoblastic cells.[37]

Cadherins, Selectins and Immunoglobulins (Ig) are nonintegrin molecules that are responsible for most cell-to-cell adhesion interactions.[37, 105] Cadherins formed from single chain transmembrane glycoproteins, are an intricate part of adherens junctions, anchoring

junctions formed between tight junctions and desmosomes through the cytoskeleton.[37] Cadherins are calcium-dependent molecules that are often linked to the differentiation or commitment of specific cell phenotypes.[11, 37] Osteoblast, and osteoblast-derived cells express a selected group of cadherins; N-cadherins, cadeherin-4, cadeherin-6, cadeherin-11.[37] N-cadherin (Ncad) and Cadherin-11 (cad11) are the major cadherins present in bone-forming cells, and more specifically they are regulated upon the commitment of progenitor cells to the osteogenic pathway. Once committed however, the cadherins do not change with cellular differentiation.[37]

Immunoglobulins (Ig) are receptors organized in a scaffolds-like sheet consisting of folds of 70-100 amino acids.[37] Although these nonintegrin molecules are not well understood, there is data suggesting molecules from the Ig are in some way linked to osteoblast cells.[37] Within the Ig family, intercellular adhesion molecule-1 (ICAM-1) and vascular cellular adhesion molecule-1 (VCAM-1) are both linked to osteoblasts through ligands present on leukocytes, leukocyte function-dependent antigen-1 (LFA-1) and $\alpha 4$ integrins, respectively.[37] It is suggested that the potential functions of these Igs are linked with osteoblast differentiation.[37]

Selectins are a family of glycoproteins consisting of E-selectin, P-selectin and L-selectin.[37] E- and P-selectin are expressed in endothelial cells and it is believed that both E- and P-selectin are not key players in osteoblast adhesion or development.[37] However, L-selectin is expressed in human mesenchymal cells, a cell type capable of deriving into an osteoblast cell.[37] For this reason, there is speculation that L-selectin might play a role in osteoblast adhesion or development, but their function is unknown at this time.[37]

1.2.3.3 Cytoskeleton Proteins

Cytoskeleton proteins make up the internal structure of a cell. These internal proteins include talin, paxillin, vinculin and tensin. Internal proteins are the connecting link between the cellular cytoskeleton, known as actin filaments, and the membrane receptor proteins or integrins. The connection points between the substrate and the cells are known as focal adhesions. Focal adhesions vary in size and structure, and are closed junctions that are composed of the various cytoskeleton proteins.[11] Specific molecules are involved in focal adhesions.[105] These molecules include the Src kinase family, focal adhesion kinase, paxillin, and tensin.[105] Integrins and cadherins have a direct link into the actin of the cell via the cytoskeleton proteins.[11] As integrins cluster together forming focal adhesions, they signal the tensin protein and focal adhesion kinase (FAK). Upon being signaled, tensin and FAK phosphorylate recruit other cytoskeleton proteins such as talin, vinculin and α-actinin.[11] Proteins like vinculin and talin act as linking proteins to other cytoskeletal proteins, integrins, signaling molecules and protein kinases.[11] These proteins participate in the signaling transduction pathways that relay messages through the cytoplasm. The talin, vinculin and α-actinin then link to the actin filament responsible for cell shape and cell adhesion maintenance.[11]

Src kinases are molecules activated by growth factors during the formation of focal adhesions while other molecules like kinase paxillin and tensin are turned on by integrins. Src kinases start a signal cascading down to the ECM proteins and other growth factors to relay messages from the integrins. These pathways, both intersecting and convergent, evoke cellular responses such as gene expression, cell division, maturation and self–destruction.[37, 67] Thus, it is through intricate detail that molecules send

communicating signals from cell-to-cell and cell-to-substrate, all to promote cellular adhesion, attachment, proliferation, differentiation, new bone formation and eventually apoptosis (programmed cellular death).[37, 66-68, 70, 105, 106]

1.2.4 Vascularization

Vascularization is achieved within a tissue-engineered scaffold upon the formation of new blood vessels. The degree of porosity and interconnections of an engineered scaffold, as previously discussed, have an important role in the development of a vascularized network, capable of providing nutrients, growth factors and hormones to the maturing cells, as well as removing cellular wastes and byproducts. However, it is the angiogenic factors such as fibroblast growth factors (FGF), transforming growth factor β (TGF-β) and vascularized endothelial growth factor (VEGF) that promote the formation of a vascularized network *in vivo*.[37, 107] VEGF is believed to play an important role in bone metabolism as well as in the formation of new bone tissue. Harada *et al.* demonstrated that prostaglandins E1 and E2, osteogenic stimulators commonly expressed during osteoblast maturation, directly affect the up-regulation of VEGF expression.[37, 107] Prostaglandin E2 was also found to increase the mRNA and protein levels of VEGF, thereby increasing the expression of VEGF. However, the effects of prostaglandin E2 can be reversed by the addition of dexamethasome, a common supplement for primary cell cultures.[107]

Although a complete functional role of VEGF is not well understood, it is known to induce and control angiogenesis. The presence of a vascularized network contributes to cellular differentiation, matrix mineralization and new bone remodeling. It is believed

that the addition of angiogenic growth factors to tissue-engineered scaffolds would not only aid in the growth and remodeling of new bone tissue, but also provide an important framework for the development of a blood network.[37]

1.3 Study Objective

The physiological system of bone and the functions of bone regeneration are an extremely complicated process, yet one of the simpler systems of the body. Although it is important to understand the comprehensive workings of the system, it is also important to narrow the investigation in an attempt to solve one small piece of the overall puzzle. The ensuing chapters focus on the development and characterization of dense and porous bone scaffolds, the *in vitro* methods for measuring osteoblast proliferation and the effect of sieved HA powder on cell proliferation and differentiation. The objective is to gain an understanding of how cells interact with scaffolds in a controlled, simplified, *in vitro* model. This preliminary work with dense scaffolds, foamed based porous scaffolds and MC3T3-El osteoblasts provides insight for future *in vivo* studies investigating CaP-based tissue-engineered implants. The fabrication of CaP-based scaffolds is a key component for the development of a suitable engineered implant as discussed in Chapter 2. Chapter 3 will review *in vitro* methods for studying osteoblast proliferation on dense and porous scaffolds. To conclude, Chapter 4 investigates the cellular differentiation and proliferation of MC3T3-E1 osteoblasts on hydroxyapatite scaffolds of different lots varying slightly in the surface and powder properties.

CHAPTER 2

PROCESSING OF HYDROXYAPATITE-BASED ENGINEERING BONE SCAFFOLDS

2.1 Introduction

Calcium phosphate (CaP) based scaffolds are a favorable material for bone applications. Two of many different ceramic scaffold types are dense and porous. Dense ceramic scaffolds are commonly processed by cold uniaxial pressing. Porous ceramic scaffolds may be processed via different fabrication methods, including the polymeric sponge method, the lost wax method, tape casting, slip casting with binders, and foaming, to name a few.[108-112] Dense scaffolds are often preferred for studying cell behavior, and protein and growth factor adhesion because of the simplified, one-dimensional surface. However, dense scaffolds do not approximate accurate structural representation of bone which is naturally porous. Recent research has shown scaffold properties, such as degree of porosity, surface roughness and surface chemistry greatly affect cellular behavior.[1, 13, 17] Furthermore, studying cell interactions on three-dimensional porous scaffolds provides a more realistic model of natural bone.

There are three types of pressing which use pressure to compact ceramic powders; uniaxial, isostatic and hot pressing. Uniaxial pressing compresses powder in a single direction within a metal die.[113] Ceramic scaffolds processed by this method are simple in shape, easily produced, less time consuming, and more cost efficient. Isostatic pressing compresses the ceramic powder in all directions. The ceramic powder is bagged in a waterproof encasing, submerged in a pressurized fluid medium. Ceramic scaffolds processed isostatically can have more complex shapes, but require longer fabrication

times and therefore are less cost efficient.[113] Unlike uniaxial or isostatic pressing, hot pressing combines ceramic powder pressing with ceramic sintering to potentially yield a dense strong compact. Hot pressed scaffolds must be processed one at a time, making fabrication time consuming and costly.[113]

The ceramic powder used for pressing can be either manually prepared with a polymeric binder coating, or processed as-manufactured. Binders enable the ceramic powder particles to adhere to each other by imparting additional strength to the green compact, the unsintered form of the pressed powder. However, binders can leave residues toxic to the *in vitro* or *in vivo* cellular environment. *In vivo*, binder residuals have been shown to elicit localized tissue reactions such as inflammation that increases the potential risk of infection and eventual rejection of the implant by the body. Fabricating dense pressed scaffolds with as-manufactured ceramic powders eliminates the use of a binder, and hence potential toxic residues resulting from insufficient burn-off of the binder during sintering.

Porous ceramic scaffolds are often designed to model the porosities of cortical and cancellous bone by incorporating a vascular network consisting of interconnected macro- and micropores.[37] This vascular network supplies proteins and growth factors to the cellular components, which are necessary for the deposition and mineralization of new bone.[37] Macropores ranging in size from 100 to 400 μm are believed to be optimal for cellular ingrowth.[21, 41, 43, 44] Macropores filter the cellular and vascular components of bone and blood vessels.[1, 21] Micropores typically less than 100 μm, are present within the structure of the macropore wall, and greatly increase the total surface area for protein adsorption and ion exchange.[21] These pores provide a favorable surface for cellular

adhesion and differentiation.[21] Micropores form interconnecting channels between the macropores, which allow for the transport of nutritional fluids to the cells, and the transport of cellular waste away from the cells, promoting bone growth.[114]

There are many different processes by which porous ceramics are fabricated. Some of these methods include polymeric sponge method, the lost wax method, tape casting, slip casting with binders, and foaming.[108-112] Arita *et al.* developed the polymeric sponge method to fabricate porous hydroxyapatite (HA) sheets by tape casting with a $CaCO_3$ gas-forming agent.[109] Using this method, porous HA sheets were produced with a porosity of 62%, however their limited pore diameter (<10 μm) restricted bone ingrowth.[109] The lost wax method yields porous ceramics from a negative replica of a porous skeletal microstructure filled with ceramic slurry.[108] During high-temperature sintering, the wax burns off leaving an interconnected porous scaffold.[108] Once again, these fabricating techniques require the use of binders, which as was previously discussed, leaves residues that are potentially toxic to the *in vitro* and *in vivo* cellular environment.

Foaming was a technique originally developed by Ryshkewitch, where a viscous Al_2O_3 slip, produced from oxide powder and 0.2% polyvinyl alcohol solution, was mixed with 4% hydrogen peroxide (H_2O_2).[111] This slip was poured into an open aluminum frame, placed into a drier and slowly heated to activate the H_2O_2 gas, producing the porous green bodies.[111] Foaming uses H_2O_2 to produce gas bubbles that become trapped within the drying ceramic. The original foaming process also used a polymer binder incorporated into the viscous slip.[111] An alternative to this method is to use a binderless process that involves foaming a ceramic slurry, colloidally stabilized in a suspension of

ceramic powder and a indifferent electrolyte.[115] Hignite *et al.* concluded that eliminating the use of binders from porous processing of CaP ceramics, improved the control of pore development and resulted in pure CaP scaffolds, free from toxic chemical residue.[115] Yang *et al.* also utilized H_2O_2 to foam porous biphasic calcium phosphate (BCP, 65% HA and 35% βTCP) scaffolds, having a porosity of 61% and an average a pore size of 402 μm.[114] This chapter will focus on detailed processing of uniaxial pressed dense scaffolds and binderless foamed porous scaffolds, as well as useful methods for characterizing scaffold properties.

2.2 Materials and Methods

2.2.1 Hydroxyapatite

Hydroxyapatite (HA, Hitemco Medical Applications, Old Bethpage, NY), one of the more researched CaP bioceramics for bone applications HA powder, was used in this study to fabricate both dense and porous scaffolds. This HA powder was fabricated by the precipitation method, then sintered and sieved to obtain a fine range of particle sizes.[116] The HA powders under investigation were processed by the conventional gravity sieving method (G) or by a combination of conventional gravity sieving and airjet sieving (GJ). The average particle size was 34.5 μm ± 19.7 μm and 11.0 μm ± 8.1 μm for the HA-G and HA-GJ powders, respectively.[116]

2.2.2 Fabricating Dense Scaffolds

Dense scaffolds were processed by uniaxial pressing as-manufactured (AR) G and GJ HA at 13.8 MPa (2000 psi) for 1 minute using a Carver press (Carver Inc., Wabash, IN). The powder was pressed into green compacts, 13 mm or 32 mm in diameter. The green compacts were carefully removed from the die, placed on an alumina dish and sintered at 1360°C for 4 hours in a 1612FL CM Box Furnace (CM Furnaces, Bloomfield, NJ), with molydisilicide heating elements. The sintering furnace was programmed to reach 1360°C in 2 hours with a controlled ramp up and ramp down rate of 11.3°C per minute.

2.2.3 Fabricating Porous Scaffolds

Porous HA scaffolds were prepared by foaming a slurry consisting of HA powder suspended in an indifferent (pH 7.4) potassium nitrite (10^{-3}M KNO_3) electrolyte. H_2O_2 was then added as the binderless foaming agent. G and GJ powders were foamed into both approximately 30% and 50% porous scaffolds. The approximately 30% porous scaffolds were foamed according to an HA: KNO_3: H_2O_2 ratio of 43: 55: 2 (by volume), with an H_2O_2 concentration of 5%. The approximately 50% porous scaffolds were foamed according to an HA: KNO_3: H_2O_2 ratio of 36: 58: 6 (by volume), with an H_2O_2 concentration of 30%.

Using the appropriate foaming ratio, suspensions were prepared by uniformly suspending HA powder in indifferent KNO_3 electrolyte. After thorough mixing, the H_2O_2 foaming agent was added to create a slurry. This slurry was then mixed vigorously by hand until homogeneous, injected into cylindrical molds (Sil-mold-25, Synair,

Chattanooga, TN) and was dried for 1 hour at 125°C in a gravity convection oven (Lindberg Blue, Asheville, NC) to evaporate the physisorbed water. These fragile green compacts were gently removed from the mold, placed on an alumina sintering dish and sintered at 1360°C for 4 hours in the 1612FL CM Box Furnace programmed to reach 1360°C in 2 hours.

2.2.4 Powder X-Ray Diffraction (XRD)

The bulk chemistry of the AR HA powders and the processed HA scaffolds was determined using powder XRD (Rotaflex, Rigaku, Japan). XRD was also used to confirm the phase purity throughout the processing steps of the dense and porous scaffolds. The resulting scans of the processed scaffolds were referenced to standard patterns from the Joint Committee on Powder Diffraction Standards (JCPDS) database and to the resulting control scans of the AR powders. The specimens under investigation were ground by mortar and pestle into a fine powder visually comparable in consistency to the AR powders in preparation for analysis. The ground powders were then placed on a low background holder and scanned between 2θ values of 20° and 60° with a step size of 0.05 at 2° per second, using monochromatic Cu Kα x-rays. The sizes used for the DS, RS, RS_m and SS slit filters were $^1/_6$°, 0.3, 0.45 and $^1/_6$°, respectively.

2.2.5 Fourier Transform Infrared Spectroscopy (FTIR)

FTIR (Spectrum BX, Perkin Elmer, Wellesley, MA) was used to analyze the chemistry of the dense and porous scaffolds processed from both G and GJ powders.

These scaffolds were prepared for FTIR in a manner similar to XRD; ground by mortar and pestle into a fine powder comparable in consistency to the AR powders. The powder was carefully spooned into the detector, and scanned by a KBr beam splitter. Eight single-beam scans were collected over the range of 650 to 4000 cm^{-1}, in 1.0 cm^{-1} intervals with a resolution of 2.0 cm^{-1}, and averaged to yield the resulting IR scans. An ATR-cell was in collecting a single-beam background spectrum that was subtracted from the test scans to obtain a spectrum for the HA powders.

2.2.6 Scaffold Imaging

The scaffolds were imaged by scanning electron microscopy (SEM) using a JEOL 6300F (Japan Electron Optics Laboratories) microscope, with a field emission gun. Each specimen was coated with a thin layer of gold to aid in conducting the electrons over the ceramic surface. SEM imaging was performed at an accelerating voltage of 15 keV, with a working distance of 15mm. The SEM images were used to determine the grain size of the dense scaffolds, by the line intercept method.[113] Macro- and micropore sizes of the porous scaffolds were measured using SPOT Imaging software.

2.2.5 Porosity Determination

Two methods were used to determine the porosity of the porous scaffolds, Archimedes volume displacement and mercury porosimetry. The Archimedes method followed the ASTM standard (C20-97) with slight modifications to accommodate smaller scaffolds sizes. Using Archimedes method, the porosity was calculated from the sample

dry mass, suspended mass and the saturated mass. All specimens were dried at 125 °C for 1 hour in a gravity convection oven to evaporate any excess moisture, and then weighed to obtain the dry mass. Subsequently, the scaffolds were placed in clean, individually labeled beakers filled with distilled H_2O and placed under vacuum conditions to force trapped air within the inner pores out of the scaffold. A vacuum was drawn to 0.84 atm (25 inHg) for 10 minutes, then released and drawn again to 0.87 atm (26 inHg). After 30 minutes, the pressure was released. A vacuum was then drawn to 0.90 atm (27 inHg) for another 30 minutes. This process was repeated until no more air was extracted from the scaffold in the form of bubbles. Using a special apparatus for density determination, the suspended mass was collected. The scaffolds were lightly rolled on a clean, dry cloth and weighed to obtain the saturated value. From the dry mass, suspended mass and saturated mass, the porosity was calculated (Appendix A).

Mercury (Hg) porosimetry was used to verify the scaffold porosity. Hg-porosimetry results were collected using an AutoPore IV porosimeter and AutoPore software (Micromeritics, Norcross, GA). The porous scaffolds were assembled in a 0.387 cm^3 solid sample penetrometer and run under both low and high pressure analyses conditions. Low pressure analysis filled the penetrometer chamber with Hg and pressurized the chamber up to 3.5 atm (50 psig). Upon completion of the low pressure analysis, the penetrometer assembly was weighed. The mass of the assembly was input into the AutoPore software for the final porosity determination post the high pressure analysis. The high pressure analysis pressurized the Hg in the chamber to 204.1 atm (3000 psig) forcing the Hg to infiltrate the open pores and calculate an intrusion volume which was used in the calculating the porosity.

2.2.8 Surface Profilometry

The arithmetic mean surface roughness (R_a) of the dense scaffolds, measured using a Hommel RC4000 profilometer (Hommelwerke), was calculated over a measurement length of 10 mm at a velocity of 0.5 mm per second. Six, randomly selected dense scaffolds (n=6) were used in the determination of the R_a value. Three measurements from each HA scaffold, were collected, averaged, and used for the statistical analysis. Statistical significance for the R_a values was determined using one-way ANOVA analysis, with a Tukey post-hoc test. Statistical significance was considered if $\rho < 0.05$.

2.3 Results and Discussion

2.3.1 Dense Scaffolds

During this study, observations were made regarding dense pressing that greatly impacted the quality and uniformity of the HA scaffolds. The first observation involves evenly distributing the HA powder within the die chamber. Evenly distributed powder minimizes density gradients, thereby reducing the number of internal cracks and defects, yielding a more uniform dense scaffold. Uniformly and non-uniformly dense scaffolds also have distinct color differences. Uniform scaffolds appear to have a consistent pale blue-green color post sintering, whereas non-uniform scaffolds have distinct light and dark blue-green shaded regions, post sintering (Figure 4). Uniform discs were also found to be easier to remove from the die without breakage, leading to the next observation.

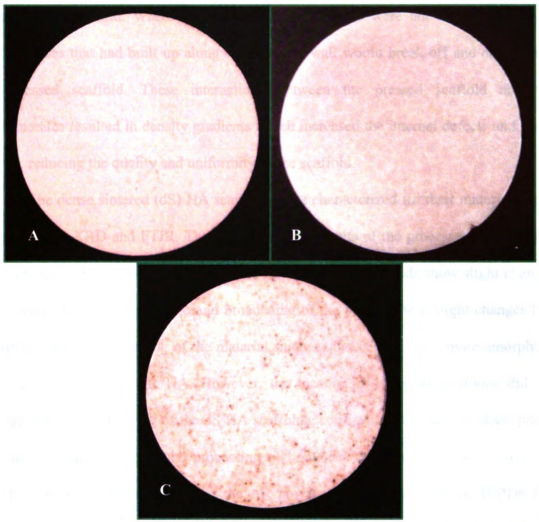

Figure 4: These digital images of sintered dense pressed HA scaffolds depict a uniformly dense scaffold (A), a non-uniformly dense scaffold (B), and a contaminated dense HA scaffold (C). The uniformly dense scaffold is uniform in color where the non-uniformly dense scaffold have has distinct light and dark shaded regions. The contaminated scaffold has a speckled appearance as compared to the non-uniform scaffold.

The manner in which scaffolds were removed from the die chamber also impacted the disc quality and uniformity. Although evenly distributed powder within the die chamber minimizes internal defects and small cracks, it was important that extreme care be used when removing the discs to prevent breakage or chipping of the scaffold.

Lastly, cleanliness of the die and the die components was essential in the prevention of agglomeration buildup along the chamber walls which impacts the quality

of the dense scaffold. When the die and die components were not cleaned regularly, agglomerates that had built up along the chamber wall would break off and embed into the pressed scaffold. These interactions between the pressed scaffold and the agglomerates resulted in density gradients which increased the internal defects and small cracks, reducing the quality and uniformity of the scaffold.

The dense sintered (dS) HA scaffolds were characterized for their material purity using powder XRD and FTIR. The bulk chemistry results of the processed dS scaffolds were obtained from XRD. The XRD scans for the dS HA scaffolds show slight changes in the peak–to–peak height ratio and broadening of the peaks. These slight changes that occurred during the sintering of the material suggests the dS HA has a more amorphous HA structure than the AR HA. However, the location of the peak positions did not change during the sintering of the dS HA scaffolds, confirming that the HA phase purity was maintained throughout the processing of both the dS HA-G and dS HA-GJ. The XRD scans were referenced against the AR powder control scans and the JCPDS HA PDF # 09-0432. (Figure 5)

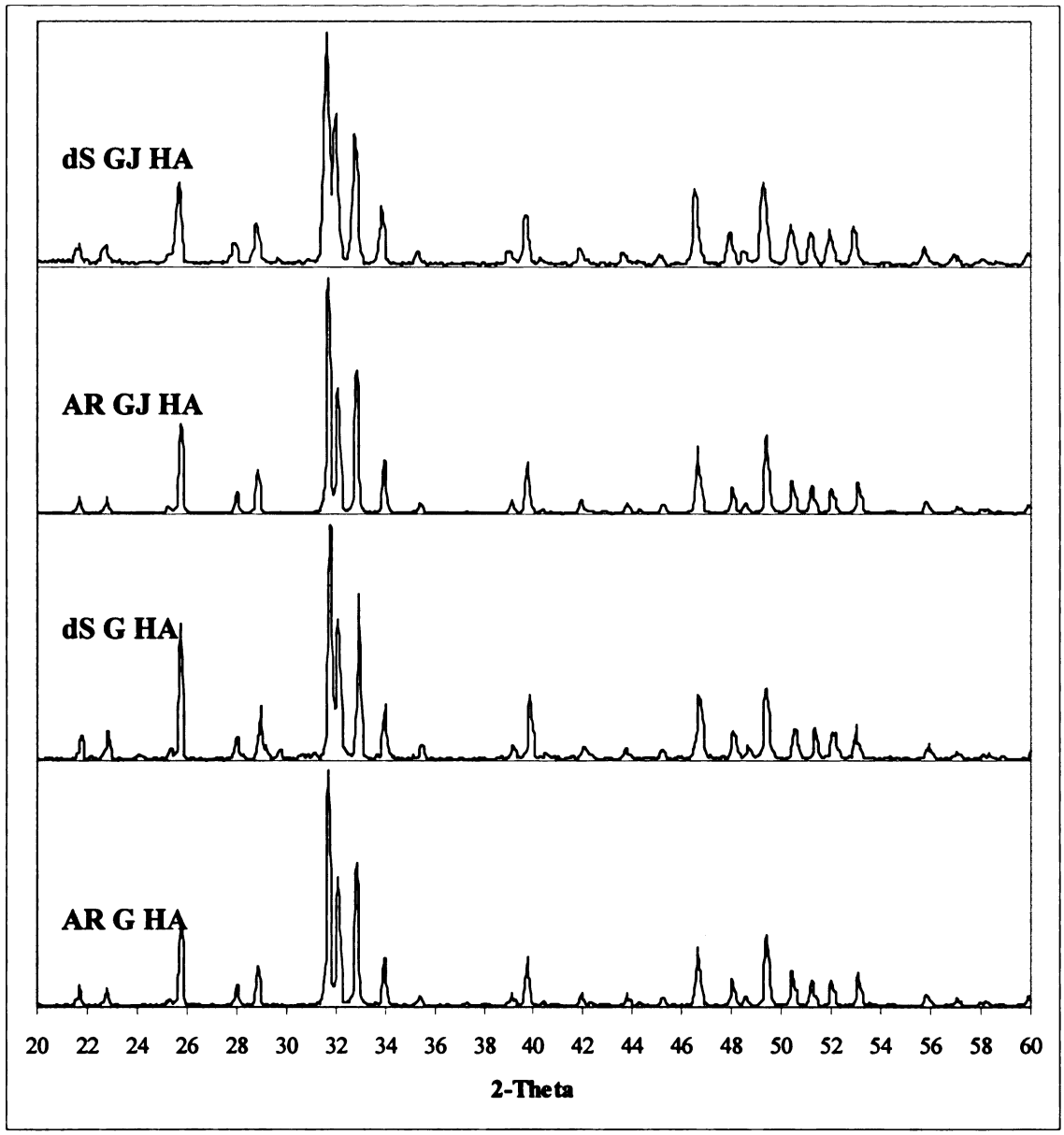

Figure 5: This figure shows the XRD scans that compare AR G and GJ HA and dS G and the GJ HA. All scans demonstrate the characteristic HA peaks as referenced to JCPDS PDF# 09-0432. The G and GJ AR scans are comparable in that they have similar peak-to-peak height ratios, peak positions and peak width. This indicates the bulk chemistry of the G and GJ AR HA powders are analogous. When comparing the AR powders to the G and GJ dS HA, the peak positions are also comparable, demonstrating the HA phase purity was maintained during processing of the dS HA scaffolds. The peak-to-peak height ratios changed for dS HA, as was slight peak broadening observed. These slight changes in the dS HA, which occurred as a result of sintering, suggest a decrease in the crystallinity. No significant chemistry differences were observed between the G and GJ dS HA scans. Each scan represents one scan from three independent samples scanned for each scaffold type.

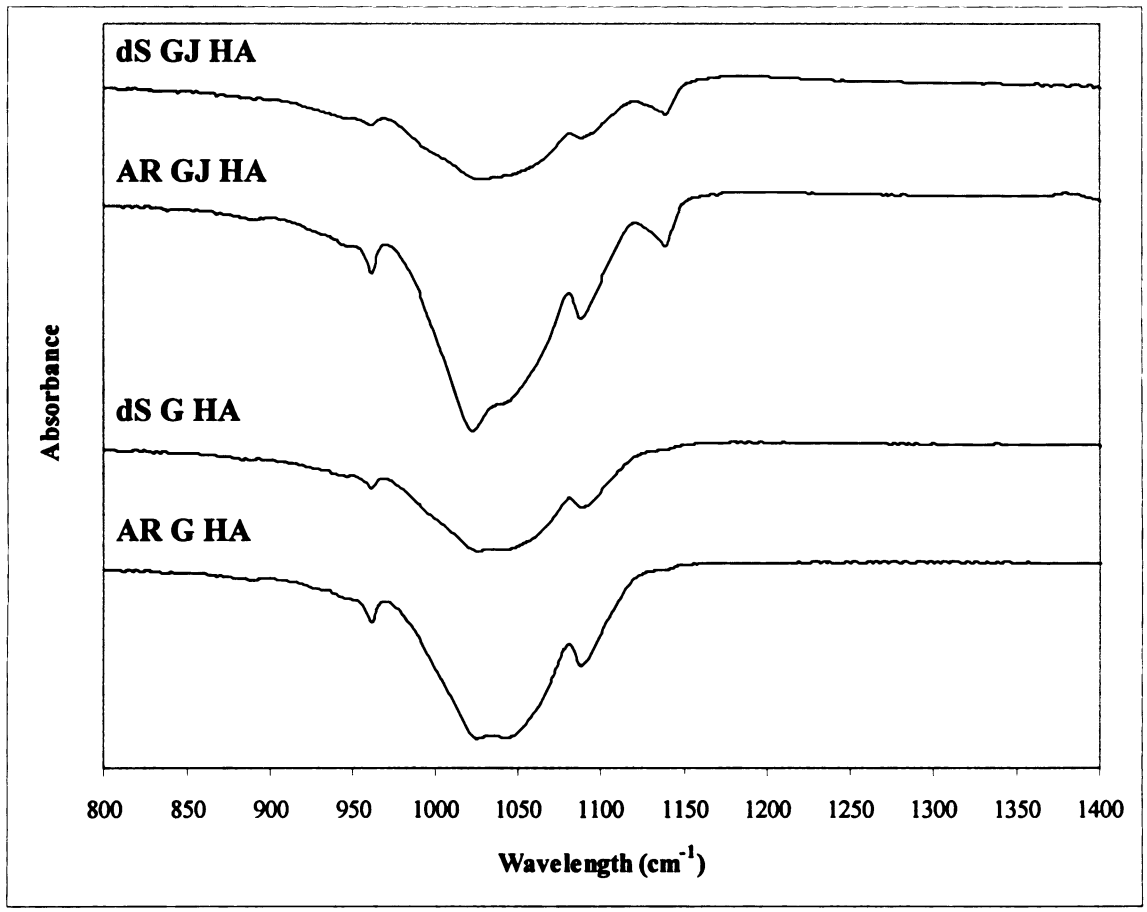

Figure 6: This figure shows the FTIR results, comparing the AR G and GJ HA to dS G and the GJ HA. All scans demonstrate characteristic triply asymmetric stretching modes of ν_3 P-O bonds of the HA phosphate group at 1022, 1044 and 1087 cm^{-1}.[55, 117-119] The FTIR results for the G and GJ AR scans indicate slight differences in the relative absorbance and the peak-to-peak height ratio, demonstrating slight chemistry variations between the AR G and GJ HA powder. These variations are indicative of the manufacturing process, since are observed in the AR powders. When comparing the AR powders to the G and GJ dS HA, peak positions are comparable, but the relative absorbance of the dS HA decreases and the peak-to-peak height ratios also change. These changes in the dS HA, occur as a result of sintering and verify a decrease in the crystallinity. When comparing the FTIR scans for G and GJ, the GJ scans (both AR and dS) indicate an additional peak present at 1137 cm^{-1}, believed to be trace amounts of HPO_4^{2-} ions. An excess amount of HPO_4^{2-} ions is characteristic of non-stoichiometric, calcium-deficient HA.[118-121] Each scan represents one scan from three independent samples scanned for each scaffold type.

The FTIR scans of the AR, dS HA-G, and dS HA-GJ demonstrated little difference in the peak positioning between the G and GJ powders. The peaks observed at 1022, 1044 and 1087 cm^{-1} are identified as the characteristic triply asymmetric stretching modes of ν_3 P-O bonds of the HA phosphate group.[55, 117-119] (Figure 6) The peak–to–peak height ratios varied slightly between the G and GJ, of the AR and dS scans. However, the absorbance strength of the AR HA is much greater than the absorbance strength for dS HA. These results are in agreement with the XRD results, suggesting the sintered scaffolds have a decreased crystallinity as compared to the AR HA powder.[55] Although the characteristic HA peaks are identified for the G and GJ HA powders, an additional peak was observed on both the AR and dS GJ scans at 1137 cm^{-1}. One explanation for the additional peak could be due to nucleation of a second CaP phase, such as tricalcium phosphate (TCP), octacalcium phosphate (OCP), or dicalcium phosphate dihydrate (DCPD); all of which have characteristic peaks present at 1137 cm^{-1}.[33] Since this peak was present in both the AR and the dS scans, the formation of a second CaP phase due to grain boundary precipitation as a result of sintering can be ruled out. Also, the XRD scans confirm there were no additional phases present prior to and post sintering of the dense scaffolds, which would suggest that the additional peak present was not caused by the formation of a second CaP phase.

Another possibility for the additional peak could be related to the presence of excess HPO_4^{2-} groups from nonstoichiometric HA.[33] Trace amounts of HPO_4^{-2} were found in the HA crystals formed by various HA precipitation method that used $CaCl_2$, KOH and KH_2PO_4 as the reactants.[33, 117-119, 121] Ishikawa *et al.* also saw the incorporation of HPO_4^{2-} into the IR scans of calcium-deficient HA.[120] These deficiencies were not

detected in the XRD scans resulting in substantially equivalent scans for the calcium-deficient and stoichiometric HA.[120] And, since this peak was present in both the AR and dS scans for the GJ powder it is highly probable it resulted during manufacturing. Although the process by which Hitemco Medical Applications precipitates HA is proprietary information, it is possible that calcium-deficient HA was formed during the precipitation phase of manufacturing.

Surface roughness and grain size are both dependent properties of the particle size, and have been shown to affect cellular attachment and growth.[62] The HA manufacturer reported the G and GJ HA particle size to be 34.5 ± 19.7 μm and 11.0 ± 8.1 μm, respectively, as measured by a Microtrac S3000 pore size analyzer.[116] The surface roughness and grain size were determined for dS G and GJ HA scaffolds. The surface roughness was greater on the G HA scaffolds than the GJ HA scaffolds. The difference in surface roughness was determined to be statistically significant with an average R_a value of 0.336 ± 0.027 μm for the G HA scaffolds and 0.265 ± 0.0163 μm for the GJ HA scaffolds. The R_a value is calculated based on the differential change in wand height over a specified length. The wand is initially calibrated at zero, and contours the surface as it moves over the specified length. One would expect to find a larger height differential on the scaffold fabricated with a greater average particle size, as was seen in this study. The effect of surface roughness on osteoblast cells is investigated and discussed in Chapter 4.

The results from the grain size determinations were different than expected. One would expect a smaller average particle size to have a smaller grain size. In this case, there was no significant difference in the grain size measurements between the dS G and GJ HA scaffolds. The grain size for the dS GJ HA was determined to be 4.1 ± 0.7 μm,

while the grain size for the dS G HA was determined to be 4.4 ± 0.5 μm. The micrographs (Figure 7 and Figure 8) show a visual depiction of the grains of the dS G and GJ scaffolds, confirming comparable grain sizes between the two different HA lots. The resulting grain sizes contradict the average particle sizes reported by the manufacture. One explanation to this discrepancy is the particle sizes reported by the manufacturer are in fact not individual particles but agglomerates of many smaller particles. The AR HA powder was imaged at low and high magnifications under SEM and the results confirm the AR HA powder agglomerates (Figure 9), which explains the discrepancy between the average grain size and reported particle size. In actuality, the manufacturer reported the agglomerate size.

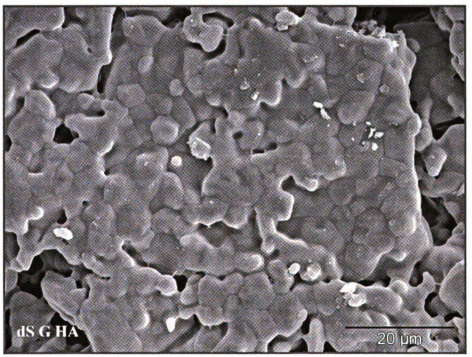

Figure 7: This SEM image depicts the grain boundaries of dS G HA under 1500X magnification. The grain size for the dS G HA was calculated, by the line intercept method, to be 4.4 ± 0.5 μm.

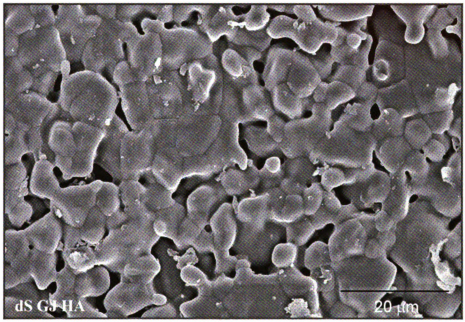

Figure 8: This SEM image depicts the grain boundaries of dS GJ HA under 1500X magnification. The grain size for the dS GJ HA was calculated, by the line intercept method, to be 4.1 ± 0.5 µm.

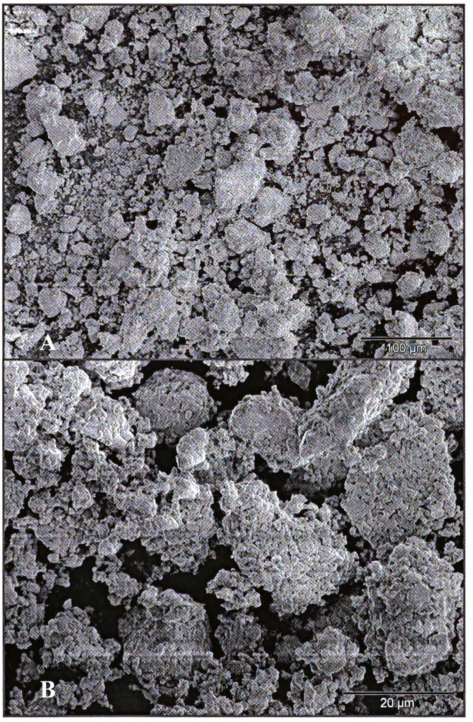

Figure 9: These SEM micrographs depict agglomerate formation of AR HA powder. Under low magnification (250X), the agglomerates appear to be individual particles that would approximate the particle size reported from the manufacturer. When this region is magnified to 1500X magnification, the agglomerates consist of clumps of smaller particles.

2.3.2 Porous Scaffolds

Observations gathered during foam processing of porous scaffolds have found the HA: KNO_3: H_2O_2 ratio (by volume) to be an important design criterion. As was observed during processing, a more viscous slurry traps smaller bubbles, formed from the reaction of the H_2O_2 foaming agent, and produces a less porous scaffold with a smaller average pore size. In a less viscous slurry, the trapped gas bubbles move throughout the slurry with greater ease. As these bubbles rise, they combine together to form a more porous scaffold with a larger average pore size.

The concentration of the H_2O_2 foaming agent was another critical factor when foaming porous scaffolds. Foaming with 30% H_2O_2 produced a more highly porous scaffold, while foaming with a 5% H_2O_2 concentration was ideal when processing less porous scaffolds. The two HA: KNO_3: H_2O_2 ratios, 43: 55: 2 (by volume, with 5% H_2O_2) and 36: 58: 6 (by volume, with 30% H_2O_2) were developed to foam scaffolds with an estimated porosity of 30% and 50%, respectively. The actual porosity of the scaffolds was determined to be 27 ± 2.3% and 57 ± 4.5% porous for the 43: 55: 2 and 36: 58: 6 ratios, respectively, using a modified version of the Archimedes volume displacement method. The porosity results obtained from mercury porosimetry verified the Archimedes volume displacement method. The porosity determined by mercury porosimetry was 27 ± 8.0% for the 43: 55: 2 ratio and 55 ± 5.8% for the 36: 58: 6 ratio (Figure 10). For simplicity purposes, the porous foamed (pf) scaffolds processed from the HA: KNO_3: H_2O_2 ratios, 43: 55: 2 and 36: 58: 6 will be referred to as pf27 and pf57, respectively.

SEM imaging was used to show the differences in surface topography of the dS, pf27 and pf57 scaffolds. Figure 11 shows an increase in the number of pores with an

increase in porosity. The average macropore size (pores larger than 100 μm) also increased with porosity. The average macropore size for the pf27 scaffolds was 164 μm, while the pore sizes ranged from 100 to 501 μm, and the average macropore size the pf57 scaffolds was 256 μm while the pore sizes ranged from 103 to 669 μm. This demonstrates scaffolds foamed with a lower H_2O_2 concentration (5%) resulted in smaller macropores, where as the scaffolds foamed with a higher H_2O_2 concentration (30%) resulted in larger macropores. The micropores (pores smaller than 100 μm) were also characterized for both the pf27 and pf57 scaffolds. While the micropores of both pf27 and pf57 scaffolds ranged size from 24 – 99 μm, the average micropores size was 76 μm for the pf27 scaffolds and 57 μm for the pf57 scaffolds.

The porous structure pf57 scaffolds consists of macropores with interconnecting micropores. This interconnecting porosity allows for fluid to flow through the pf57 scaffolds. The interconnectivity was experimentally verified by allowing water to flow through the scaffold which was placed in a silicon mold. The mold sealed the scaffold edges, and only allowed water to flow through the open porosity of the scaffold. Water did not flow through the pf27 scaffolds when tested for interconnecting porosity and thus the pore structure of the pf27 scaffold consists primarily of closed pores.

Another factor found to greatly influence the foaming reaction was the concentration of the H_2O_2. H_2O_2, a weak, colorless acid, was found to be a very effective binderless foaming agent that does not leave behind toxic residue on the scaffold, as confirmed by XRD results (Figure 12). However, H_2O_2 breaks down quickly into water and oxygen gas, if left at room temperature for an extended period of time, and/or exposed to heat, water, oxygen, light, traces of dirt or traces of heavy metal ions.[122]

$$H_2O_2\,(l) \rightarrow H_2O\,(l) + O_2\,(g), \quad (4)$$

Therefore, it was found that the theoretical concentration of the H_2O_2 did not always accurately represent the actual concentration of the H_2O_2, depending on a variety of variables the foaming agent was exposed to. It was found that a more precise scaffold porosity was obtained when the concentration of the H_2O_2 foaming agent was known and verified. The H_2O_2 concentration was verified by the standard reduction titration method.[122] To ensure an accurate concentration of the H_2O_2, fresh stock solutions of the diluted concentrations were made on a regular basis. When making fresh stock solutions, the concentration of the high purity H_2O_2 (30% concentration) was first verified by volumetric titration. If the diluted concentrations were not freshly made, verifying the concentration prior to foaming was critical.

These HA scaffolds were also characterized for their material purity using powder XRD and FTIR. The results from the XRD scans confirm HA purity during the fabrication of the unsintered (U) porous green compacts (Figure 12) The relative peak – to – peak height ratios, and the peak widths remain the same for the AR powders, and the U pf27 and U pf57 scaffolds, for both G and GJ HA lots. The consistency in the scans confirm that there is no chemical interaction between the HA powder, the indifferent KNO_3 electrolyte and the H_2O_2 foaming agent used. Only the characteristic peaks for HA are observed, which verifies that this binderless foaming processing does not induce undesirable chemical residues.

The XRD scans for the sintered (S) pf27 and S pf57 scaffolds confirm the HA phase is maintained during processing as the characteristic HA peaks are identified (Figure 13). Differences in the relative peak – to – peak height ratio were observed on

both the G and GJ HA scans for S pf27 and S pf57, suggesting that sintering decreases the crystallinity of the HA phase. Additional peaks were also observed on both the G and GJ HA scans for S pf27 and S pf57 at 2-θ values of 29.8° and 30.7°. These non-characteristic HA peaks were references against JCPDS PDF #09-0169 and identified as characteristic βTCP peaks.

To better characterize the additional peaks identified in the XRD scans, FTIR was conducted on both the G and GJ HA for the S pf27 and S pf57 scaffolds (Figure 14). The FTIR scans of the G and GJ HA for the S pf27 scaffolds as compared to the AR control scans were substantially equivalent, except for the peak-to-peak height ratios, the peak width and the absolute intensity. The FTIR scans of the G and GJ HA for the S pf57 were substantially different from the AR control scans. On these scans, additional uncharacteristic HA peaks were observed at 1150, 1400 and 3000 cm^{-1}. Since trace amounts of the βTCP were identified in the XRD scans, a control scan of unsintered βTCP was performed. The results of this control clearly identify the peaks in the S pf57 scans to be βTCP. These peaks were not present in the G or GJ HA scans of the AR powder, therefore the formation of βTCP occurred during sintering. As previously discussed (Chapter 1.2.1.1), the stability of the HA phase during sintering is dependent on the sintering temperature and the partial pressure of H_2O.[9, 13, 123] When sintering HA, chemisorbed H_2O evaporates creating an atmosphere suitable for maintaining a stable HA phase at high temperatures as seen by the XRD and FTIR scans for the dS and pf27 scans of both G and GJ HA powders. However, the highly porous HA scaffolds (pf57) have a greater surface area which allows for the evaporating chemisorbed H_2O to dissipate before generating the atmosphere necessary to stabilize the HA phase at high sintering

temperatures. Without a sufficient partial pressure of water present, βTCP is the stable phase and thus grain boundary precipitation of βTCP occurs.[9] The characteristic, feather-like structure of βTCP was observed along the grain boundary when imaged using ESEM, confirming the nucleated second phase is βTCP (Figure 14).

An additional peak 1137 cm^{-1} was identified in the FTIR scans of the AR HA. This peak is associated with the presence of excess HPO_4^{2-} groups from nonstoichiometric HA. Excess amounts of HPO_4^{2-} are commonly identified when HA is manufactured via the precipitation method. The HA used in this experiment was manufactured via the precipitation method using common reactant that are associated with excess HPO_4^{2-}. At temperatures between 650 and 750°C these excess HPO_4^{2-} groups can give rise to a βTCP phase. Equations 5 through 7 depict the chemical breakdown of these excess HPO_4^{2-} groups into nonstoichiometric HA and βTCP phases.[120]

$$2HPO_4^{2-} \rightarrow P_2O_7^{4-} + H_2O \quad \textbf{(5)}$$

$$P_2O_7^{4-} + 2OH^- \rightarrow 2PO_4^{3-} + H_2O \quad \textbf{(6)}$$

$$Ca_{10-x}(HPO_4)_x(PO_4)_{6-x}(OH)_{2-x} \rightarrow (1-x)Ca_{10}(PO_4)_6(OH)_2 + 3xCa_3(PO_4)_2 + xH_2O \quad \textbf{(7)}$$

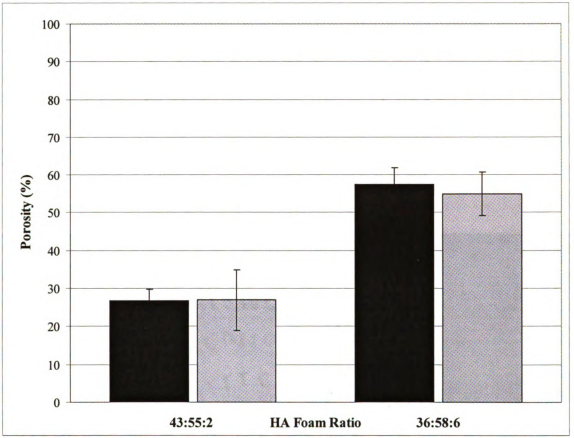

Figure 10: The porosity, determined using a modified Archimedes volume displacement is shown in the figure to be a suitable method for measuring porosity, as verified by mercury porosimetry. Archimedes volume displacement (in black) determined the porosity to be 27 ± 2.3 % for the 43: 55: 2 HA foam ratio and 57 ± 4.5 % for the 36: 58: 6 HA foam ratio. Mercury porosimetry (in gray) verified these results, and determined the porosity to be 27 ± 8.0 % for the 43: 55: 2 HA foam ratio and 55 ± 5.8 % for the 36: 58: 6 HA foam ratio. The Y-error bars represent the standard deviation of n = 12 samples.

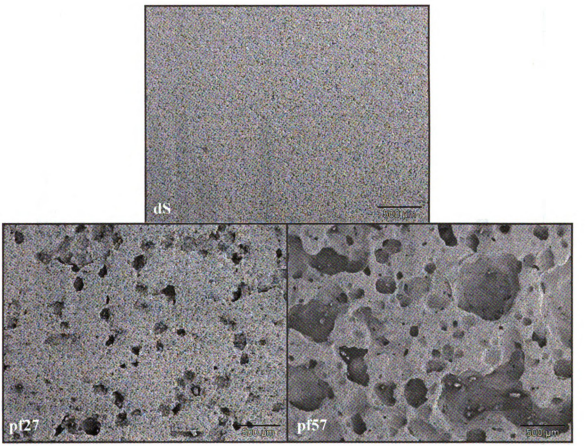

Figure 11: This SEM micrograph depicts the surface topographies of dS, pf27 and pf57 scaffolds at 40X magnification. The dS SEM image, illustrates a near dense surface, and acts as a reference for the foamed scaffolds. As illustrated, the porosity increases from the pf27 scaffolds to the pf57 scaffolds. The pf57 scaffolds have an average macropore size of 256 μm, and an average interconnecting micropore size of 57 μm. The pf27 scaffolds have an average macropore size of 164 μm, and an average interconnecting micropore size of 76 μm. The pore diameters were measured from SEM images of the scaffold surface using SPOT Imaging software. Twelve independent samples were imaged for pore size determination.

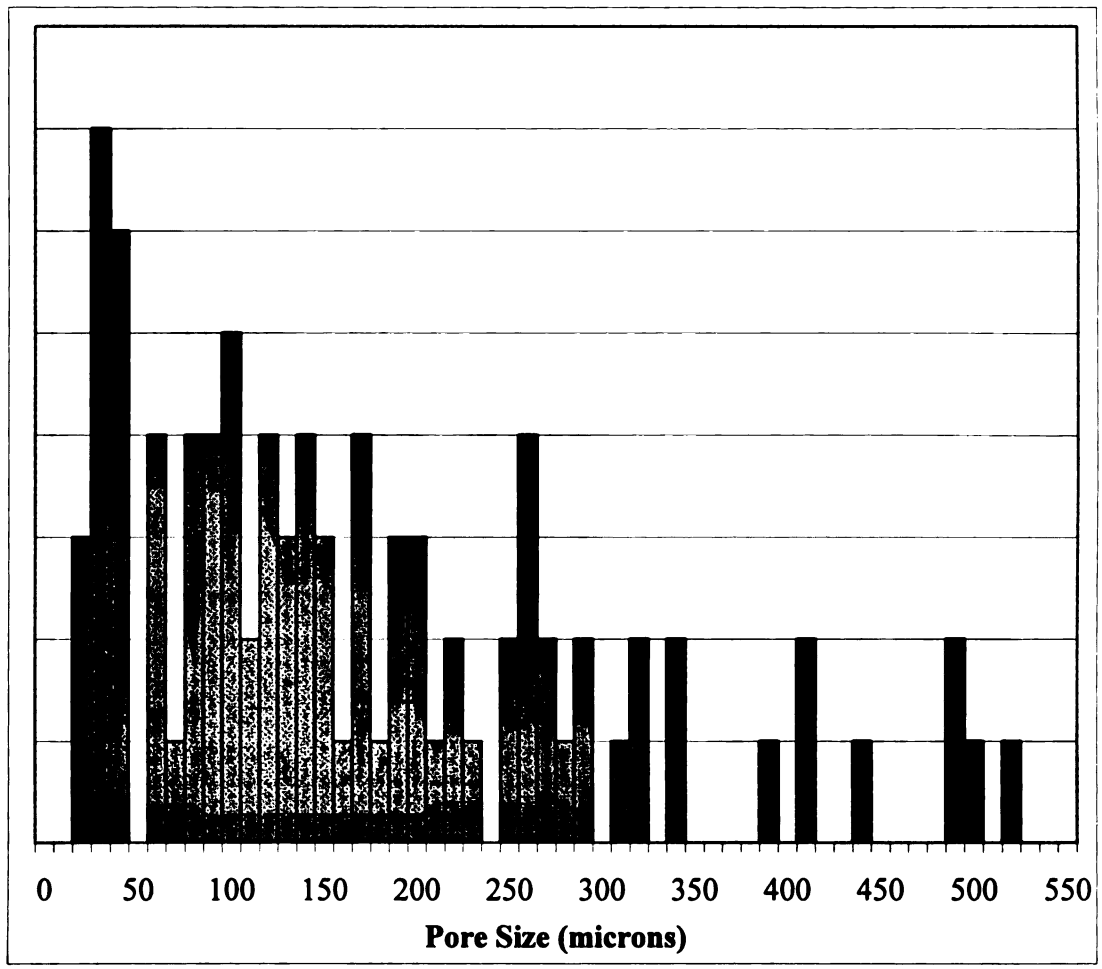

Figure 12: This figure represents the pore size distribution of the pf57HA scaffolds. The macropores are defines as pores greater than 100 μm and the interconnecting micropores are defines as pore less than 100 μm. The average macropore for the pf57 scaffolds was 256 μm. The pore diameters were measured from SEM images of the scaffold surface using SPOT Imaging software. Twelve independent samples were imaged for pore size determination.

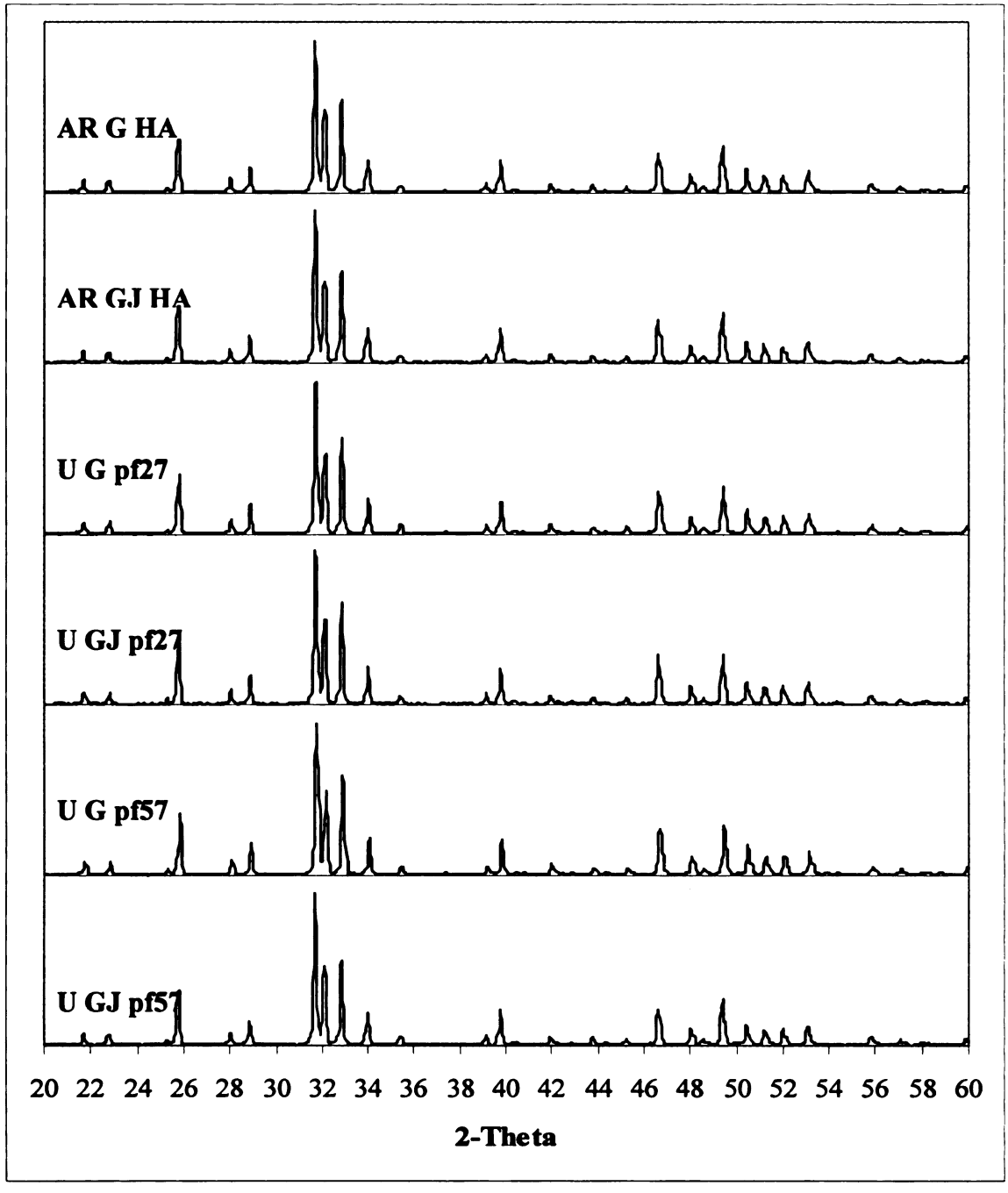

Figure 13: This figure shows XRD scans that compare the G and GJ HA of AR HA, U pf27 and U pf57 scaffolds. The characteristic HA peaks were identified on each of the scans, as referenced to JCPDS PDF# 09-0432, demonstrating the HA phase purity throughout the foaming process. All scans have comparable peak-to-peak height ratios, peak positions and peak width, illustrating the bulk chemistry of the G and GJ AR HA powders are analogous to the G and GJ HA of both pf27 and pf57 scaffolds. This figure confirms that there is no chemical interaction between the HA powders, the neutral KNO_3 electrolyte and the H_2O_2 foaming agent used. It also verifies the foam processing method as a binderless fabrication method that does not yield undesirable chemical residue. Each scan represents one scan from three independent samples scanned for each scaffold type.

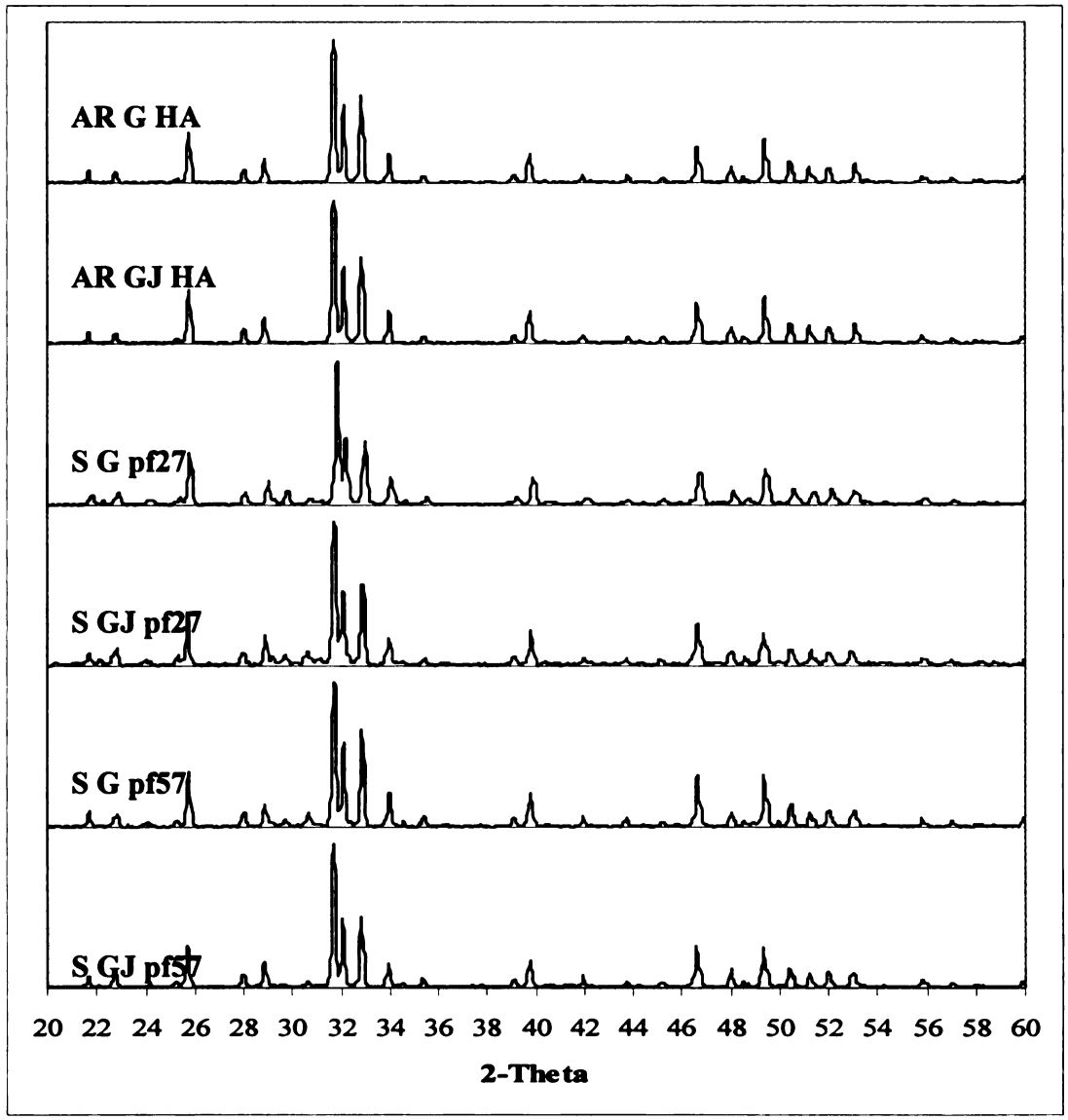

Figure 14: This figure shows XRD scans that compare the G and GJ HA of AR HA, S pf27 and S pf57 scaffolds. All scans demonstrate the characteristic HA peaks as referenced to JCPDS PDF# 09-0432. The peak-to-peak height ratios changed slightly and peak broadening was observed for S foamed HA scaffolds, as a result of sintering, suggesting a decrease in the crystallinity. When compared to the AR powders, the peak positions of the pf27 and pf57 (of both G and GJ HA) are comparable. This suggests the bulk chemistry of the S porous scaffolds is HA. On the S pf27 and S pf57 scaffolds (of both G and GJ HA), additional peaks are note at 2-theta values of 29.8 and 30.7. These peaks indicate nucleation of another CaP phase during the sintering process occurs. The peaks at 2-theta values of 29.8 and 30.7 were referenced against the JCPDS for CaP phases, and were identified as characteristic βTCP peaks according to PDF #09-0169. No significant chemistry differences were observed between the G and GJ dS HA scans. Each scan represents one scan from three independent samples scanned for each scaffold type.

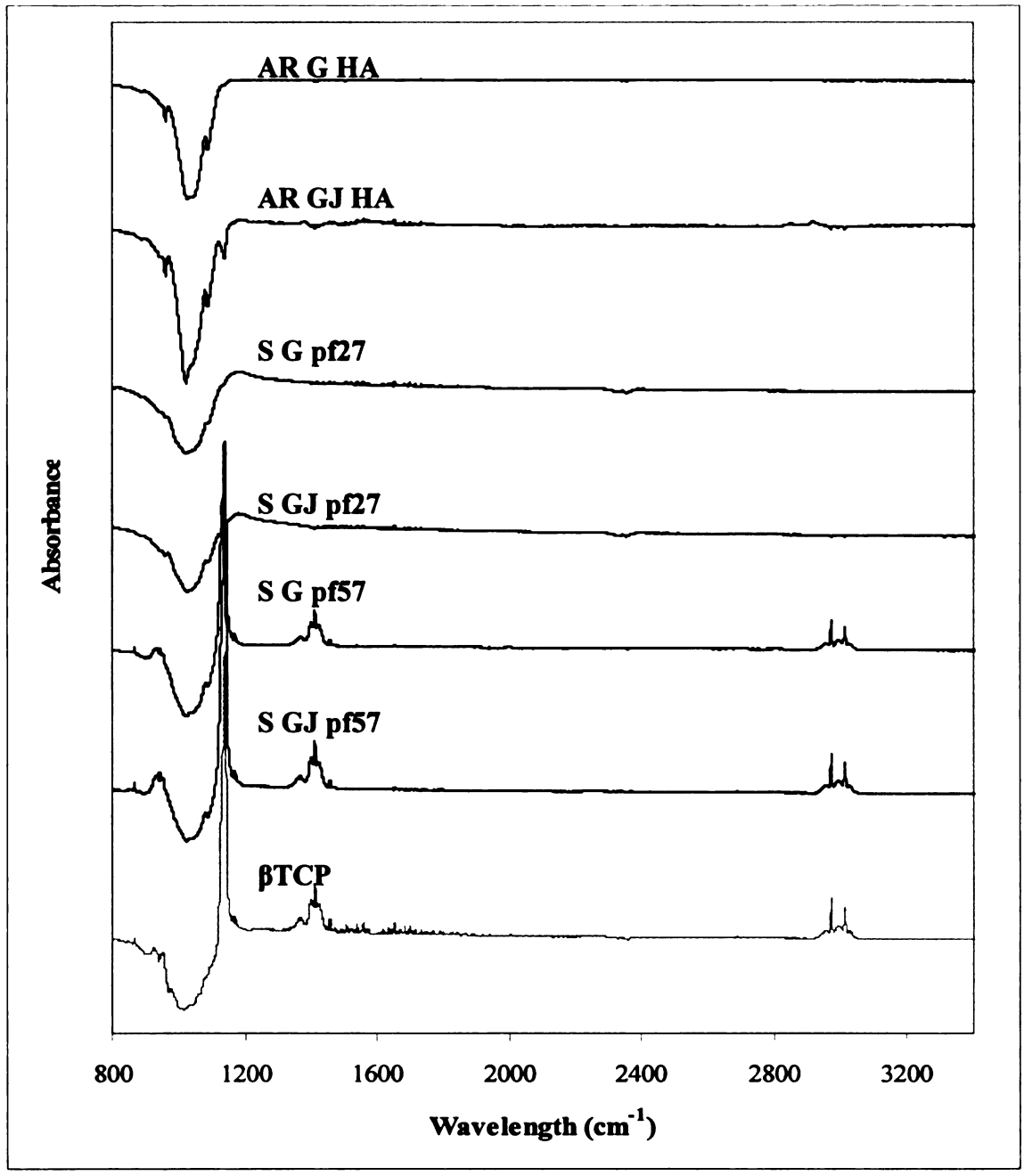

Figure 15: This figure compares the FTIR results of AR G and GJ HA, and S pf27 and pf57 for G and GJ HA scaffolds. The AR and S pf27 scans demonstrate characteristic triply asymmetric stretching modes of ν_3 P-O bonds of the HA phosphate group at 1022, 1044 and 1087 cm^{-1}.[33, 55] Differences are observed in the relative absorbance and the peak-to-peak height ratio suggesting slight chemistry variations. These variations in the S pf27 HA, occur as a result of sintering and verify a decrease in the crystallinity. The resulting FTIR scans for S pf57 HA scaffolds reveal the presence of a distinctly unique phase, as compared to the AR. Based on the XRD results, a control scan of pure, unsintered βTCP (in gray) was performed, and clearly identifies the phase present in the S pf57 HA scaffolds. Each scan represents one scan from three independent samples scanned for each scaffold type.

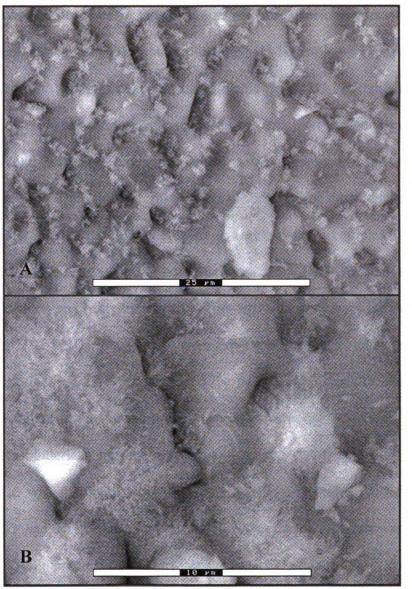

Figure 16: These SEM images of S pf57 HA under high magnifications, 2000X (**A**) and 5000X (**B**), depict βTCP precipitating along the grain boundaries.

2.4 Conclusions

To conclude, this study demonstrated two binderless fabricating methods for processing HA scaffolds; dense pressing and porous foaming. The dense scaffolds, with a flat surface topography, provide a simple and useful model for studying cell interactions on HA; however these scaffolds are not realistic to the structure of bone. There was no

significant difference observed in the grain size of dense scaffolds processed with G or GJ HA powders. However, FTIR results illustrated GJ HA to have excess HPO_4^{2-} ions, often associated with calcium-deficient, non-stoichiometric HA. Although simplistic to fabricate, three recommendations were made during this study to enhance the scaffold quality, yield and integrity; having an even distribution of HA powder, carefully removing the scaffold from the die, and frequent cleaning of the die and its components.

The fabrication of the porous foamed scaffolds is more complex in that varying critical parameters such as the liquid: powder ratio and the H_2O_2 concentration can have significant effects on engineered parameters (porosity and pore size) for the scaffold. In this study, two HA: KNO_3: H_2O_2 ratios were pre-established to engineer scaffolds with two different porosities; 27% porous and 57% porous. The scaffold with the greater porosity also resulted in having the greater average macropore size. XRD demonstrated foaming to be a binderless, non-toxic processing method. XRD also confirmed that the pure HA phase was maintained post-foaming and post-sintering of the 27% porous scaffolds. XRD and FTIR results of the 57% porous scaffolds however, found trace amounts of βTCP precipitating along the grain boundaries; this grain boundary precipitation is a result of the loss in HA phase-stability during sintering.

CHAPTER 3

EVALUATION OF MC3T3-E1 OSTEOBLAST PROLIFERATION ON DENSE AND POROUS HYDROXYAPATITE SCAFFOLDS

3.1 Introduction

Calcium phosphate (CaP) bioceramics have long been used as coatings and filler materials for medical applications. More recently, they have been identified as an osteoconductive matrix onto which osteoblasts (OBs) readily adhere and differentiate.[1] Hydroxyapatite (HA, $Ca_{10}(PO_4)_6(OH)_2$) is one of the most researched CaP bioceramics. The osteoinductive and bioactive properties of HA have been well established.[124] Due to the chemical similarities between the natural inorganic matrix of bone and HA, HA is a favorable material for engineering bone scaffolds. There are two types of scaffolds commonly investigated, dense and porous. There are many factors involved in fabricating these scaffolds. Fabricating binderless scaffolds has been advantageous for cell proliferation and growth; as processing bone scaffolds using binderless methods, do not leave cytotoxic residues within the scaffold. Fabrication methods for processing both dense and porous scaffolds were detailed in Chapter 2.

For many years, research working to understand the proliferation (growth) of bone forming OBs was conducted on simplified, polystyrene substrates. In addition, many assays and procedures used to characterize OB behavior were developed for these polystyrene materials. However, the cell interactions with these plastic substrates differ greatly from the cellular interactions on bioceramics; as was demonstrated by Shu *et al.* in a study where dense HA scaffolds suppressed OB proliferation and enhanced OB differentiation when compared to polystyrene. Therefore, when studying OB

proliferation, it is more clinically relevant to study their behavior on bone or a bone-modeling substrate. Unfortunately the complexities of engineered bone scaffolds, (i.e. surface roughness, surface area, porosity) complicate the interpretation of proliferation assays developed on polystyrene. This chapter provides a comprehensive discussion and review of various methods used to evaluate OB proliferation and the challenges faced when using these methods to characterize OB behavior when cultured on dense and porous engineered scaffolds.

3.2 Preparation of Engineered Scaffolds

Dense and porous HA scaffolds were used as the substrate material for evaluating methods used to determine OB proliferation. Dense scaffolds were fabricated from HA, supplied by Hitemco Medical Applications, as discussed in Chapter 2.2.2. The dense HA scaffolds (dS HA) were pressed into discs 2.30 ± 0.18 mm in thickness and 11.03 ± 0.03 mm in diameter. Porous scaffolds were foamed at an HA: KNO_3: HA ratio of 36: 58: 6 yielding scaffolds 57 ± 4.5% porous, as detailed in Chapter 2.2.3. The porous foamed (pf57) HA scaffolds were cut into discs, using a diamond blade precision bone saw (Isomet 1000, Buehler, Lake Bluff, IL), 3.0 ± 0.18 mm in thickness and 14.0 ± 0.44 mm in diameter. All scaffolds were autoclave sterilized at 121°C at 0.124 MPa (18 psi) for 1 hour in preparation for cell culture. Once sterilized, scaffolds were placed in 24-well polystyrene culture dishes. Agarose gel (1.0%) was used to coat the bottom and sides of the 24-well culture dishes, forming collars around the scaffolds. By coating the wells with agarose, OBs are guided to attach, grow and differentiate on the HA scaffolds. Prior

to OB seeding, scaffolds were rinsed twice with complete media, α-Minimal Essential Medium (α-MEM) supplemented with 10% Fetal Bovine Serum (FBS), for 5 minutes.

3.3 Cell Culture

MC3T3-E1 is a pre-osteoblast cell line developed from newborn mouse calvaria. Research has demonstrated that MC3T3-E1 cells are capable of differentiating into osteoblasts and osteocytes, forming *in vitro* deposition of calcium and phosphate minerals, an initial stage of calcified bone tissue formation.[87] Recent work by Smith *et al.* confirmed MC3T3-E1 OBs behaved in a similar manner as primary OBs harvested from a newborn mouse calvaria, based on ς-potential analysis.[125] Therefore, these cells were used to study the proliferation of OBs on dense and porous scaffolds.

Frozen cells stored at -80°C were promptly thawed and re-suspended in fresh complete media, on polystyrene culture dishes. These cell cultures were incubated at 37°C in a humidified atmosphere of 95% air and 5% CO_2 for 24 hours at which point the cells were enzymatically detached with 1.0% trypsin-EDTA, then divided every 2 – 3 days, further propagating the cell passage.

Upon developing a sufficient cell culture, OBs were seed onto the prepared ceramic scaffolds at a density of 11,320 OBs per cm^2.[26] The surface area for the dense scaffolds was 1.0 cm^2 while the surface area for the porous scaffolds was 10.2 cm^2 (Appendix A). Polystyrene culture wells (PS) were used as the control substrate and had a surface area of 1.8 cm^2. The seeded OBs were fed every 2 days with fresh complete media supplemented with the antibiotics ciprofloxacin (Cipro, 10 μg/mL) and ampicillin (Amp, 100 μg/mL) and incubated in a 37°C humidified 5% CO_2 / 95% air atmosphere. At

pre-selected time points (4, 24, 48 and 72 hours) the media was aspirated off the scaffolds and the OBs were rinsed twice with 1X phosphate-buffered saline (PBS) in preparation for determining cell proliferation.

3.4 Colorimetric Bioassays

Colorimetric bioassays, such as crystal violet (CV), were developed to study cell proliferation and cytotoxicity.[126, 127] Some colorimetric assays were designed to detect the activity of living cells versus dead cells and generate a colorimetric signal based on the activity level.[126] Colorimetric bioassays are radioisotope-free and allow for rapid detection and precise measurements. They have been well cited in the literature for determining cell proliferation on PS substrates.[127-131] These methods involved variations of staining cellular DNA and RNA with CV. Once stained, the excess CV was rinsed off, the adherent stain was extracted from the DNA and RNA and the absorbance was measured using a spectrophotometer.

The reported success of CV colorimetric assays measure the proliferation of cells cultured on plastic culture wells.[127-131] PS culture wells do not absorb additional CV stain and thus during rinsing the excess stain is removed. Staining cells cultured on different substrates, such as HA, presents a greater challenge than PS culture wells. Ceramic materials are very absorbent and thus absorb a greater amount of CV stain than can be rinsed off. In a preliminary investigation, it was found that dS and pf57 scaffolds (without cells) absorbed CV stain to an extreme, leaving a significant amount of stain adhered to the HA post numerous rinses. To combat this issue, the absorbance of the extracted stain was measured and used as a background. This background could then be subtracted from

the absorbance data determined from the scaffolds with cells. Subtracting the background data was successful on the dS scaffolds as only minimal stain remained.[26]

Using the background subtraction method was not feasible for porous scaffolds because 1) a large quantity of excess stain was trapped within the pores post rinsing, and 2) the non-uniform pore distribution of the pf57 scaffolds resulted in variable quantities of stain being trapped within the pore structure. Thus, when the background data was collected and subtracted from pf57 scaffolds with cells, proliferation results indicated negative cell growth. Therefore, the results were inconclusive and the CV colorimetric assay is not useful for quantifying cell proliferation.

3.5 DNA Quantification

DNA quantification is another method used to measure cell proliferation on plastic substrates. This technique, developed in the early 1980's by Labarca and Paigen, uses an immunofluorescent dye, bisbenzimidazole Hoechst 33258, to bind to and fluoresce the DNA. The discovery of Hoechst 33258 for DNA quantification has proven beneficial for two reasons. First, Hoechst 33258 binds only to deoxyribonucleoprotein found within DNA, and therefore, there would not be any interference from fluorescing RNA, as was found with the use of ethidium bromide.[132] Cells contain a set amount of DNA within the nucleus and a varying amount of RNA. Having the Hoechst 33258 binding solely to DNA enhances the precision of quantifying cell growth. Second, Hoechst 33258 binds to deoxyribonucleoprotein found within the DNA. Thus, if the DNA was dissociated from the chromatin structure, the deoxyribonucleoprotein would still be accessible to bind to the Hoechst 33258.[132] These reported advantages of the DNA

quantification method led Labarca and Paigen to predict that their method could quantitate DNA down to 10 ng, equivalent to a few thousand cells.[132]

Two variations to the method developed by Labarca and Paigen were attempted to study OB proliferation on dS and pf57 scaffolds. The first method used 10mM EDTA (pH 12) to lyse the cells in place. The DNA was homogenized within the lysis buffer by pipetting and then the DNA-concentrated buffer was collected and stored at -80°C for the duration of the study. At the end of the study, the collected DNA was thawed, briefly sonicated and quantified using a fluorometer. The first challenge arose when lysing the cells off the various substrates. Collecting the DNA off the PS was fairly straightforward. OBs on the PS substrate were observed lysing under the microscope (Figure 17). When the DNA-concentrated buffer was collected, the empty PS well was stained with immunofluorescing DNA dye (Hoechst, Molecular Probes #6505). There was no fluorescing DNA remaining in the PS well, thus verifying all the DNA was collected into the lysis buffer. Lysis buffer was also added to both the dS and pf57 scaffolds. In order to fully coat the scaffolds, addition buffer was required. Just enough buffer was added to sufficiently agitate the scaffold; ensuring buffer was coating all areas of the scaffolds. The DNA-concentrated buffer was then collected off the dS and pf57 scaffolds. To verify all DNA was collected, the dS and pf57 scaffolds were stained with immunofluorescing DNA dye (Hoechst, Molecular Probes #6505). However, when imaged under the microscope, fluoresced DNA was observed within the porous structure of the pf57 scaffold and imbedded within the surface of dS (Figure 18). A significant amount of DNA remained on the scaffolds post collection of the lysis buffer.

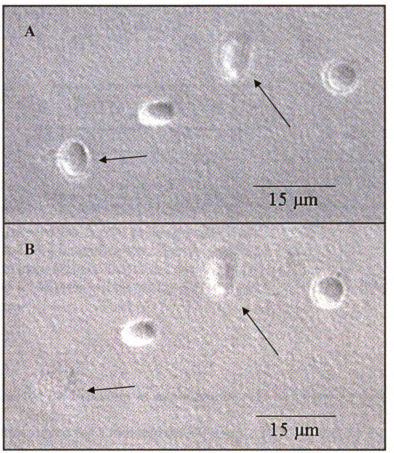

Figure 17: This micrograph depicts OBs cultured on polystyrene for 8 hours, coated with 300μL of 10mM EDTA (pH 12) Lysis buffer. The four cells, seen in A, have started taking on water to adjust to the high pH lysis buffer. As the cells continuously increase the water content, the cell membranes reach their holding capacity and eventually lyse (B). Cell in process of lysing are indicated with the arrows. There is a 20 second time lapse between image A and image B. A and B were imaged at 400X magnification.

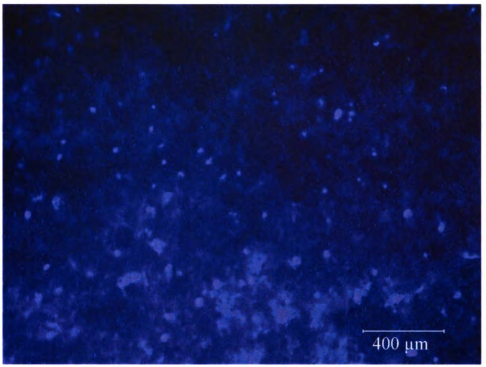

Figure 18: Fluoresced DNA post soaking and agitation of 10mM EDTA lysis buffer on pf57 scaffold at 100X magnification. The above image is a representative image of the scaffold. Five images were collected for each scaffold and three trials of n = 3 scaffolds were conducted at different times using different passages of OB cells. The scale bar represent 400 µm.

To adjust for the difficulty in extracting the DNA off the dS and pf57 scaffolds the OBs were trypsinized for 3 minutes before being collected. The cells were spun down (3000 rpm for 10 minutes) and the trypsin was aspirated off the cells. The pf57 cells generated a visual cell pellet, while the dS scaffolds did not. The trypsinized scaffolds were then rinsed twice in PBS and stained with Rhodamine immunofluorescing actin dye (Molecular Probes Rhodamine-Phalloidin). This immunofluorescent dye fluoresces the actin filament present within the cytoskeleton of a cell. Few cells were observed on the trypsinized dS scaffold (Figure 19) suggesting 1) the scaffolds were not trypsinized long enough and 2) the attachment strength of OBs to the dS is greater than the attachment

strength of the PS. No cells were observed on the PS substrates via actin immunofluorescing after a 3-minute trypsinization. A significant amount of cells were present within the pores of pf57 after trypsinization (Figure 19). The capillary forces generated by the surface tension between the HA porous scaffold and the trypsin could prevent the trypsin from infiltrating the pores and thus not wetting the OB cells.[133]

Another explanation for seeing such a large number of OBs remaining could be because of a strong attachment of the OBs to the pf57 scaffold. The pf57 scaffolds have an increased surface roughness which has been shown to increase the OB attachment.[62, 65, 134] Based on these results, trypsinizing the OBs off the scaffold to collect the DNA was successful for the dS scaffolds. However, there are not enough cells for an accurate count to quantify the DNA from the OBs from the porous scaffolds by trypsinization, and it is too difficult to remove the OBs from the porous scaffolds. Thus, DNA quantification is not an appropriate method for quantifying OB proliferation on pf57 scaffolds *in vitro*.

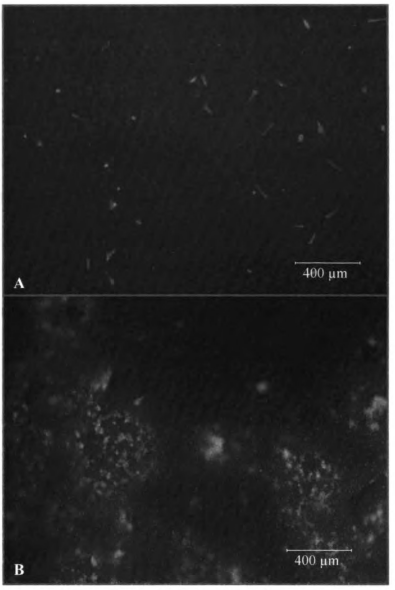

Figure 19: Immunofluorescent actin stain of OBs on dS and pf57 scaffolds cultured for 4 hours. These images depict the remaining OBs on the dS (A) scaffold and pf57 (B) scaffold after a 3-minute trypsinization and 10-minute spin at 3,000 rpm. This image demonstrated trypsinization as a suitable method for removing OBs off the dS scaffold (A). The image of the porous scaffold illustrates a significant quantity of cells remaining within the pore, suggesting trypsinization is not a suitable method for removing OBs from the inner pores of the scaffold. A and B were imaged at 50X magnification. The above images are representative images of the scaffolds. Five images were collected for each scaffold and three trials of n = 3 scaffolds were conducted at different times using different passages of OB cells. The scale bars represent 400 µm.

Figure 20 shows the proliferation results quantified using this modified DNA quantification. The significantly low quantities of DNA per surface area for the pf57 scaffolds confirm the DNA was not fully extracted from the scaffolds when the lysis buffer was collected. The significant variation between trials and the atypical OB proliferation behavior, as indicated for the dS scaffolds and control substrate, demonstrated these results are not conclusive and that variations between measurements also suggest this procedure is not robust.

Before additional HA scaffolds were tested to determine if DNA quantification was an appropriate method for studying OB proliferation, preliminary trials were conducted on plastic. In the process of designing the plastic control preliminary trials, modifications to the previous procedure were made. These modifications are as follows: the OBs were trypsinized from the substrates, the OBs were spun down and the trypsin was aspirated off the pellet. Phosphate buffer saline was then added to the cells; they were sonified, frozen until the completion of the study, thawed and quantified using a fluorometer. To verify that the changes within the new method would not affect the DNA results previous collected, a DNA quantification trial was run on the same fluorometric reader using the same DNA concentrations (fresh stock solutions were made to eliminate the possibility of having a bad standard). The results again were inconclusive, possibly because the reader did not have adequate tolerance to quantify the DNA at the nanogram level. Thus, the procedure was repeated using a more accurate fluorometer. Hemacytometer counts then verified that the problem in obtaining conclusive results was with the DNA measurement itself and not the experimental setup, or with the cells (Figure 21). The consistent results using a different fluorometer confirmed that it wasn't

the fluorometer itself but another problem causing the inconclusive results (Figure 22). After an extensive literature review on using DNA quantification to determine cell proliferation, one common factor stood out – the number of cells seeded per scaffold. The literature reported substrates being cultured with upwards of 200,000 cells per cm^2, a significant increase from the 11,320 OBs per cm^2 cultured on the dS or PS scaffolds.[95, 97, 99] The one advantage to the DNA quantification method was that numerous samples could be tested simultaneously. Needing to see upward to 200,000 cells per cm^2 for each sample to yield sufficient DNA quantification measurements has multiple disadvantages. First, it is neither feasible nor practical to obtain such a large quantity of cells for numerous scaffolds (greater than 25). Second, when cells are seeded with that high of a cell density, the cells would be confluent by the time they were all attached. Once cells are confluent, their close proximity cause localized changes in cell signaling, altering the cell behavior and therefore the original intent of studying OB proliferation is lost. Therefore, although the DNA quantification method originally showed promise as a means to quantify OB proliferation, after much trial and error, it was discovered that this technique is not practical for this application.

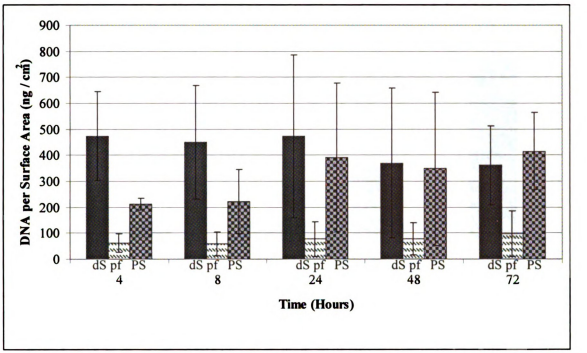

Figure 20: DNA quantification results for the dS (solid black), pf57 (white hashed) and PS (black and gray checkered). First, as observed by wide distribution of the standard deviation, there is significant variation between scaffolds which demonstrates this procedure of DNA quantification is not robust. Secondly, the calculated surface area for the pf57 scaffolds is 10 fold the surface area of dS and PS substrates, and cells were plated on the scaffolds per surface area, therefore pf scaffolds should potentially have more DNA. However, this study indicates a small, low quantify of DNA present for pf57 scaffold confirming the all the DNA was not extracted from the porous scaffolds because Figure 19 shows that cells do attach to pf scaffolds. Finally, the proliferation of the OBs on dS and PS over 72 hours is not indicative of common OB behavior on these scaffolds. Three trials of $n = 3$ scaffolds were conducted at different times using different passages of OB cells and the Y-error bars represent the standard error.

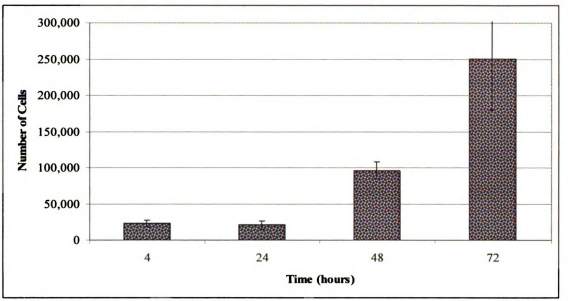

Figure 21: Hemacytometer preliminary data for DNA quantification. Results demonstrated typical OB proliferation behavior on PS. This verifies the inconclusive results obtained from the DNA quantification method are related to the DNA measurements themselves and not the experimental setup or a cell problem. Three trials of n = 3 scaffolds were conducted at different times using different passages of OB cells and the Y-error bars represent the standard error.

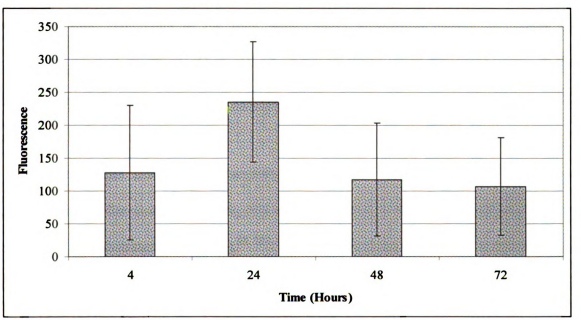

Figure 22: DNA quantification data for the corresponding hemacytometer data for OB proliferation on PS. Results are inconclusive, much like the previously tested DNA quantification method. Three trials of n = 3 scaffolds were conducted at different times using different passages of OB cells and the Y-error bars represent the standard error.

3.6 Hemacytometer

Another method for quantifying cell proliferation is by manually counting the cells. This is achieved by using a hemacytometer (Appendix A), a tool originally developed to count blood cells in a known volume of blood.[135] This tool has grown in popularity and is common among most cell culture labs, used when splitting cell cultures. The hemacytometer is also useful for proliferation studies. There are many benefits to counting with a hemacytometer. It is simple, effective and widely accepted as a suitable method for making cell counts.[136] In addition, a hemacytometer can be used with cell viability assays (such as Trypan Blue) to determine the morbidity rate of cells within a culture.[137]

Using a hemacytometer to manually count cells was another method tested to measure OB proliferation of dS and pf57 scaffolds. By this method, cells were detached from the scaffold with 1% Trypsin-EDTA, rinsed with complete media and transferred to a conical tube. The cells in the tube were evenly suspended within the media by repetitive, manual pipetting. Then, 10 μL were injected under the glass slide of the hemacytometer, and the cells were counted under the phase contrast microscope at 10x magnification (Appendix A).

The results from the hemacytometer count are consistent with the findings presented in the literature, suggesting this method is suitable for quantifying proliferation on dS and PS substrates (Figure 23).[95, 127, 136] Further analysis on the proliferation results for dS scaffolds will be discussed in Chapter 4. The proliferation data for the pf57 scaffolds, obtained using the hemacytometer, was inconclusive. Similar to the DNA quantification assay, removing the cells from the intricate porous structure proved unsuccessful by trypsinization.

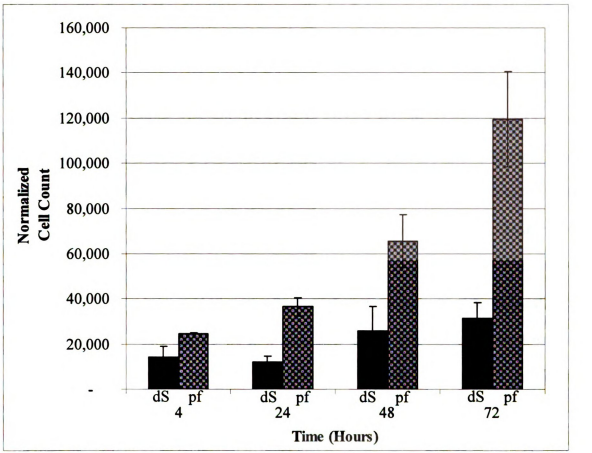

Figure 23: The graph depicts hemacytometer results of OB proliferation on dS (black) and PS (black and gray checkered) substrates over 72 hours. These results are consistent with findings presented in the literature, confirming hemacytometer measurements are a suitable method for quantifying OB proliferation on dS and PS.[26] Three trials of n = 3 scaffolds were conducted at different times using different passages of OB cells and the Y-error bars represent the standard error.

3.7 Immunofluorescent Imaging

Imaging cells is another common method used in proliferation studies.[23, 138, 139] Immunofluorescent imaging is a useful tool for studying cell morphology and with the aid of the appropriate computer software, cell proliferation can be quantified.[140] Straightforward immunofluorescent imaging of cells however offers qualitative and not quantitative proliferation results. The actin and nuclei of the cells were stained with

Rhodamine (Red) and Hoechst (Blue), respectively. Prior to staining, OBs were fixed with 3.7% formaldehyde for 10 minutes. The fix was extracted with 0.1% Triton X-100 surfactant for 5 minutes. The cells were then pre-incubated for 30 minutes in a 1% solution of Bovine Serum Albumin (BSA) in 1XPBS. A rhodamine-phalloidin solution (consisting of 5μL of stock solution diluted into 200μL of 1% BSA in 1XPBS) was then added and the scaffolds were incubated at room temperature for 20 minutes under dark conditions. Following a PBS wash, Hoechst stain was added and the scaffolds were incubated for 15 minutes under the same conditions.

There was an increase in immunofluoresced actin on both dS and pf57 scaffolds over 72 hours (Figure 24 and Figure 26). Immunofluorescent imaging can be a useful, qualitative method for determining OB proliferation of both dS and pf57 scaffolds. However, only the actin was immunofluoresced in this study. An increase in observed actin over the 72 hours can be related to other cell phenomena such as apoptosis, necrosis or cell spreading, in addition to cell proliferation. Immunofluorescent staining of the cell nuclei would be a more accurate way to observed cell proliferation as the number of cell nuclei is directly related to the number of cells. However, obtaining a direct count of nuclei via immunofluorescent imaging is extremely challenging on 3-dimensional scaffolds. In addition, nuclei immunofluorescent, Hoechst stain, bind to CaP.

Immunofluorescent imaging can also be useful for understanding of OB attachment and proliferation on the porous scaffolds. Various immunofluorescent images as well as phase contrast images of the same image can be overlaid on one another to depict cell positioning with respect to the pores. The first combined image overlays the fluoresced actin filament with the fluoresced nuclei (Figure 26). This provides spacial

orientation of the nucleus within the cell cytoskeleton. The second combined image uses the phase contrast imaging (Figure 27A) with immunofluorescent imaging of the cell nuclei simultaneously (Figure 27B). OBs were found to be located both on the pf57 surface and within the pores. As seen in Figure 27C, actin becomes more concentrated (or brighter) around the pore edges. This behavior suggests migration of the OBs into the pores. Another possibility is that the OBs could be attaching cells along the pore walls and based on the imaging angle, the actin appears to be more concentrated within the wall regions. Combining a phase contrast image with an immunofluoresced image of the actin filament was not as successful as the immunofluoresced image of the cell nuclei. Immunofluorescent imaging has proven to be a very useful and valuable tool for qualitatively observing OB proliferation, observing various OB morphologies (as will be further discussed in Chapter 4) and establishing the spacial orientation of the OBs with respect to the pores.

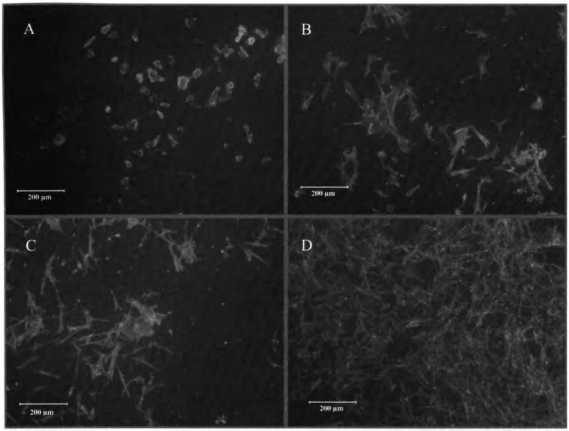

Figure 24: This figure shows the immunofluoresced actin on OBs attached to dS scaffolds over 72 hours. The proliferation of the OBs is evident for each time points, 4 hours (A), 24 hours (B), 48 hours (C) and 72 hours (D), and demonstrates immunofluorescent imaging is a qualitative method for observing OB proliferation. All images were taken at 100X magnification. The above images are representative images of the scaffolds. Five images were collected for each scaffold and three trials of n = 3 scaffolds were conducted at different times using different passages of OB cells. The scale bars represent 200 µm.

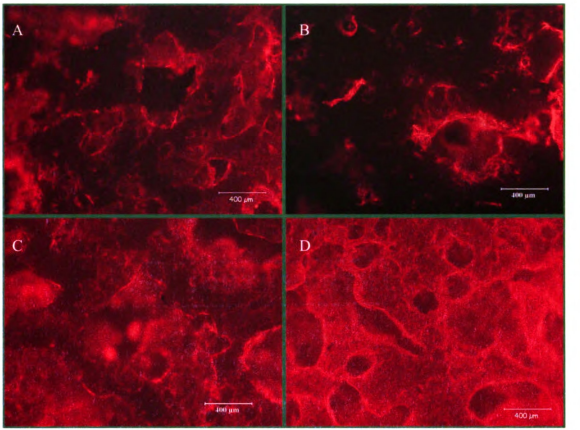

Figure 25: This figure shows the immunofluoresced actin on OBs attached to pf57 scaffolds over 72 hours. The proliferation of the OBs is evident for each time points, 4 hours (A), 24 hours (B), 48 hours (C) and 72 hours (D), and demonstrates immunofluorescent imaging is a qualitative method for observing OB proliferation. All images were taken at 100X magnification. The above images are representative images of the scaffolds. Five images were collected for each scaffold and three trials of n = 3 scaffolds were conducted at different times using different passages of OB cells. The scale bars represent 400 µm.

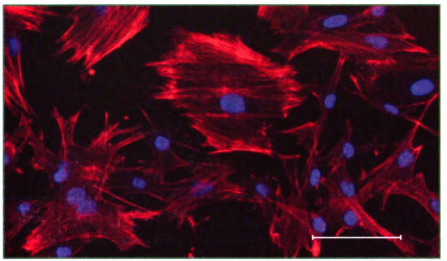

Figure 26: Combine image the fluoresced actin filaments and the fluoresced nuclei of OBs on plastic substrate, at 200X magnification. Scale bar represents 100 μm.

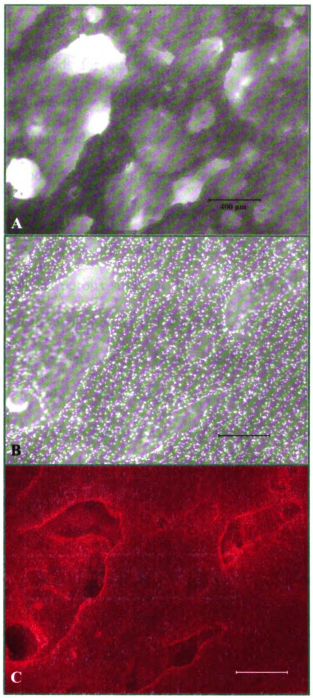

Figure 27: The complexity of OB attachment and proliferation into the pf57 scaffold is illustrated. The phase-contrast image depicts the intricate pore structure of the pf57 scaffolds (A), and when imaged simultaneously to DAPI blue immunofluorescence, the position of the OB nuclei with respect to the scaffold is observed (B). An immunofluorescent actin stain of the same scaffold region confirms the presence of the OBs (B). A, B and C were imaged at 50X magnification. The scale bars represent 400 µm.

3.8 Conclusion

In conclusion, methods for quantifying OB proliferation were examined. The crystal violet colorimetric assay was found to be a useful method for measuring OB proliferation on dS scaffolds and PS because of the ability to rinse off the excess stain and generate a background scan that accommodates for the slight variability between the dS and the PS substrates. This method however was found to be inconclusive for quantifying OB proliferation on the pf57 scaffolds due to the difficulties in rinsing out the absorbed CV stain from the porous structure. Similarly, the pf57 presented difficulties with the DNA quantification method in that once again the complex, intricate porous structure made extracting the DNA (via a lysis buffer) or the OBs (via trypsinization) virtually impossible to obtain an accurate quantification of cell proliferation. Furthermore, other more fundamental problems with the DNA quantification assay were exposed. To establish an accurate growth curve for the OBs on plastic, a significant amount of cells needed to be plated. Contrary to the original prediction there are many factors that affect the amount of DNA that can be detected. One of these factors includes the accuracy of the equipment. In this situation, the fluorometric reader was not robust in detecting nanogram differences in cell numbers, but it was also discovered that for an accurate measurement a significant quantity of cells were needed per scaffold. Such high cell numbers were not practical or feasible for studying proliferation on large quantities of scaffolds. Having established trypsinization fails to remove OBs from the pores of the pf57 scaffolds, the hemacytometer method focused on the robustness of quantifying proliferation on the dS scaffolds. The results from the hemacytometer study demonstrated this method to be a viable technique for quantifying OB proliferation. Immunofluorescing

stain, although not a quantifiable method for studying OB proliferation, could be used to clearly presented qualitative evidence of OB proliferation on both dense (dS) and porous (pf57) scaffolds, provided the staining was based on the cell nuclei. Although in this study, there was an increase in actin filament over 72 hours, it did not confirm cell proliferation. Other phenomena such as cell necrosis, apoptosis or cell spreading could also result from an increase in immunofluoresced actin. Imaging techniques that combine phase contrast images of the porous scaffold with simultaneous immunofluorescent capture the OB positioning with respect to the pores, useful for observing the attachment behaviors of the OBs. Of the methods used to measure *in vitro* cell proliferation on the dense and porous scaffolds, CV assay and hemacytometer measurements were the best for dS scaffolds. The major limitation of the CV assays is the absorbance of excess stain into the scaffold. Hemacytometer measurements are limited by the ability to detach the cell from the substrate surface. Because of these limitations, neither CV assaying or hemacytometer measurements are suitable for quantitative measurements of cell proliferation on porous scaffolds. Immunofluorescent imaging of the cell nuclei is a rough, qualitative method for estimating OB proliferation on the porous scaffolds.

CHAPTER 4

THE IN VITRO EFFECT OF AIR-JET SIEVED HYDROXYAPATITE ON MC3T3-E1 MOUSE OSTEOBLAST CELL DIFFERENTIATION AND PROLIFERATION

4.1 Introduction

Hydroxyapatite (HA) is one of the most researched calcium phosphate (CaP) bioceramics, due to its chemical similarities to natural bone, as well as its osteoconductive and biocompatible properties.[1, 9, 17, 39] Precipitation, a common technique for processing HA powders, yield powders non-uniform in shape, and with a wide particle size distribution.[120, 141, 142] Significant variations within the powder size and shape makes them unsuitable for some biomedical applications.[116] Thus, to make these HA powders more uniform, they are sieved to obtain a narrower particle size distribution. Gravity sieving (G) through a 53 μm sieve, although suitable for removing large particles, fails to remove particles <0.2 μm. Gravity sieving was originally thought to be sufficient for fabricating ceramic implants for medical applications, until it was established that these superfine particles (< 0.2 μm) were found to be problematic, clogging the plasma sprayer used for plasma coating HA onto dental implants.[116]

Air-jet sieving (GJ) gives enhanced quality control by yielding a narrower particle size distribution. During air jet sieving, a stationary wand delivers air upward through a 20 μm sized mesh. To avoid particles clogging the mesh, the sieve screen continuously rotates as a hammer strikes the sieve column, thereby promoting settling of the particles. Simultaneously, a vacuum is used to draw the HA particles through the mesh, into a

separate tube, where the superfine particles are trapped in a HEPA filter and the larger particles are collected for other uses.[116]

The manufacturer reports the average particles size of the G and GJ HA powder to be 34.5 μm ± 19.7 μm and 11.0 μm ± 8.1 μm, respectively.[116] In a study conducted by Sun *et al.*, it was found that differing HA particle sizes affected osteoblast (OB) activities such as proliferation and the OB mean surface area.[140] Concentrations of transforming growth factor-β1 (TGF-β1) and prostaglandin E_2 (PGE_2) were also affected by the HA particle size.[140] However, in Chapter 2, the average grain size of the G and GJ HA when pressed into dense scaffolds was 4.4 ± 0.5 μm and 4.1 ± 0.7 μm, respectively. Fine particles have a high surface to volume ratio, which allow electrostatic and other surface forces to dominate, and form agglomerations of the powder. Agglomeration would explain the discrepancy between the particle sizes, reported by the manufacturer, and grain size results.

Fourier transform infrared spectroscopy (FTIR) results of G and GJ HA powders (as shown in Chapter 2) also indicated peak differences (Figure 6). An additional peak was identified at 1137 cm^{-1} for the GJ powder. This peak may be due to excess HPO_4^{-2} ions, often associated with non-stoichiometric HA. Excess HPO_4^{-2} groups have been observed by Ishikawa and others as a product of HA precipitation using $CaCl_2$, KOH and KH_2PO_4 as reactants, or from calcium deficient HA.[117, 118, 120, 121] Yet another explanation for the additional peak could be the nucleation of a second CaP phase, such as tricalcium phosphate (TCP), octacalcium phosphate (OCP), and dicalcium phosphate anhydrous (DCPA); all of which have characteristic peaks at 1137 cm^{-1}.[143] Chemistry differences, such as those observed by the FTIR, have also been shown to affect OB responses.

This chapter will incorporate the dense and porous scaffolds fabrication process discussed in detail in Chapter 2, with MC3T3-E1 OBs to study the effect of GJ HA on OB proliferation and differentiation. In addition, to the GJ and G powders, this chapter will examine the different Hitemco HA lots (batches) previously used within our research group.

4.2 Materials and Methods

Six different manufacturing lots of HA powder, obtained from Hitemco Medical Applications (Old Bethpage, NY, USA) were processed following a common HA precipitation method. The HA powders were then sieved by either gravity sieving (G) or by combined gravity and air jet sieving (GJ). A simplified identification key for these investigated powders is shown in Table 1.

Identification	Manufacturing Lot Number	Sieving Method
HA-G-A	050897-test	Gravity
HA-G-B	050897-001A	Gravity
HA-G-C	120701-test	Gravity
HA-GJ-D	120701-001A	Gravity and Air jet
HA-G-E	160899-test	Gravity
HA-G-F	101202-test	Gravity

Table 1: Identification key for the various HA manufactured lots obtained from Hitemco and their associated sieving method. The HA powder identified by Hitemco as "test" lots were samples removed from the commercial lot, back stocked and used for verification purposes. The HA powder identified by Hitemco as an "-001A" lot were part of the lot shipped and used for commercial purposes. Therefore, HA-G-A and HA-G-B for all intents and purposes should have originated from the same manufacturing batch.

HA-G-A and HA-G-B powders were precipitation synthesized from the same batch, and both were gravity sieved. The difference in these two powders is HA-G-A powder was gathered from materials reserved for later testing if necessary. HA-G-C and HA-GJ-D were also precipitation synthesized from the same batch. However HA-G-C was set aside after being gravity sieved and HA-GJ-D was then sieved further with an air jet sieve. HA-G-C powder was never air jet sieved. HA-G-E and HA-G-F were precipitation synthesized from two different batches, where both batches have been used for previous research within our group. Both HA-G-E and HA-G-F were gravity sieved only.

4.2.1 Scaffold Preparation

Dense (dS) scaffolds were prepared by uniaxially pressing the HA into a 32 mm in diameter die, as discussed in Chapter 2.2.2. Scaffolds were fabricated using powder from each HA lot as listed in Table 1. Scaffold chemistry and phase purity were evaluated using powder X-Ray diffraction (XRD) and FTIR of both the as-manufactured (AR) HA batches and the prepared scaffolds. The XRD and FTIR powder preparation and material characterization techniques are defined in Chapter 2.2.4 to 2.2.5. The dS scaffolds were imaged, at 1500x magnification, using a scanning electron microscope (SEM, Chapter 2.2.6) and the images used to determine grain size, by the line intercept method.[113] Surface roughness (R_a) of the all dense scaffolds was measured (Chapter 2.2.8) and using one-way ANOVA analysis with a Tukey post-hoc test, the statistical significance of Ra was considered if $p<0.05$. Prior to cell culture, the scaffolds were autoclaved sterilized and prepared for cells as discussed in Chapter 3.2. Dense scaffolds

from each lot were used for OB differentiation studies. Scaffolds HA-G-B and HA-GJ-D were used as the culture substrate for the proliferation study.

Porous foamed scaffolds with 57 ± 4.5% porosity (pf57) were fabricated from HA-G-B and HA-GJ-D powders as was discussed in Chapter 2.2.3. Scaffold chemistry and phase purity were evaluated in Chapters 2.2.4 and 2.2.5 using XRD and FTIR of the AR batches and the prepared scaffolds. The pf57 scaffolds were imaged using an SEM (Chapter 2.2.6), and the images were used with SPOT Imaging software to determine the macro- and micropore sizes of the porous scaffolds. Prior to cell culture, the scaffolds were autoclave sterilized and prepared for cell culture as discussed in Chapter 3.2. Porous scaffolds were used to evaluate OB differentiation and to assess OB proliferation.

4.2.2 Cell Preparation

The MC3T3-E1 OBs were prepared for the differentiation and proliferation studies as discussed in detail under Cell Culture, Chapter 3.3.

4.2.3 Cell Differentiation

MC3T3-E1 OBs were seeded on the dS scaffolds from each lot (3x n = 3) at a density of 30,000 cells per cm^2.[138] The cells were fed with 7 mL of complete media supplemented with antibiotics (1% Penicillin-Streptomycin, #15070063, Invitrogen, Grand Island, NY). Upon confluency, the OBs were fed with 7 mL of differentiation media, which consisted of the antibiotic nourished complete media further supplemented with 10 mg/mL ascorbic acid (#A2218, Sigma, St. Louis, MO, USA) and 216 mg/mL β-

glycerol phosphate (#G9891, Sigma, St. Louis, MO, USA). The OBs were fed daily with differentiation media for 14 days. On day 14, alkaline phosphatase (AP) activity was determined.[26] Polystyrene culture wells (PS) were used as the control substrate.

To determine the AP activity, the AP activity yielded red stain, and then quantified using a spectrophotometer. First, the scaffolds were rinsed in 1X phosphate buffer saline solution (PBS), and then fixed in 2% paraformaldehyde for 10 minutes, followed by a rinse in 0.1 M cacodylic buffer. The fixed cells were incubated for 30 minutes at 37°C in a solution containing 0.5 mg/mL naphthol AS-MX (#N5000, Sigma, St Louis, MO) dissolved in N,N dimethalformamide (#D4245, Sigma) and 1.0 mg/mL fast red TR salt (#F8764, Sigma) in 0.2 M Tris buffer (pH 8.4). Following the 20-minute stain, the fixed cells were rinsed twice with 0.1 M cacodylic buffer, and stored in 0.1 M cacodylic buffer at 4°C.[26] To quantify the enzyme, the cacodylic buffer was aspirated off the scaffolds, the cellular matrix was carefully removed from the discs by gently scraping, and the cellular matrix was placed in 6-well culture plates. The precipitated salt from the AP activity staining was solubilized in 100% trichloracetic acid (TCA) under gentle agitation at room temperature for 24 hours. The solubilized salt was further diluted with TCA in a 1:2 ratio. The absorbance of the solubilized salt was measured with a spectrophotometer at a wavelength of 540 nm. TCA was used as the reference solution. A one-way ANOVA analysis with a Tukey post-hoc test was performed on the quantified AP activity, and statistical significance was determined if $\rho < 0.05$.

MC3T3-E1 OBs were seeded on the pf57 scaffolds fabricated from HA-G-B and HA-GJ-D powders (3x n = 3) at a density of 31,000 cells per cm^2. PS was used as the control substrate. The cells were fed with 7 mL of completed media supplemented with

antibiotics, 1% Pen-Strep. Upon confluency, the OBs were fed with 7 mL of antibiotic supplemented differentiation media. After 14 days of cell culture, the AP activity was stained in the same manner as the dS scaffolds.[26]

4.2.4 Cell Growth

Cell growth was measured on both dS and pf57 scaffolds fabricated from HA-G-B and HA-GJ-B powders. MC3T3-E1 OBs were seeded on the scaffold (3x n=3) at a density of 30,000 cells per cm^2. PS was used as the control substrate. Cell proliferation was measured at 4, 24, 48 and 72 hours. OB proliferation on the dS scaffolds and PS substrate was quantified by a hemacytometer count, as detailed in Chapter 3.6 and qualified by immunofluorescent imaging, as detailed in Chapter 3.7. Proliferation on the pf57 scaffolds was qualified by immunofluorescent imaging.

4.3 Results and Discussion

The bulk chemistry of each lot was evaluated using powder XRD. From the XRD scans of the AR powders, all peaks were identified as the characteristic HA peaks, and were verified by referencing against the Joint Committee of Powder Diffraction Standards (JCPDS) PDF# 09-0432. Characteristic HA peaks were identified on XRD scans for the dS scaffolds of each lot and were verified when referenced against the AR powder XRD scans and the JCPDS PDF# 09-0432. The characteristic HA peaks present within the dS XRD scans confirm that the HA phase was maintained during processing and sintering of the scaffolds. However, a weak additional peak was detected on the XRD scans for dS HA-G-B and dS HA-G-E at 29.6 2-θ. This additional peak could be the

result of the nucleation of a second CaP. HA is stable at a temperature of 1360°C, when sintered under a partial water pressure.[13, 123] Thus, variations to the sintering atmosphere could be a catalyst for the nucleation of a second CaP phase, such as tetracalcium phosphate, tricalcium phosphates, monetite and calcium oxide/ tetracalcium phosphate mixtures.[123] There were slight differences in the peak-to-peak height ratio of the dS scans as compared to the AR scans, suggesting slight chemistry variations occurred during sintering. In addition, peak broadening was evident on all dS scans, which signify a decrease in the crystallinity of the HA, as a result of sintering. de Groot *et al.* noted the importance of Ca/P ratio, where slight variations in the ratio could indicated the presence of other thermodynamically stable apatites, such as tetracalcium phosphate, tricalcium phosphate and calcium oxide.[123]

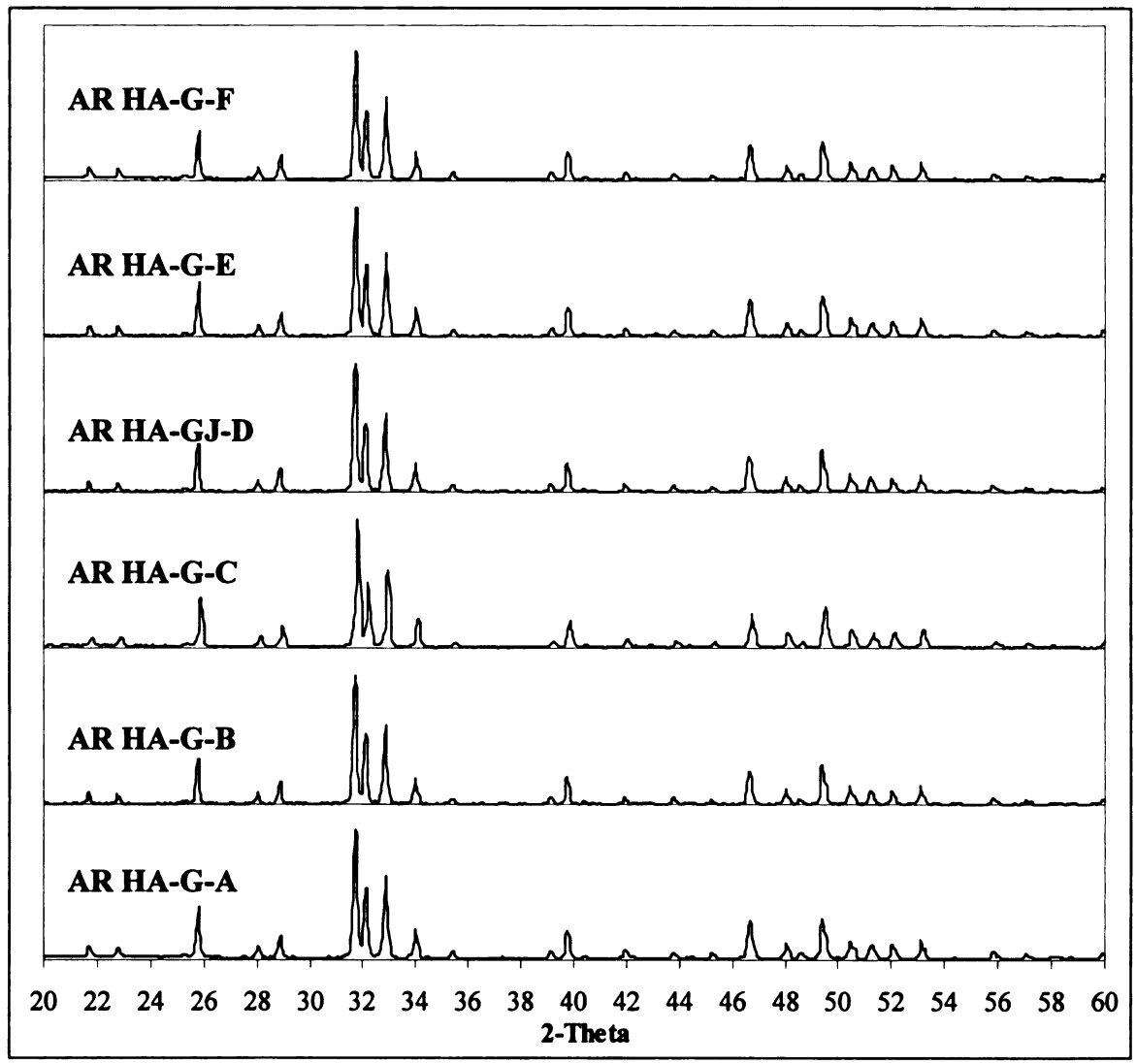

Figure 28: Shows the XRD scans of the AR powders from each lot number. All characteristic HA peaks are identified as HA and confirmed when referenced to the JCPDS PDF# 09-0432. Each scan represents one scan from three independent samples scanned for each scaffold type.

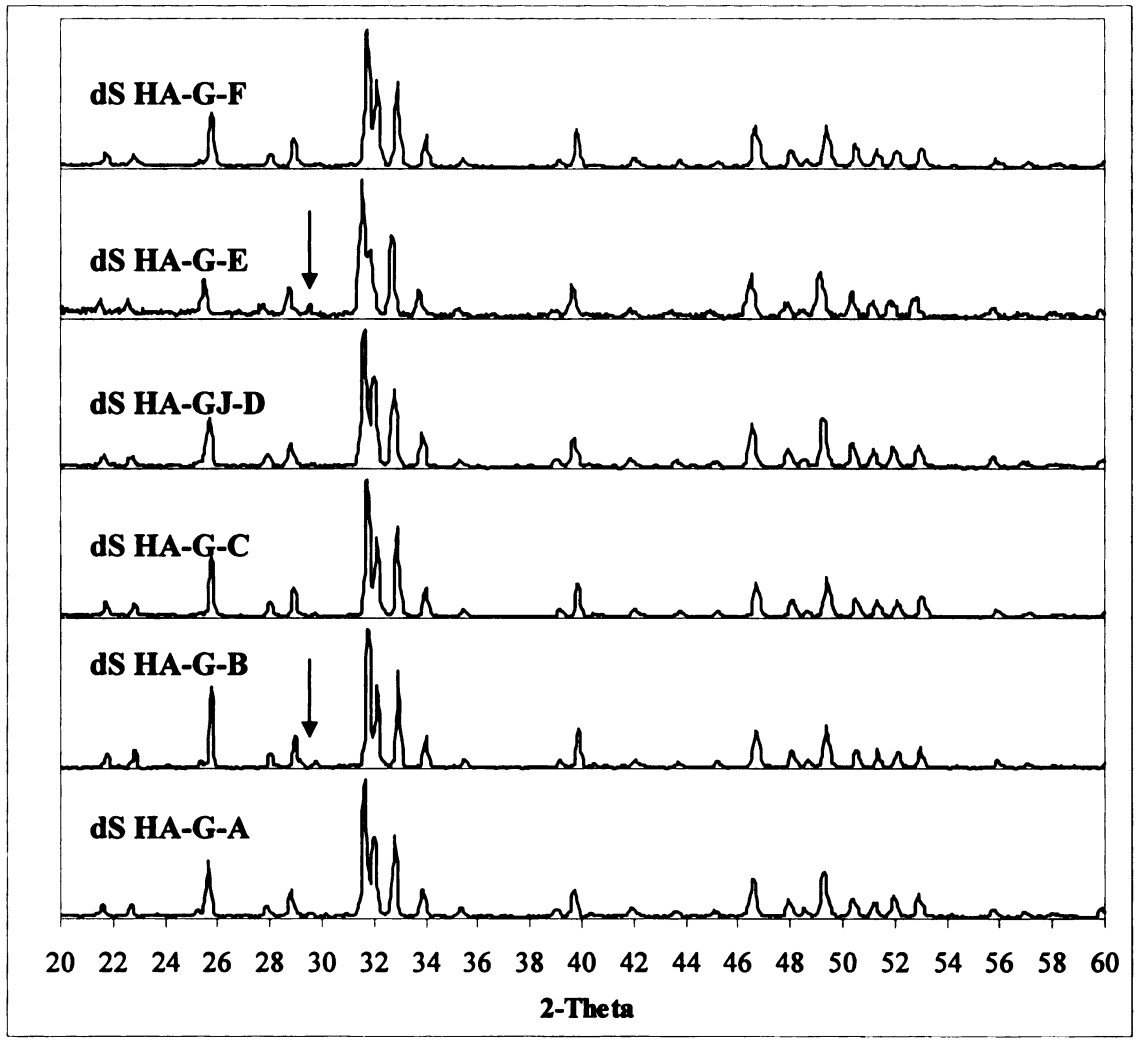

Figure 29: This figure depicts the XRD scans of each dS powder. The characteristic HA peaks are identified according to JCPDS PDF# 09-0432 and the AR control scans. The observed peak-to-peak height ratio differences suggests slight variations within chemistry of the HA. Peak broadening is evident on all scans, and signifies a decrease in the crystallinity of the HA. A small, additional peak was observed on the dS HA-G-B and dS HA-G-E scans at 29.6° 2-θ. Each scan represents one scan from three independent samples scanned for each scaffold type.

The FTIR scans from each lot of the AR powders demonstrated the characteristic triply asymmetric stretching modes of ν_3 P-O bonds of the HA phosphate group at 1022, 1044 and 1087 cm^{-1} (Figure 30 and Figure 31).[55, 117-119] In addition, the peak present at 962 cm^{-1} was identified as a weak symmetric stretching ν_1 P-O bonds, also associated with the HA phosphate group (Figure 30 and Figure 31).[117-121] There were observed differences between the FTIR scans of the different AR HA lots. Peak–to–peak height ratio differences and the absorbance strength differences were observed which would suggest slight variations in the powder chemistry and crystallinity confirming the findings from the XRD data. The FTIR scans of the dS scaffolds also demonstrated peaks at 962, 1022, 1044 and 1087 cm^{-1}, characteristic of HA. There are slight differences in the peak-to-peak height ratio and the absorbance strength of the dS scaffolds that suggest slight powder chemistry variations of the HA and varying degrees of crystallinity between the different HA samples. However, as compared to the AR FTIR scans, the peak-to-peak height ratios and absorbance strengths of the various dS scaffolds are more consistent then those of the respective AR powders (Figure 30 and Figure 31).

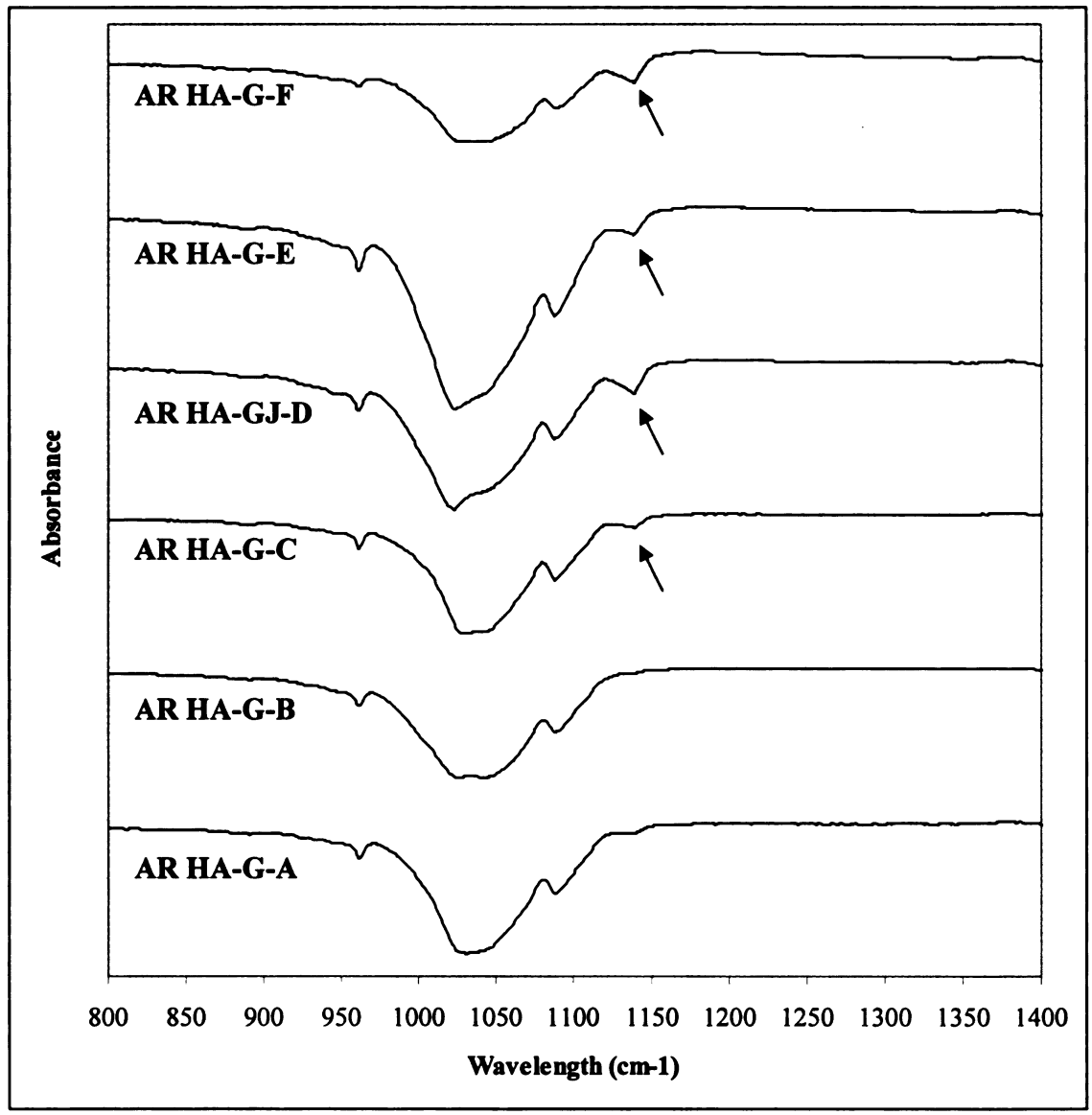

Figure 30: The FTIR scans of the AR HA powders demonstrate the characteristic triply asymmetric stretching modes of ν_3 P-O bonds of the HA phosphate group at 1022, 1044 and 1087 cm^{-1}.[55, 117-119] The peak present at 962 cm^{-1} was identified as a weak symmetric stretching ν_1 P-O bonds, also associated with the HA phosphate group.[117-121]The FTIR results of the different AR scans indicate slight differences in the relative absorbance and the peak-to-peak height ratio, demonstrating slight chemistry variations between the different HA powders. These variations are indicative of the manufacturing process, since the variations are observed all the AR powders. An additional peak present at 1137 cm^{-1} is observed on the HA-G-C, HA-GJ-D, HA-G-E and HA-G-F scans. HA-GJ-D demonstrated the largest absorbance of the other powders. Each scan represents one scan from three independent samples scanned for each scaffold type.

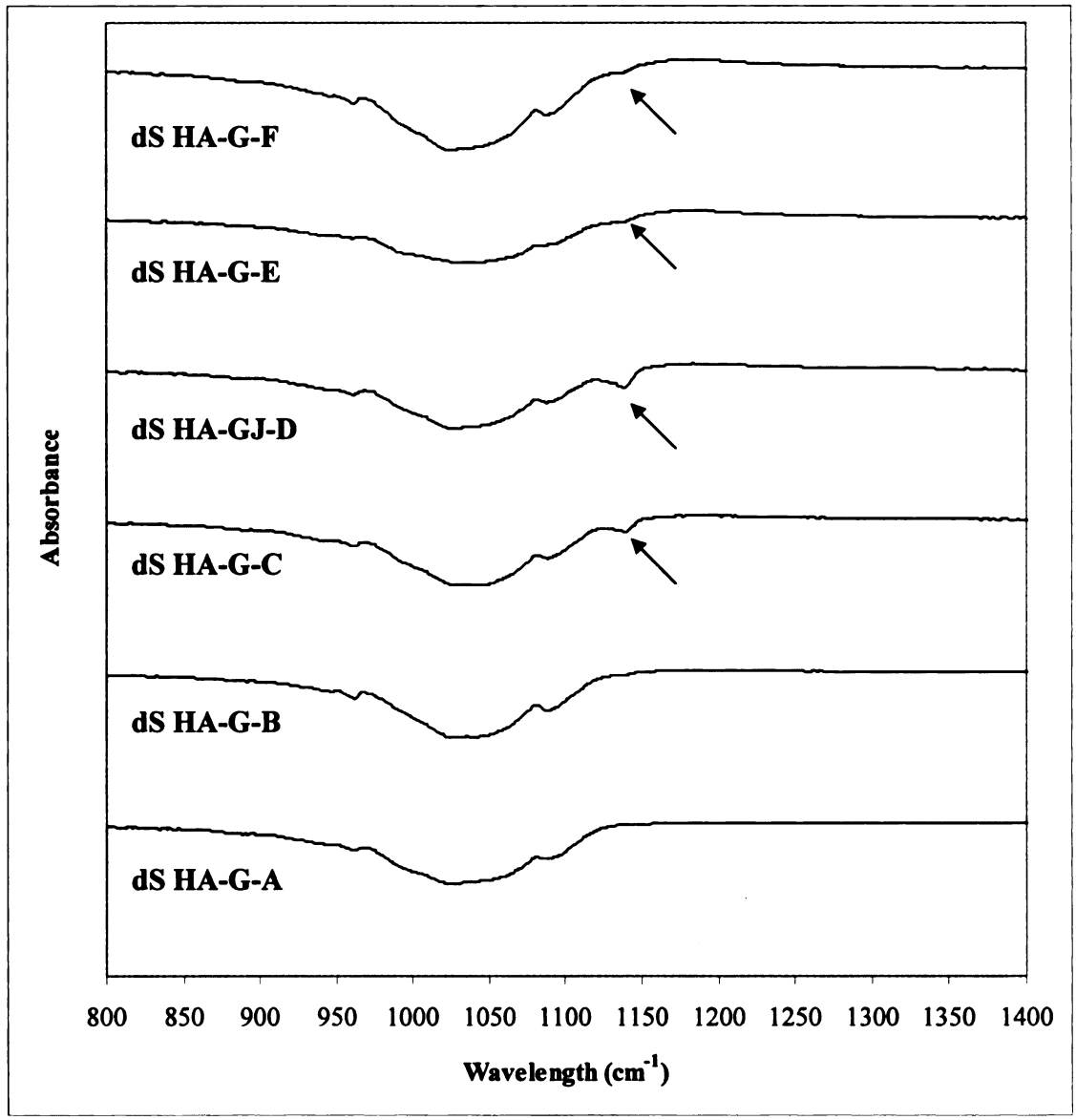

Figure 31: This figure shows the FTIR results of the dS HA powders. All scans demonstrate characteristic triply asymmetric stretching modes of ν_3 P-O bonds of the HA phosphate group at 1022, 1044 and 1087 cm^{-1}.[55, 117-119] The peak positions of the dS HA powders are comparable to the AR HA powders, but the relative absorbance of the dS HA decreases and the peak-to-peak height ratios also change. These changes in the dS HA, occur as a result of sintering and verify a decrease in the crystallinity and variations to the chemistry. The additional peak at 1137 cm^{-1}, identified in the AR HA-G-C, HA-GJ-D, HA-G-E and HA-G-F powders is also identifiable in the dS powder. This peak has the greatest absorbance for the HA-GJ-D powder than the other peaks identified at 1130 cm^{-1}. Each scan represents one scan from three independent samples scanned for each scaffold type.

SEM images were used to calculate the grain size the line intercept method (Figure 32). The average grain size (± standard deviation) was determined be 4.0 ± 0.6 μm, 4.4 ± 0.5 μm, 2.9 ± 0.4 μm, 4.1 ± 0.7 μm, 4.1 ± 0.6 μm, and 4.3 ± 0.6 μm, for HA-G-A, HA-G-B, HA-G-C, HA-GJ-D, HA-G-E, and HA-G-F, respectively.

The surface roughness of the dS scaffolds was determined to be 0.371 ± 0.018 μm, 0.336 ± 0.028 μm, 0.465 ± 0.015 μm, 0.266 ± 0.016 μm, 0.274 ± 0.022 μm, 0.347 ± 0.013 for HA-G-A, HA-G-B, HA-G-C, HA-GJ-D, HA-G-E, and HA-G-F, respectively. The surface roughness of the polystyrene plastic control dishes was also measured as a reference for cell culture, and the Ra was 0.007 ± 0.006 μm. The Ra results of each dS scaffold were determined to be statistically using one-way ANOVA with a Tukey post-hoc test ($p<0.01$)

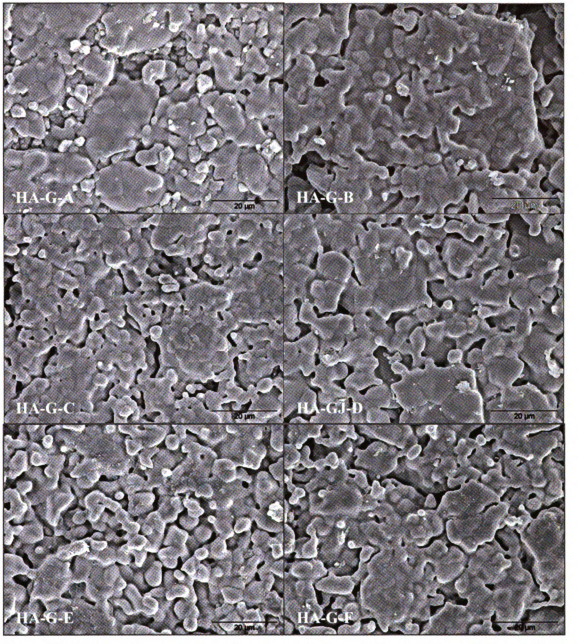

Figure 32: SEM micrograph depicting the grain boundaries of dS scaffolds, at 1500x magnification. The average grain size (± standard deviation) for each scaffold was calculated using the line intercept method and the results are as follows, 4.0 ± 0.6 µm, 4.4 ± 0.5 µm, 2.9 ± 0.4 µm, 4.1 ± 0.7 µm, 4.1 ± 0.6 µm, and 4.3 ± 0.6 µm for HA-G-A, HA-G-B, HA-G-C, HA-GJ-D, HA-G-E, and HA-G-F, respectively. Scale bar represents 20 µm.

OBs cultured on the dS scaffolds for 14 days were fixed and stained for the alkaline phosphatase activity, a marker of OB differentiation. The AP activity was

present on all dS scaffolds as depicted in Figure 34. The AP salt was dissolved in TCA to quantify the amount of enzyme present on the scaffolds. The results of the AP quantification for each of the dS scaffolds and the PS were evaluated using one-way ANOVA with a Tukey post-hoc test, and no statistically significant difference in the amount of AP present on the dS scaffolds and PS substrate.

Since there was no statistically significant difference in the amount of AP present at day 14 for the dS scaffolds, it can be concluded that the production of the AP activity (at day 14) was not affected by the air-jet sieving process; it can be concluded that the AP activity (at day 14) was not affected by the slight HA chemistry variations between lots; and it can be concluded the production of the AP activity (at day 14) was not affected by the additional peak, identified on the FTIR scans for HA-G-C, HA-GJ-D, HA-G-E, and HA-G-F scaffolds. In addition, there was also no correlation between the surface roughness, for each dS HA type, and the amount of AP activity present on the scaffolds. These results however do not conclusively prove that OB differentiation is not affected by these factors.

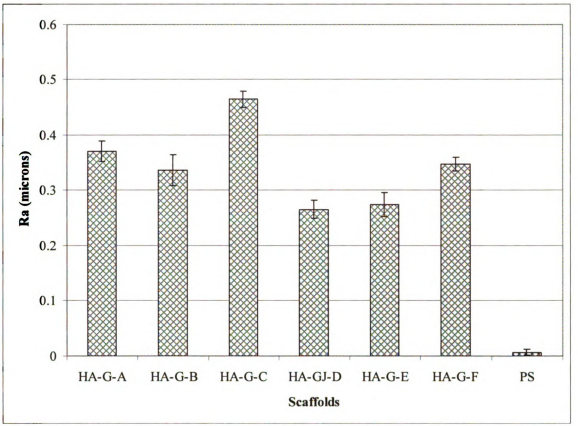

Figure 33: This bar graph depicts the surface roughness of the dS HA scaffolds and plastic control (PS). Three trials of n=3 were conducted at different times using different passages of OB cells. The Y-error bars were determined from the standard error of the mean. ANOVA one-way analysis with a Tukey post-hoc test determined a statistically significant difference between all scaffolds ($p < 0.01$).

AP staining was also used as a marker for OB differentiation on pf57 scaffolds. The pf57 scaffolds require an extremely large quantity of cells as a result of the scaffolds large surface area. OB differentiation was study on the HA-G-B and HA-GJ-D scaffolds. These two HA lots were selected because they were intended for commercial purposes. At day 14, the cells cultured on the pf57 scaffolds were fixed and stained for the AP activity present (Figure 36). The faint red stain observed along the scaffold edges suggests that some AP activity is present on the scaffold. However, by visual observation,

the signal strength of the stained AP on the pf57 scaffolds (Figure 36) is much less then the dS scaffolds (Figure 34).

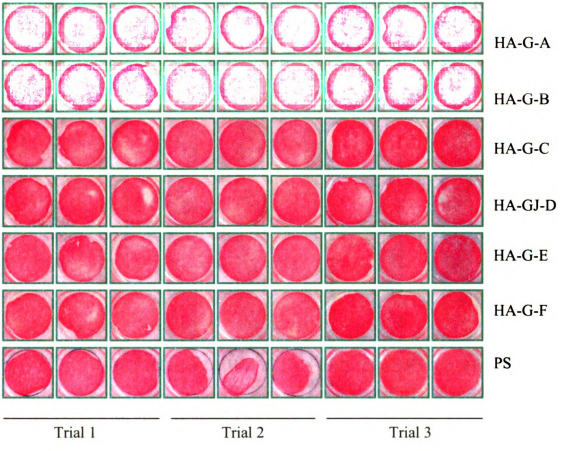

Figure 34: Digital images depict the red stained AP activity (30 minute reaction time) on dS HA scaffolds and PS substrates after 14 days culture of MC3T3-E1. Three trials of n=3 were conducted at different times using different passages of OB cells. The enzyme as seen by the stain uniformly coats the scaffolds for each trial. The HA discs are 32 mm in diameter. The control cells were cultured on in a 6-well PS culture plate.

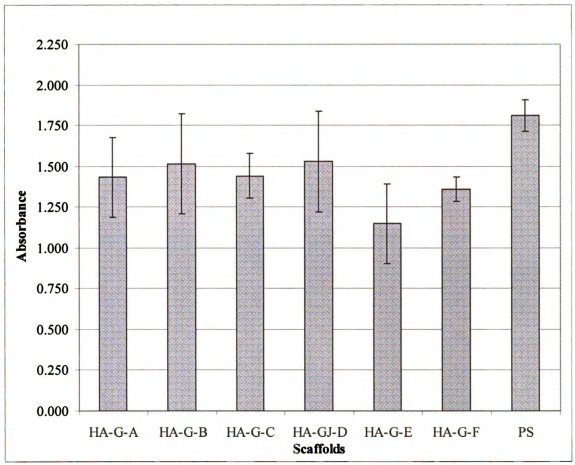

Figure 35: This bar graph represents the quantified AP activity after 14 days culture of MC3T3-E1 on dS HA scaffolds and PS substrates. TCA was used to dissolve the AP salt and the absorbance was measured with a spectrophotometer at 540 nm. Three trials of n=3 were conducted at different times using different passages of OB cells. The Y-error bars were determined from the standard error of the mean. ANOVA one-way analysis with a Tukey post-hoc test determined there was no statistically significant difference between the dS scaffolds and PS substrate ($p > 0.05$).

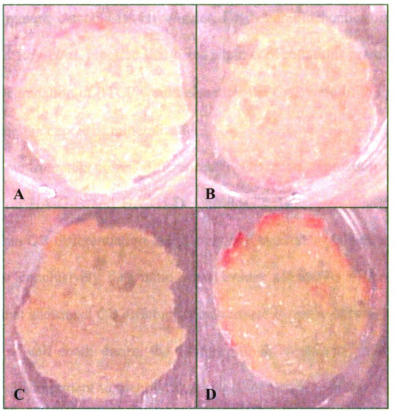

Figure 36: Digital images depict the stained AP activity (30 minute reaction time) on the pf57 HA scaffolds, HA-GJ-D (A & B) and HA-G-B (C & D), after 14 days culture of MC3T3-E1. Three trials of n=3 were conducted at different times using different passages of OB cells and no AP was observed on the scaffolds not shown. The HA scaffolds are 13 mm in diameter.

Past research has shown OBs to prefer porous scaffolds with a greater surface area, and surface roughness.[26, 144] HA has been shown to enhance differentiation as compared to PS substrates.[8] Thus, one possibility could be the OBs on the pf57 scaffolds differentiated at a faster rate and thus the production of the AP activity peaked before the targeted 14 days. FTIR scans of the pf57 scaffold suggest βTCP is present within the pf57 scaffolds. βTCP has a much greater solubility rate than HA.[21, 123] Degradation of the

βTCP would alter the calcium and phosphate concentrations within the medium, which could affect AP activity production and/or OB differentiation. Osteocalcin, a protein found only in mature osteoblasts, is considered a better biochemical marker for OB differentiation.[37] Roy *et al.* reported that osteocalcin concentrations are correlated to the Ca/P ratio.[145] Degradation of βTCP would also alter the Ca/P ratio of the pf57 scaffolds, possibly affecting the degree of mineralization.

Within our research group, differences in OB gene expression were observed when cultured on HA-G-B and HA-GJ-D scaffolds.[146] Thus, one might expect to see differences within OB differentiation. AP is only one marker for OB differentiation. For future work, to conclusively determine what factors affect OB differentiation, it is recommended that additional OB differentiation markers be used. Although there were no physical signs of cell death during the 14 day OB differentiation study on the pf57 scaffolds, it is still important to mention that cell death is a possibility for the slight AP signal. High concentrations of calcium and phosphate ions present within the medium as a result of a degrading CaP phase can also have negative, toxic and possibly terminal effects on the cells. This experiment cultured OB cells under static conditions feeding with fresh media daily. However, under these conditions, there are limitations in the ability of the nutrients to penetrate into the porous network.[147] One favourable alternative to culturing under static conditions is to culture using a flow perfusion bioreactor.[148] In addition to improving the delivery of nutrients throughout the scaffold, metabolically active cells like OBs are stimulated by the mechanical signals that are generated by the shear stress of the flowing fluid.[149, 150] Furthermore, OBs cultured in bioreactors have showed enhanced AP activity and mineralization.[151, 152]

βTCP has favourable properties for bone applications including, biocompatible and osteoconductive. However, βTCP degrades at a much faster rate as compared to HA.[89, 123] This is advantageous for applications that require a high resorption rate, but bone tissue regeneration is a slow process and *in vivo* βTCP implants have been shown to resorb before sufficient bone formation.[153] The resorption rate of HA is much slower than that of βTCP and thus HA implants offer greater mechanical stability. Biphasic calcium phosphates (BCP) are a ratio of HA and βTCP, and thus have the favourable properties of a greater resorption rate with greater mechanical stability. In a study by Wang *at el.*, BCP ceramics implanted into periodontal defects of monkeys demonstrated rapid bone replacement.[154] However, in a study by Alam et al., BCP ceramics with a minimum of 25% βTCP resulted in a fibrous connective tissue formation, where as the 100% HA demonstrated normal bone formation, when implanted into Wistar rats.[155] The lack of bone formation in the BCP ceramics could be the result chronic inflammation observed. A previous study by Malard *et al.*, noted strong inflammatory responses in 10-20 μm powders as a result of a high resorption rate.[156] Similar inflammatory responses have been seen in other highly resorbable materials, like polylactic acid (PLA) and polyglycolic acid (PGA).[157, 158] Although the HA/βTCP ratio was not quantified in this study, the intensity of the βTCP peak at 29.6° 2-θ in comparison to the intensity of HA peak at 31.8° 2-θ suggests only a small amount of βTCP is present.

Cell proliferation was studied on both the dS and pf57 scaffolds fabricated from HA-G-B and HA-GJ-D powders. The OB proliferation was quantified by a hemacytometer count for the dS scaffolds (Figure 37). The results for both the HA-G-B and HA-GJ-D scaffolds are consistent with previous findings, suggesting HA suppresses

OB proliferation as compared to PS substrates.[26] However, no difference was observed in the OB proliferation on the HA-G-B and HA-GJ-D scaffolds. Immunofluorescent actin stain was used to qualify the OB proliferation on both the dS and pf57 scaffolds. Figure 39 and Figure 40 depict the OB proliferation over 72 hours for the dS HA-G-B and HA-GJ-D scaffolds, respectively. Figure 41 and Figure 42 show the OB proliferation over 72 hours for the pf57 HA-G-B and HA-GJ-D scaffolds, respectively. The complexity of the porous scaffold makes accurately quantifying OB proliferation on the porous scaffolds nearly impossible. The images from the immunofluorescent stain clearly show a significant increase in the actin over the 72 hours. These results are in agreement with published findings that OBs have high affinity to porous scaffolds.[18, 144]

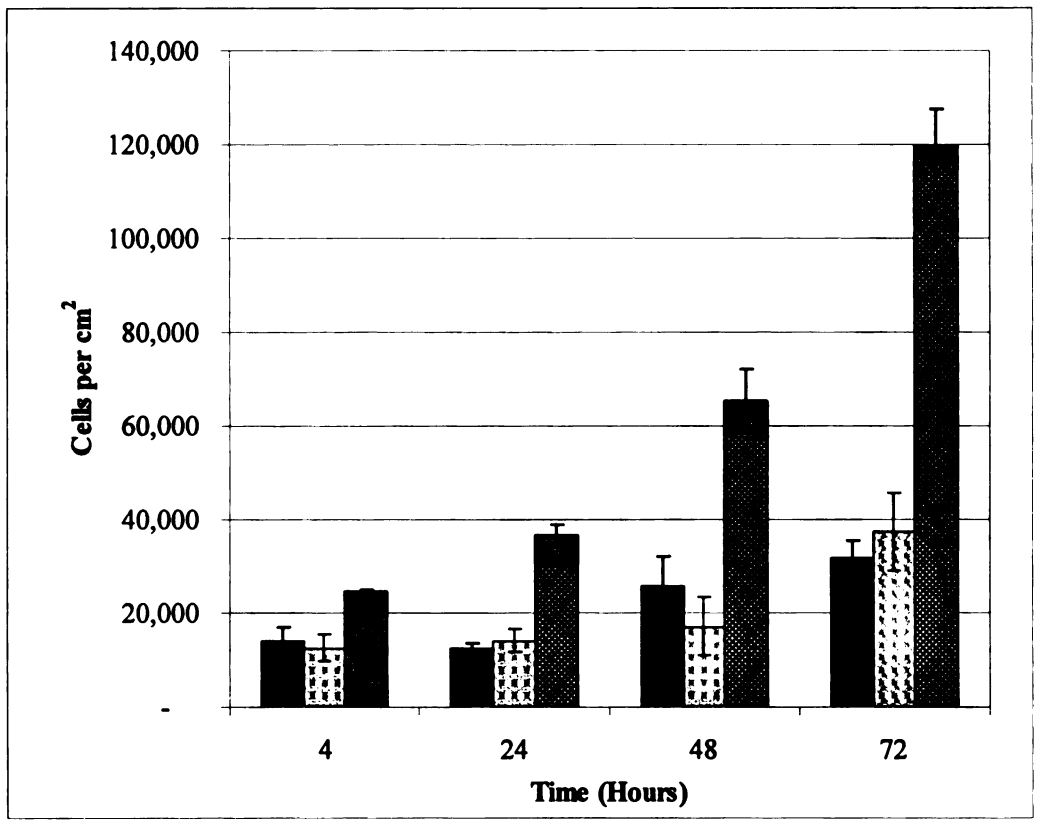

Figure 37: Hemacytometer results quantifying OB proliferation over a 72 hours on dS HA-G-B (Black) and HA-GJ-D (plaid) scaffolds and PS (Dark crossed) substrate. The proliferation results are consistent with published findings that proliferation of OBs is suppressed when cultured on dense HA scaffolds.[26] Three trials of n=3 were conducted at different times using different passages of OB cells. The Y-error bars were determined from the standard error of the mean.

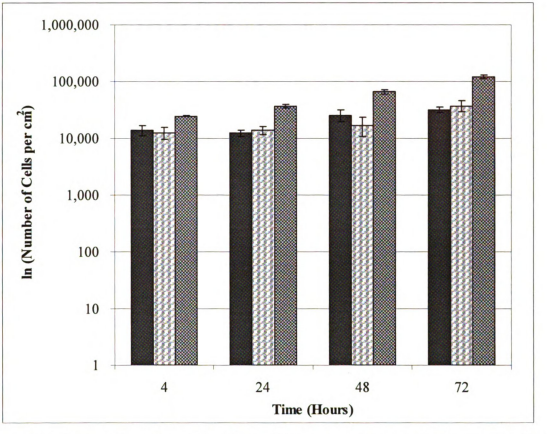

Figure 38: The semi-log plot of the OB proliferation on ds HA-B-G (Black), HA-D-GJ (Plaid) and PS (Dark crossed) scaffolds depicts proliferation over 72 hours. The PS demonstrates more consistent proliferation, where the OB proliferation on the dS scaffolds increases after 48 hours. Three trials of n=3 were conducted at different times using different passages of OB cells. The Y-error bars were determined from the standard error of the mean.

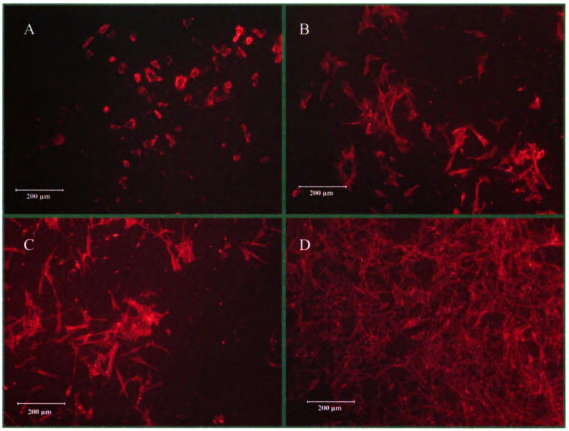

Figure 39: Immunofluorescent OB actin stained at 4, 24, 28 and 72 hours (A, B, C and D, respectively) on dS HA-G-B scaffolds. OB proliferation is observed over the 72 hours. Imaged at 100X magnification. The above images are representative images of the scaffolds. Five images were collected for each scaffold and three trials of n = 3 scaffolds were conducted at different times using different passages of OB cells. Scale bars represent 200 µm.

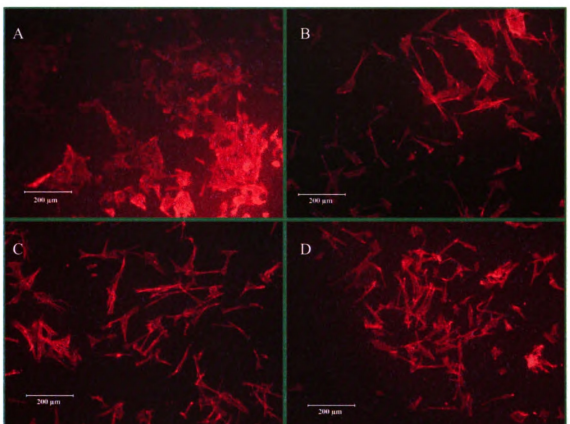

Figure 40: Immunofluorescent OB actin stained at 4, 24, 28 and 72 hours (A, B, C and D, respectively) on dS HA-GJ-D scaffolds. OB proliferation is observed over the 72 hours. Imaged at 100X magnification. The above images are representative images of the scaffolds. Five images were collected for each scaffold and three trials of n = 3 scaffolds were conducted at different times using different passages of OB cells. Scale bars represent 200 µm.

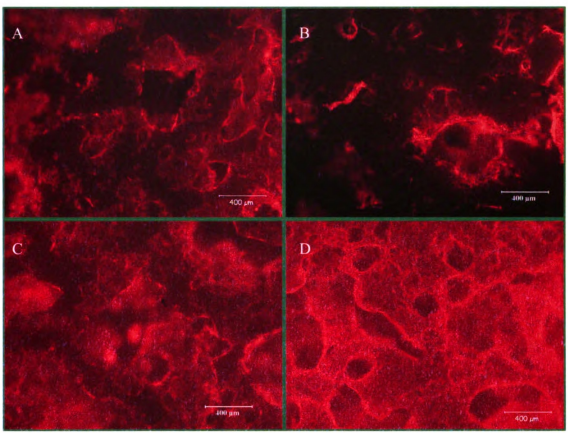

Figure 41: Immunofluorescent OB actin stained at 4, 24, 28 and 72 hours (A, B, C and D, respectively) on pf57-GJ HA scaffolds. A significant increase OBs is observed over the over the 72 hours. At 72 hours the OBs nearly cover the scaffolds as compared to 4 (A) and 24 (B) hours. The immunofluoresced actin is shown to be brighter along the pore edges which would suggest a higher concentration of cells. Imaged at 50X magnification. The above images are representative images of the scaffolds. Five images were collected for each scaffold and three trials of n = 3 scaffolds were conducted at different times using different passages of OB cells. Scale bars represent 400 µm.

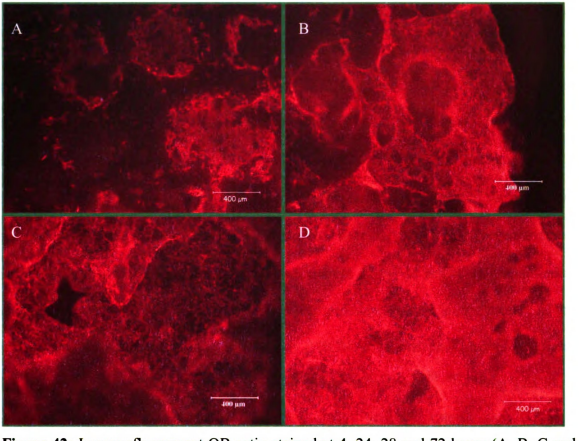

Figure 42: Immunofluorescent OB actin stained at 4, 24, 28 and 72 hours (A, B, C and D, respectively) on pf57-G HA scaffolds. A significant increase OBs is observed over the over the 72 hours. At 72 hours the OBs nearly cover the scaffolds as compared to 4 (A) and 24 (B) hours. The immunofluoresced actin is shown to be brighter along the pore edges which would suggest a higher concentration of cells. The OB proliferation on the pf57-G and pf57-GJ scaffolds at 72 hours, as observed by the immunofluorescent staining, are comparable in promoting OB proliferation. Imaged at 50X magnification. The above images are representative images of the scaffolds. Five images were collected for each scaffold and three trials of n = 3 scaffolds were conducted at different times using different passages of OB cells. Scale bars represent 400 µm.

4.4 Conclusions and Future Recommendations

The XRD and FTIR scans indicate the presence of a second CaP phase for the sintered pf57 HA scaffolds. The feather-like structure, observed by SEM imaging, along the grain boundaries of the pf57 HA scaffolds confirms the presence of this second CaP phase. XRD and FTIR analysis, as well as the characteristic feather-like structure of this nucleated phase, identify this second phase as βTCP. Biphasic (BCP) scaffolds are often challenging to fabricate due to the segregation of HA and βTCP powders. This work identified that porous, binderless BCP scaffolds can be fabricated by nucleating βTCP during sintering of the pf57 scaffolds. However, there are many potential variables that can affect βTCP nucleation. Thus, future studies are necessary to identify these variables. Some of these variables include the moisture content of the pf scaffolds, the sintering temperature variations, the sintering partial water pressure, and the pore structure of the scaffolds. Laser scanning confocal microscopy (LSCM) is an emerging technology useful for analysing pore structure, shape and surface microstructure.[159, 160] Using LSCM, a series of images can be taken of the porous scaffold. With the LSCM, each image is captured within the same plane or foci.[160] These confocal images are assembled at different planes by overlaying images at different depths.[160] Recommended future studies would utilize this tool to more accurately determine micro- and macropore sizes of the 3-dimensional pf scaffolds.[160]

In addition, future studies are necessary to characterize the properties this new biphasic (HA:βTCP) scaffold. Mechanical strength and resorption are two important properties that are dependent on the HA:βTCP ratio. A simple XRD study is recommended, to focus on the 2θ region where βTCP and key HA peaks (28 – 34°, 2θ)

exist. To provide more detailed information of this region, a slower incremental step size is recommended (0.01). From this scan, the peak-to-peak height ratios can be used to calculate the HA:βTCP ratio for the biphasic scaffolds.

An increase in the observed immunofluoresced actin filament was observed on both the dS and pf scaffolds over 72 hours by immunofluorescent imaging and an increase proliferation was observed by cell number on the dS surfaces. Both approaches demonstrated decreased proliferation on dense HA as compared to the polystyrene (PS) control, which is consistent with findings that suggest HA suppresses OB proliferation.[26] This work concludes that the air-jet sieved HA has no significant effect on the proliferation and differentiation of OBs seeded on dS scaffolds, and no significant effect on the proliferation of OBs seeded on pf57 scaffolds. The OB proliferation, as observed over 72 hours on the pf57 scaffolds, confirms that binderless, porous foamed scaffolds are a suitable environment for OB proliferation.

However, after an extended culture time of 14 days, a low AP activity was observed on the pf57 scaffolds. The AP activity was used as a marker for OB differentiation and was studied at only one time point. The AP enzyme production curve was modelled after the dS scaffolds. Therefore, the lack of AP activity on the pf57 scaffolds at 14 days could be the result of the peak AP enzyme production occurring either prior to or post the 14 day time point. One recommended future study is to develop the AP enzyme production curve for the pf57 scaffolds, investigating various time points (4, 6, 9, 12, 14 days). An additional study is recommended to investigate the AP activity on the 3-dimensional pf57 scaffolds using a perfusion flow bioreactor. A perfusion flow bioreactor provides continuous dynamic flow of media or nutrients to the OBs cultured

on the 3-dimensional pf57 scaffolds. This continuous flow not only supplies cells within the inner pores of the 3-D scaffold with nutrients, but also flushes away toxic cell bi-products that could potentially lead to cell death, unlike static culture conditions. The use of a perfusion flow bioreactor is also a better model of the body, where fluids are constantly recirculating.

Overall, this work demonstrated BCP porous scaffolds can be fabricated using a binderless method starting from HA powder. This preliminary work also suggests the pf biphasic scaffolds are a suitable scaffold for 72 hour OB proliferation.

APPENDIX A

TISSUE CULTURE

CELL CULTURE

Tissue Culture Media

Stock Minimum Essential Medium (α-MEM Media)

Procedure:

1. Autoclave 20 – 25 media bottles and allow the bottles to completely dry.
2. Add 2 gallons (7.56 Liters) of distilled H_2O to the 20-L medium jug.
3. Add the α-MEM media powder into the medium jug. (Turns the liquid a orange-ish, yellow and smells like dog food)
4. Add the remaining additional 2.44L of distilled H_20, saving some to rinse out the powdered media container.
   Note: 2.44L is equivalent to about an inch above the sticker on the milk jug container or where the bottom part of the handle on the jug is first attached.
5. Stir the media until the powder is completely dissolved.
6. Weigh out 22grams of $NaHCO_3$ and add it to the mixture. (This turns the mixture red)
7. Stir mixture until it is completely dissolved.
8. Check the pH, it should be close to a pH of 7.(Most of the time, it is accurate without adjusting)

Sterilizing the Media:

1. Filter-sterilize the media with a 0.22μm bottle filter, into an empty media bottle.
   Note: Filter sterilize the media in the bio-safety cabinet. Morethan one filter may be needed to sterilize all the media.
2. Label the sterilized media as follows; α-MEM, the date and your initials.
3. Store the sterilized media at 4°C.
4. Wash the media bottle and prepare it for autoclave sterilization.

Complete Media

Used to feed stock cells

- Add 55.5ml of FBS to 500 ml of α-MEM

Differential Media

Used to feed confluent cells for a long-term study

1. Add 55.5mL of FBS to 500mL of α-MEM. (Complete Media)
2. Add 1.11mL of β- Glycerol Phosphate to the Complete Media. (Differentiation Media)
   Note: This portion of differential media will last at 4 ℃, over the course of a long-term study.
3. Just prior to use, add 125uL of ascorbic acid to 50mL of differential media.

Differentiation media with ascorbic acid must be made fresh.

β-Glycerol Phosphate

A supplement for differential media

1. Weight out 21.6 grams of β-glycerol phosphate.
2. Dissolve the β-glycerol phosphate into 100mL distilled H_2O.
3. Filter sterilize, and aliquot the liquid into 15mL conical tubes.
4. Store at –20°C.

Ascorbic Acid (Vitamin C)

A supplement for differential media

1. Weight out 0.05g of Ascorbic acid
2. Dissolve it in 5mL of 1xPBS
3. Filter sterilize

******MAKE FRESH DAILY: Ascorbic acid will break down within 4 hours.******

Freezing Media

Cells are frozen in this solution for long periods of time

- Add 5mL of DMSO to 45ml of Complete Media.
  (DMSO is stored above the centrifuge in tissue culture room)

Antibiotic Solutions

Media (complete or differentiation) is supplemented with antibiotic to treat contaminated cells or prevent contamination during a study

Antibiotics Stock Solutions

Penicillin-Streptomycin (pen/strep)

- Comes pre-prepared from the manufacturer
  Stock Concentration: 10,000 units/mL penicillin G sodium and 10,000µg/mL streptomycin sulfate

Ampicillin (Amp)

1. Add 1g of powder Ampicillin to 10mL distilled H_2O
2. Filter sterilize with a 0.22µm filter, aliquot into 1mL tubes
   Stock Concentration: 100mg/Ml

Ciprofloxacin HCl (Cipro)

1. Add 0.1g of powder Ciprofloxacin HCL to 10mL distilled H_2O
2. Filter sterilize with a 0.22µm filter, aliquot into 1mL tubes
   Stock Concentration: 10mg/mL

Antibiotic Solutions cont.

Working Solutions of Antibiotics

Penicillin-Streptomycin

- Add 5mL of pen/strep to 50mL of the desired media.

Ampicillin-Ciprofloxacin HCl (Used in combination with one another)

1. Add 500µL Amp stock solution to 500mL of the desired media
2. Add 500µL Cipro stock solution to 500mL of the desired media

Working concentrations:

Amp: 100µg/mL
Cipro: 10µg/mL

****Antibiotics will not protect against yeast infections.** **

Cells

Freezing / Thawing

** *Remember: Freeze Slow, Thaw Quick!* **

Freezing

When freezing, use one cryogenic vial for freezing every 1 million cells (rounding down)

1. Divide the enzymatically-detached cells into groups of 1 million, placing them into separate conical tubes.
2. Spin down the cells to pellet the cells from the trypsin / media mixture (Program 2: 3000rpm for 10 minutes).
3. Aspirate off the trypsin / media mixture, leaving the cell pellet.
4. Resuspend the cells in 1.5mL of freezing media.
5. Transfer the cells to a cryogenic vial, labeled with the cell type, clone number, passage number, date, initials, and antibiotic treatment (if necessary).

Thawing

1. Select the cryogenic vial of frozen cells from the -80°C freezer or the liquid nitrogen storage unit.
2. Thaw the cells quickly in warm, sterile water. (37°C)
3. Once thawed, transfer the contents from the cryogenic vial into a tissue culture dish. (One cryogenic vial = One tissue culture dish)
4. Add 1mL of FBS to the cells in each tissue culture dish.
5. Incubate (37°C, 95% air / 5% CO_2) for 5 minutes.
6. Add 10mL of fresh complete media to each dish.

Thawing cont.

7. Swirl the tissue culture dish slowly, moving front to back and side to side to center the cells on the plate.
8. Label the dish with the clone number, passage number, date and your initials.
9. Incubate for 24hours to allow the cell to reattach before splitting the culture.
10. If the cell numbers look low, add 5mL of fresh complete media and incubated for another 24 hours.

Cells

Culture Splitting

Healthy Mc3T3-E1 cells are split every 2 – 3 days for a 100mm dish (4 – 5 days for a 170mm flask), and there should be ~ 25 cells or more per field under the microscope (at 10x magnification) Cell typically double in 24 hours. If cells are growing excessively fast (need to be split every day for 100mm dish), or excessively slow (1 – 2 times a week for a 100mm dish) there is a good probability the cells have been sub-cloned. Do not use these cells for a study.

Warm the media and trypsin EDTA to room temperature before use.

1. Aspirate out the old media from the culture dish.
2. Rinse the dish with 1 – 2 mL of 1xPBS.
3. Aspirate out the PBS wash.
4. Add 1mL Trypsin-EDTA for 100mm tissue culture plate, (2mL for culture flask).
5. Immediately add 1mL of complete media to the culture dish (to prevent over-trypsinization of the cells).
6. Swirl the cells front to back and side to side to coat the entire plate with the trypsin / media mixture, and to force the cells to detach from the plate.
   Note: Trypsin is an enzyme that will detach the spinacles from the cell forcing the cell to detach from the plate. This process can be detrimental to the cells if left for long periods of time soaking in the trypsin.
7. Verify under the microscope the cells have detached from the culture plate.
8. Transfer the cells to a conical tube.
9. Count the cells using a hemacytometer, by loading both sides of the hemacytometer with 10μL of cells.

Cells
Culture Plating
Cells can be plated in culture dishes or flasks. Flasks are useful for culture a large number of cells without changing the passage number. Be careful not to allow the cells to become confluent. Confluent cells should not be use for any studies.

1. Cells are plated to a density of 60,000 – 75,000 cells to each new 100mm culture dish. (125,000 – 140,000 for culture flask)
2. Add 10mL of complete media to each dish. (25mL to each culture flask)
3. Label the dish with the number of cells, date, initials, clone number, and new passage number.
4. Incubate cells.

Cells
Feeding

Stock Plates

1. Stock plates are fed every time cells are split, with complete media.
2. On occasion, if cells are not growing at their normal rate, increasing the FBS concentration will help boost cell growth.
3. Cells should not be split unless they are ready, thus there may be occasions where the cells are fed without being split.
4. If there is a bacterial contaminate, antibiotic treatments can be used.
5. When under antibiotic treatment, FEED DAILY for only 12-14 days. Improper use of antibiotics can develop antibiotic resistant bacteria.

*****IMPORTANT: Before cells are treated with antibiotics, contact Regina Irwin in Dr. McCabe's Lab at 5-6475 x1383. She will help identify 1) what bacteria is present, 2) the best course of antibiotics needed. *****

Proliferation Studies

1. Cells for proliferation studies are fed with complete media every 1 – 2 days depending on the experimental design.
2. Antibiotics can be used to prevent bacterial contamination, but they will not protect from yeast infections.

Differentiation Studies

1. Cells for differentiation studies are fed with complete media until the cells become confluent (day 4 – day 6).
2. Once confluent (day 4 – day 6), cells are fed daily with differentiation media for the duration of the experiment.
3. Antibiotics can be used to prevent bacterial contamination, but they will not protect from yeast infections.

PROTOCOLS

ACTIN IMMUNOFLUORESCENT STAINING

This protocol uses an immunofluorescent phallotoxin to stain the cellular actin present in the cytoskeleton. Actin is a myofibril protein found in cells. This protocol can be used to stain cells to study cell shape and phenotype, and qualitatively study cellular proliferation and growth. This stain is run at 4, 8, 24, 48, 72 hours with n=3 and cells are feed every other day. Actin is stained red.

Procedure:

1. Wash cells with 1X PBS two times (2x).
2. Fix cells in 3.7% formaldehyde for 10 min at room temperature (RT)[1]
3. Wash with 1X PBS two times (2x)
4. Permealize for 5min with 0.1% Triton X-100 in 1X PBS.
5. Wash with 1X PBS two times (2x)
6. Pre-incubate slides for 30 min with 1% Bovine Serum Albumin in 1X PBS.

THE FOLLOWING STEPS ARE DONE IN THE DARK

7. Fluorescent stain slides for 20 min at RT with phallotoxin, Rhodamine - Phalloidin (kept in freezer), dilute 5µl methanolic stock[2] in 200µl of 1% BSA in 1X PBS, for each slide. (The addition of 1% BSA helps reduce nonspecific background staining.) Keep wells in a dark covered incubator so as to prevent drying. **"LIGHT SENSITIVE"**
8. Wash with 1X PBS two times (2x).
9. See other immunofluorescent staining protocols if further staining is required. If not continue to step 11.
10. Mount in a 1:1 solution of PBS to glycerol or IMMUNOMOUT and seal edges- can last 2-3 days when stored at 4°C. For long-term storage, air-dry the cells and mount with acrylic-based resin (Cytoseal™). When finished, wrap actin stained plates in Aluminum foil and store at 4°C it will last up to 6 months.

---

[1] Methanol can disrupt actin during fixation process. Be sure to use methanol-free formaldehyde.

[2] Preparation of stock solution – Contents of vial are dissolved in 1.5mL methanol. This is referred to as methanolic stock, and yields a final concentration of 200 units/mL, approximately equivalent to 6.6µM.

AGAROSE GEL

Agarose gel is commonly placed around dense discs used for cellular experiments to prevent cells from growing on the polystyrene culture well.

Procedure:
Makes 300mL of sterile Agarose Gel

1. Weigh out 3g of Agarose (Invitrogen #15510-027).
2. Add to an autoclaved media bottle
3. Add 300ml of distilled H_2O, making sure to label the bottle.
4. Microwave in 3-minute increments, until the solution is dissolved.
   Note: The bottles will be hot and boiling.
5. Autoclave the solution (program 10, liquids) to sterilize.

ALKALINE PHOSPHATASE STAIN

Alkaline phosphatase (AP) is an enzyme that is produced by differentiating osteoblasts in preparation for and during the early stages of mineral deposition. AP is a marker osteoblast differentiation. This protocol stains the AP activity red and most commonly used on long-term cultured ranging form 7 to 21 days.

Fixing Cells

1. Aspirate off media
2. Rinse culture wells with 1X PBS (with pH 7.4)
3. Fix for 10 min with 2% Paraformaldehyde (stored in 4°C)
4. Rinse with 0.1 M cacodylic buffer (with pH 7.4)
5. Add 0.1 M cacodylic buffer to fill the well half way, store plate in 4°C until your ready to stain.

Staining Cells

1. Pre-weigh everything, no time to stop.
2. Add together the pre-weighed chemicals in the following order: (See Table 1)
   - Distilled H_2O
   - Tris maleate buffer
   - N,N dimethylformamide
   - Naphthol AS-MX
   - Fast Red
3. Using a glass funnel and circular filter paper of 125mm, filter the solution. If yellow in appearance, reaction already occurring - **Do Not Use.**
4. Add enough AP stain to cover the bottom of the staining dish.
5. Put culture dish under 37°C conditions for ½ hour, or until you see red color. If you see yellow remove stain promptly.
6. Remove stain buffer and rinse with 1X cacodylic buffer.
7. For future Von Kossa staining, add 0.1 M cacodylic buffer to fill the well half way, then leave plate in 4°C until ready to stain.

ALKALINE PHOSPHATASE STAIN CONT

Alkaline Phosphatase Stain	**25mL**	**50mL**	**100mL**	**200mL**
Naphthol As-mx Phosphate disodium salt	12.5mg	25mg	50mg	100mg
N,N dimethylformamide	0.7mL	1.4mL	2.8mL	5.6mL
Distilled H_2O	11.8mL	23.6mL	47.2mL	94.4mL
Tris maleate buffer - 0.2M alkaline pH 8.4	12.5mL	25mL	50mL	100mL
Fast Red Salt	25mg	50mg	100mg	200mg

Table 2: Ingredient ratios for differing quantities of staining solution

ALKALINE PHOSPHATASE QUANTIFICATION

This protocol is designed to quantify the alkaline phosphatase (AP) enzyme present after culture for a given time, typically ranging from 7-21 days. In this protocol, concentrated trichloroacetic acid is used to solubilize the red precipitated salt present after AP staining. **Note: Only use this protocol AFTER cells have been fixed and stained for AP, and you have taken ALL necessary pictures of your specimens.**

Procedure:

1. Aspirate off the cacodylic buffer.
2. For the dense HA or plastic substrates, carefully detach each individual, red stained, cellular matrix from the scaffold substrates, by gently scraping with a cell scraper or spatula.
   ***Note*: Do your best to remove all of cellular matrix.**
3. Transfer each cellular matrix to an individual well of a 6-well culture dish and label appropriately.
4. Add 1mL of 100% TCA to each well.
5. Mildly agitate on the rocker shaker plate, speed 7 at room temperature for 24 hours, or until the red precipitated salt is completely dissolved out of the organic matrix. (The remaining matrix will look like a clear or slightly tinted gel.)
6. Use the spectrophotometer to measure the absorbance of the each well at a wavelength of 540nm, using 100%TCA as the zeroing reference solution.
7. Dilute the solubilized stain by adding 1mL of 100% TCA to 0.5mL of solubilized stain in a cuvette. Mix thoroughly.

***This protocol is best suited for dense hydroxyapatite discs*.**

Note: If the absorbance reading is too high (>3), further dilute the solubilized AP stain in 100% TCA

Calculations:

1. Normalize the collected data to the surface area.

$$\frac{Absorption\ (A)}{SurfaceArea\ (SA)} \qquad 5$$

2. Find the mean all the normalized readings for plastic and HA

$$\frac{mean\ HA}{mean\ Plastic} \equiv fold\ increase\ or\ decrease\ of\ AP \qquad 6$$

3. Determine the fold increase or decrease.

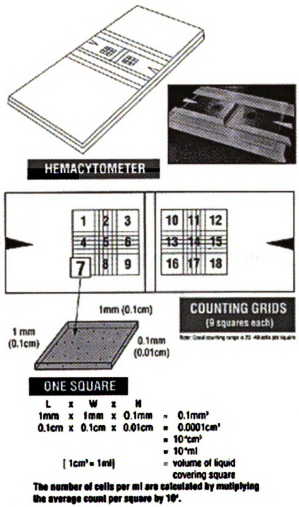

Procedure

1. **Load** both sides of the hemacytometer with the cell suspension - covering both counting grids.
2. **Count** the number of cells in squares 1, 3, 5, 7 and 9 (Figure). This is side A.
3. **Count** the number of cells in squares 10, 12, 14, 16 and 18 (Figure). This is side B.
4. **Add** A and B, and divide by 2, to obtain the average of both sides.
5. **Multiply** the average of both sides by 2000. This gives the number of cells per mL.
6. **Determine** the total number of cells available for sub-culturing, by multiplying the number of cells per mL by the total number of mLs of cell suspension.

Figure 43: Hemacytometer Schematic ***(http://invitrogen.com)***

$$\frac{Total\ \#\ of\ cells}{Total\ mL} = \frac{65{,}000\ cells}{(x)\,mL} \qquad 7$$

1. Carefully aspirate off the culture media from the wells.
2. Wash plate gently with 1X PBS warmed to room temperature:

Number of Culture Wells	Volume of 1X PBS Rinse
96	0.2 mL
48	0.5 mL
24	1.0 mL
12	2.0 mL
6	3.0 mL

Table 3: Quantity of 1X PBS rinse needed for various sized culture plates.

3. Carefully aspirate off the PBS rinse and add crystal violet solution (as listed in Table 4)

Number of Culture Wells	Volume of Crystal Violet
96	50 µL
48	100 µL
24	200 µL
12	500 µL
6	750 µL

Table 4: Quantity of Crystal Violet staining solution needed for various sized culture plates.

4. Incubate 10 minutes at room temperature.
5. Wash the plate twice by immersing the plate in a large flat tub of tap water. Change the tap water between washes. Be careful not to lift the cells off the plate.
   Note: Wash the plate until all the excess Crystal violet stain has been removed.
6. Drain the plate upside down on paper towels. Or aspirate off the excess moisture from stain scaffolds.
7. Add 1% Sodium Dodecylsulfate (SDS) to solubilize the stain.

Number of Culture Wells	Volume of 1% SDS
96	100 µL
48	300 µL
24	600 µL
12	1.0 mL
6	1.5 mL

Table 5: Quantity of 1% SDS solution needed for the various sized culture plates.

8. Agitate plate on orbital shaker until color is uniform and there are no areas of dense coloration in bottom of wells.

9. Read absorbance of each well at 570 nm using a spectrophotometer.

Procedure

1. Rinse the scaffolds in 1X PBS
2. Add 1 – 3 mL of 0.1% Trypsin EDTA and incubated for 3 minutes.
3. Collect the cells in a conical tube.
4. Rinse the scaffold with 1 mL of 0.1% Trypsin EDTA and collect rinse in the same conical tube.
5. Spin the tube at 3000 rpm for 5 minutes.
6. Carefully aspirate off the trypsin from the cell pellet
7. Place the samples on ice
8. Resuspend the cells in 2 mL 1X PBS
9. Sonicate for 20 seconds per cycle
   - Settings: 80% duty cycle, power output = 4, timer = on hold
10. Clean the probe tip with DI H_2O between samples, and before an after used with ethanol and DI H_2O.
11. Add 170 µL of sample to a 96-well opaque microplate.
12. Add 30 µL of 4.8 µg/mL Hoechst dye solution in Ethanol, prepared from stock concentrations of 200 µg/mL in H2O.
13. Measure the fluorescence using a fluorescent reader at a wavelength of 355/ 460.

Hoechst #33258 bis-Benzimide – Molecular Probes Inc, #H3569

Black Opaque Microfluor Plates – VWR #62402-983

HOECHST IMMUNOFLUORESCENT STAINING

Hoechst is an immunofluorescent DNA nucleus stain. This stain can be use in conjunction with other immunofluorescing stains such as Actin staining, however Hoechst nucleus staining is the final stain performed.

Preparation of Stain
*Note: This stain is stored under **dark** conditions at **room temperature.**.*

- Dissolve 0.0006g of Hoechst (Molecular Probes #-6506) in 10mL of ddH_2O. Makes a 10 µM staining solution.

Fixing
Note: Cells are fixed following the Actin stain protocol (for specific details refer back to that protocol), and in most cases they will have already been fixed.

1. Wash cells with 1X PBS two times (2x).
2. Fix cells in 3.7% formaldehyde for 10 min at room temperature.
3. Wash with 1X PBS two times (2x).
4. Permealized for 3 to 5 min with 0.1% Triton X-100 in 1X PBS.
5. Wash with 1X PBS two times.

Hoechst Nucleus Staining
Note: Be sure all other immunofluorescent stains are performed first.

1. Add approximately 200 µl of Hoechst stain to well / scaffold (Enough to cover)
2. Incubate in under dark conditions for 30 min. (10min recommended)
3. Aspirate off the stain
4. Wash with 1X PBS two times
5. Mount in a 1:1 solution of PBS to glycerol (#2136-01, TJ Baker) or IMMUNOMOUNT and seal edges – can last 2-3 days when stored at 4° C. (For long-term storage, air dry the cells and mount with acrylic-based resin (Cytoseal ™) – can last up to 6 months when stored at 4° C.)

TRYPAN BLUE VIABILITY STAINING

Trypan Blue is a vital dye used to stain cells that are dead or dying, for cell viability counting. Trypan blue reacts with negatively charged chromopores, only present when the cell membrane is damaged.
Reference: Freshney, R. (1987) Culture of Animal Cells: A Manual of Basic Technique, p. 117, Alan R. Liss, Inc., New York.

Procedure

1. Place 0.5 ml of a suitable cell suspension (dilute cells in complete medium without serum to an approximate concentration of 1×10^5 to 2×10^5 cells per ml) in a screw cap test tube.

2. Add 0.1 ml of 0.4% Trypan Blue Stain. Mix thoroughly.

3. Allow cells to stand for 5 min at 15 to 30°C (room temperature).

4. Fill a hemocytometer as for cell counting.

5. Under a microscope, observe if non-viable are stained and viable cells excluded the stain.

Von Kossa stains the minerals deposited by osteoblast bone cells after approximately 14-21 days. Stain is often performed after an AP stain.

Preparation of Von Kossa Stain

Dissolve 3gm of Silver Nitrate (Sigma #S-6506) in 100mL of ddH_2O. This solution can be stored wrapped in a brown bottle, filtered and reused. Change when solution becomes gray and cloudy with black precipitate.

Fixing

Wells are most often fixed for AP according to fixing procedure below.

1. Aspirate off media
2. Rinse culture wells with 1X PBS (with pH 7.4)
3. Fix for 10 min with 2% Paraformaldehyde (stored in 4°C)
4. Rinse with 0.1 M cacodylic buffer (with pH 7.4)
5. Add 0.1 M cacodylic buffer to fill the well half way, leave plates in 4C until ready to stain.

3% Von Kossa

Note: Do not rinse wells to be stained for VK with H_2O.

1. Rinse with 0.1 M cacodylic buffer.
2. Stain one well previously stained for AP and one unstained well.
3. Filter VK stain before each use.
4. Place plates in the sun or under a lamp for 15 minutes, or until you can see black mineral, (if negative, you will see a black ring at the liquid level). <Put plate under UV light in cabinet; keep watching periodically, 1 minute to 15 minutes>.
5. Aspirate off solution, put back in bottle.
6. Rinse many times in ddH_2O, until it is no longer cloudy.

PROTOCOL SOLUTIONS

Actin/Hoechst Detection

3.7% Formaldehyde
Cell fixative

- Add 10mL of 37% Formaldehyde to 90mL distilled H_20

Makes 100mL of 3.7% Formaldehyde

0.1% Triton
Surfactant used to wash away excess formaldehyde

- Add 0.1mL Triton to 99.9mL of 1xPBS

Makes 100mL 0.1% Triton

1.0% Bovine Serum, Albumin (BSA)
Protein used to enhance the fluorescing of Rhodamine/Phalloidin and Hoechst
***BSA is stored at 4°C, also store 1.0% solution at 4°C.*

- Add 0.4g BSA to 40mL of sterile 1xPBS

Hoechst #33342
Fluorescing dye that binds to DNA (Fluoresces the nuclei blue)
***Hoechst is stored at room temperature (≤25°C), protected from light.*

1. Add 0.003g Hoechst (powder) to 50mL distilled H_20
2. Use a sterile conical tube wrapped in aluminum foil to protect from light

Makes 50mL Hoechst dye

Rhodamine/Phalloidin
Fluorescing dye that binds to actin present in the cellular cytoskeleton (Fluoresces the actin red)
***Rhodamine/Phalloidin is stored in the freezer at ≤ -20°C.*
When preparing stock solution, dissolve in 1.5mL methanol.

1. Using 1mL tubes, prepare the following solution per sample being investigated
2. Add 5µL of methanolic stock of Rhodamine to 200µL of 1.0% BSA

Glycerol
Dye preservative, preserving the immunofluorescense for up to 3 days when stored under refrigerated conditions, protected from light

- Mix a 1:1 ratio of glycerol to distilled H_20

Alkaline Phosphatase Staining

Tris Acid Maleate Solution ***Store in 4℃****

1. Measure out 12.1g of Tris Base ((Tris hydrozomethyl-aminomathane}
2. Measure out 11.6 g of Maleic Acid
3. Add the dry chemicals 500mL of distilled H_2O.
4. Mix (under mild heat if necessary) until completely dissolved
5. Filter sterilize the solution using a 0.22μm filter

Makes 500mL of Tris Acid Maleate Solution

0.2M NaOH

pH adjustor

1. Weigh out 4g of NaOH.
2. Add the NaOH to 500mL dd H_2O.
3. Mix well until completely dissolved.

Makes 500mL 0.2M NaOH

Tris Maleate Buffer (pH 8.4) ***Store in 4℃****

1. Measure out 125mL Tris Acid Maleate Solution.
2. Add the Tris Acid Maleate Solution to 500 mL dd H_2O
3. Adjust the pH to 8.4 with 0.2M NaOH.
4. Filter sterilize the solution using a 0.22μm filter

Makes approximately 625mL of Tris buffer

Cacodylic Buffer (pH 7.4) ***Store in 4℃****

1. Measure out 8.0 g sodium cacodylic acid
2. Add sodium cacodylic acid to 500mL 1X PBS
3. Adjust the pH to 7.4 with 0.2M NaOH or 0.2M HCl
4. Filter sterilize the solution using a 0.22μm filter

Makes 500mL of Cacodylic buffer.

Alkaline Phosphatase Quantification

Trichloroacetic Acid (TCA)

** *TCA is a very nasty acid. Perform all powder constitution in the fume hood.* **

- Add 227 mL of distilled H_2O to 500g TCA.
- The solution will be clear, with a density of approximately 1.45g/ml.
- Store prepared TCA in an amber glass bottle at 4°C

Makes 227mL of *100% w/v TCA*

Crystal Violet Assay

0.2% Crystal Violet Stock Solution

Crystal violet is a nasty chemical. Measure out only in the fume hood and be sure to clean thoroughly. *

- Measure 98mL of dH2O into a sterilized, polyethylene bottle.
- Add 2mL of 190-proof ethanol to the dH_2O.
- Add 0.2g of Crystal Violet to the H_2O/Ethanol solution.
- Shake vigorously until dissolved.

Makes 100mL of 0.2% Crystal Violet Stock Solution.

10% SDS Stock Solution

SDS is a surfactant that solubilizes crystal violet

DO NOT AUTOCLAVE: (SDS will irreversibly precipitate)

- Measure out 50g of SDS.
- Add 400mL dH_2O to the SDS
- Heat solution to 68°C under constant stirring
- Cool solution to room temperature
- Adjust pH to 7.2 (with conjugate acid and base; HCL or NaOH)
- Adjust volume to 500mL with distilled water (dH_2O)
- Filter sterilize the solution using a 0.22μm filter

Makes 500mL of 10% SDS stock solution

20% SDS Stock Solution

SDS is a surfactant that solubilizes crystal violet

DO NOT AUTOCLAVE: (SDS will irreversibly precipitate)

- Measure out 100g of SDS.
- Add 400mL dH_2O to the SDS
- Heat solution to 68°C under constant stirring
- Cool solution to room temperature
- Adjust pH to 7.2 (with conjugate acid and base; HCL or NaOH)
- Adjust volume to 500mL with distilled water (dH_2O)
- Filter sterilize the solution using a 0.22μm filter

Makes 500mL of 10% SDS stock solution

DNA Quantification

Stock Solutions of Salmon Sperm DNA
Salmon Sperm DNA is used as the standard reference material for the DNA Proliferation Assay

1mg/mL Final Concentration

- Add 0.5mL of 10mg/mL to 4.5mL of sterile 1X PBS

Calculations:

$C_iV_i=C_fV_f$
10mg/mL (XmL) = 1mg/mL (5mL)
10mg/mL (XmL) = 5 mg
(10mg/mL (XmL)) / 10mg/mL) = (5 mg / 10mg/mL)
XmL = 5mg / 10mg/mL
XmL = 0.5mL

32μg/mL Final Concentration

- Add 32mL of 10mg/mL to 9.968mL of sterile 1X PBS

Calculations:

$C_iV_i=C_fV_f$
10mg/mL (XmL) = 32μL/mL (10mL)
10mg/mL (XmL) = 320μg =0.32mg
(10mg/mL (XmL)) / 10mg/mL) = (0.32 mg / 10mg/mL)
XmL = 0.32mg / 10mg/mL
XmL = 0.32mL =32μL

1μL/mL Final Concentration

1. Add 1μL of 10mg/mL to 9.999mL of sterile 1X PBS

Calculations:

$C_iV_i=C_fV_f$
10mg/mL (XmL) = 1μg/mL (10mL)
10mg/mL (XmL) = 10μg – 0.01mg
(10mg/mL (XmL)) / 10mg/mL) = (0.01mg / 10mg/mL)
XmL = 0.01mg / 10mg/mL
XmL = 0.001mL =1μL

Paraformaldehyde Solutions
Used as a cell fixative. Store at 4°C
Note: **Must be made in the fume hood**

2% Paraformaldehyde Solution

1. Dilute 2g of paraformaldehyde in 100 mL ddH_2O.

2. On hot plate, stir and heat (temperature at 65 °F).
   ****Monitor constantly****

3. Once dissolved, filter into individual bottles using Whatman-2 filter paper.

4% Paraformaldehyde Solution

1. Dilute 4g of paraformaldehyde in 100mL ddH_2O.

2. On hot plate, stir and heat (temperature at 65 °F).
   ****Monitor constantly****

3. Once dissolved, filter into individual bottles using Whatman-2 filter paper.

Phosphate Buffer Saline Solutions (PBS)

10X PBS

Stock concentration

NaCl	450.0g
Na_2HPO_4 $7H_2O$ (JT Baker)	39.7g
KH_2PO_4	7.2g

1. Measure out the appropriate amounts of each chemical, as listed above.
2. Add Reversed Osmosis (RO) H_2O until just below 5L mark, of the large PBS jug.
3. Measure the pH with the pH meter. The pH should be 6.6.
4. Make necessary pH adjustments with 1M HCl (to make more acidic) or 1M NaOH (to make more alkaline)
5. Add the remaining RO H_2O, to the 5L mark.

Makes 5L of 10x PBS

1X PBS

Used as a cell rinse during tissue culture and cell experiments

1. Dilute 10x PBS concentration following the formula listed below:
   10mL of 10XPBS + 90mL of (RO H_2O) = 100mL 1X PBS
2. Be sure to use an autoclavable bottle, and label it 1X PBS
3. If using a 1 Liter bottle, make about 500mL 1X PBS per bottle, or if using a 500mL bottle make about 300mL 1X PBS per bottle.
4. Sterilize by autoclaving (Program 10, Liquids)

Make as much as needed

Note: When sterilizing liquids, the bottles can only be half full.

Von Kossa Staining

Silver Nitrate Solution

1. Measure out 3g of Silver Nitrate
2. Dissolve the silver nitrate in 100mL dd H_2O.
3. Filter sterilize the solution using a 0.22μm filter
4. Store at room temperature, protected from light under desiccant conditions.

Makes 100mL of Silver Nitrate

Note: Recollect the Silver Nitrate for repeated use. To recycle for additional use, re-filter sterilize the solution using a 0.22 μm filter

APPENDIX B

LABORATORY PROCEDURES

ARCHIMEDES VOLUME DISPLACEMENT

The Archimedes volume displacement method is a technique used to measure scaffold porosity. This procedure is a modified version of the ASTM standard for measuring porosity of porous ceramics. The degree of porosity is calculated from the dry mass, suspended mass and the saturated mass. Although all the calculations are given below, data collected for measuring the porosity must be cataloged in the Excel Density Calculation Grid.

Preparation

1. Dry the samples in a shallow dish at 125C or higher for at least 1 hour in the Gravity Convection Oven (GCO) to dry off any excess moisture.
   Note: To ensure moisture is evaporation, be sure the plugs are removed from the side ventilation ports on the oven.
2. Clean and label a 50mL beaker for each scaffold being measured.
   Note: Be sure to keep the different foam batches separated.
3. Place the dried scaffolds into their respectively labeled beakers
4. Prepare a grid in your lab notebook for collecting the data, similar to what is seen below.

Date: _____ HA Foam #___	Dry Mass	Suspended Mass	Saturated Mass
Sample 1			
Sample 2			
Sample 3			

Table 6: Raw Data Density Table

Procedure

1. Tare the balance with a clean piece of weigh paper.
2. Place one of the scaffolds on the tarred balance and dry mass it.
3. Record the dry mass (in grams) in grid prepared in your lab book.
4. Collect the dry mass for each sample being measured.
   Note: You must TARE the balance between every sample.
5. Once the dry mass has been collected for each scaffold, fill the beakers with 40 – 50mL of distilled H_2O[1].
6. Place the beakers into the vacuum chamber.
7. Draw a vacuum on the chamber to 25 inHg for 5 -10 minutes.
8. Release the vacuum.

[1] Ethanol can be used in place of distilled water as the liquid medium.

9. Draw a vacuum to 26inHg. Hold for 30 minutes.

ARCHIMEDES VOLUME DISPLACEMENT (continued)

10. Release the vacuum.
11. Draw a vacuum to 27 inHg. The vacuum pump often plateaus between 26 and 27 inHg. Draw as high of a vacuum as possible. Hold for another 30 minutes.
12. Look through the window of the vacuum chamber and visually check to see if air bubbles are still coming off the scaffolds.
13. If bubbles are present, release the vacuum and repeat step 11. **Repeat step 12 until no more bubbles are coming off the scaffolds.**

Bubbles indicate there is still air trapped within the inner pores of the scaffolds. This will result in inaccurate density calculations.

14. Remove the beakers from the vacuum chamber
15. Set up the suspended mass apparatus as described below.
16. Tare the suspended mass apparatus on the balance.
17. Once tarred, place one scaffold in the center of the suspended basket, making sure the scaffold does not touch any of the basket sides.
18. Record this mass as the suspended mass (in grams) in your lab book.
19. Return the sample to the respective beaker of water.
20. Collect the suspended mass for each sample being measured, making sure the scaffold does not touch any of the basket sides.
    Note: You must TARE the balance between every sample.
21. Record the suspended masses (in grams) in your lab book.
22. Return each sample to its respective beaker of water immediately after recording the suspended mass.
23. Once the suspended mass has been collected for each scaffold, remove the suspended mass apparatus from the balance, and tare the balance with a clean piece of weigh paper.
24. Remove the first scaffold from the beaker of water, and gently roll the scaffold on a clean Kim wipe to remove the excess water on the surface of the sample.
25. Place the sample on the tarred balance and record this mass as the saturated mass (in grams) in your lab book.
26. Place the sample in a clean, labeled dish and set aside for later use.
27. Collect the saturated mass for each sample being measured.
    Note: You must TARE the balance between every sample, and periodically replace the weigh paper.
28. Record the saturated masses (in grams) in your lab book.
29. Place the samples in a clean, labeled dish and set aside for later use.
30. Once all masses are collected, enter the data into the Density Calculation Grid.

Porosity Calculations

Dry Mass = M_D
Suspended Mass = M_{Sus}
Saturated Mass = M_{Sat}
Density of Water = ρ =1 g/cm^3
Density of Ethanol = ρ = 0.789 g/cm^3

Exterior Volume = $V_E = (M_{Sat} - M_{Sus}) / \rho$
Porosity (%) = $P = [(M_{Sat} - M_D)/ V_E]*100$
Density (%) = $D = 100 - P$

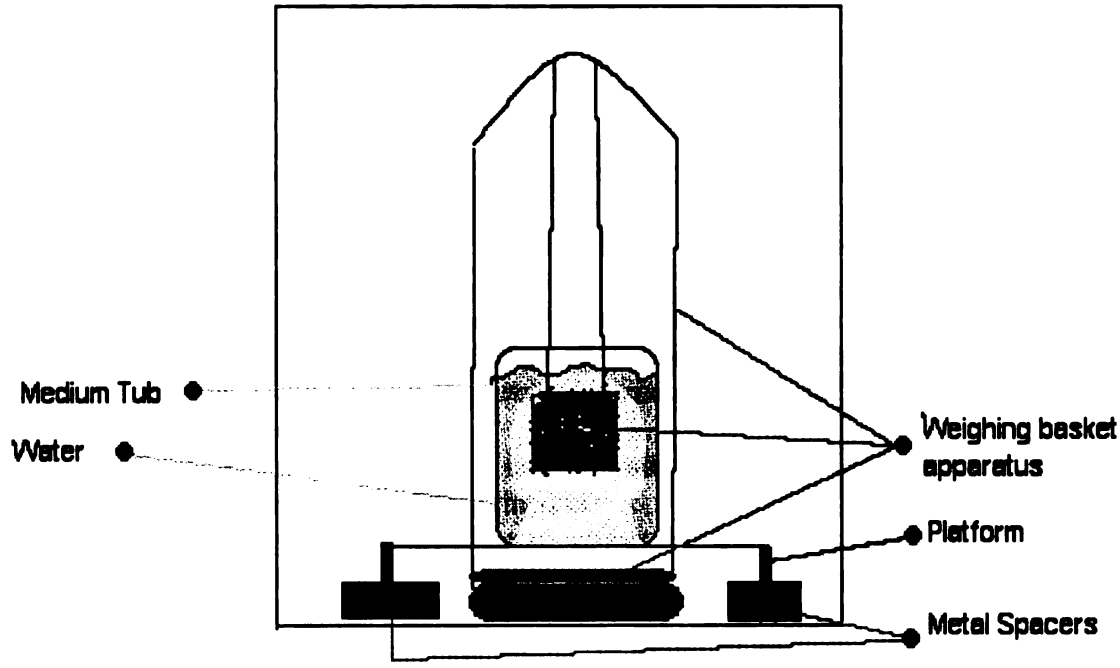

Figure 44: Suspended Mass Apparatus Setup

Operating Instructions

1. Open the top cover and verify the Manual Operation Valve is set to the "Off" position.
2. Turn on the power and control switches.
3. Turn on the cooling water, by turning the yellow handled valve behind the autoclave parallel to the copper pipe.
4. Turn on the steam inlet, by turning the blue handled valve behind the autoclave parallel to the steel pipe.
   WARNING: This pipe will become very hot when steam comes through.
   If a leak is noticeable in either the cooling pipe or steam inlet, STOP, do not go any further! Contact a senior research assistant and/or technician (Rob Selden or Tim Bender)
5. Place Nalgene tray(s) with materials to be sterilized inside of the autoclave.
6. Set the sterilize time by turning the dials.
   For specific sterilization specifications see reverse side.
7. Wait for the jacket pressure gauge to increase to 18-20 psi. (Located in the top control panel on the front of the autoclave.
   WARNING: Do not run the autoclave until this pressure stabilizes!
8. Close autoclave door tightly. (Be sure the right side is pushed in.) Crank the wheel counterclockwise until it feels snug, and then crank the wheel an extra ¼ to ½ turn.
   Do not over tighten - door will be very difficult to open after the cycle!
9. Select the cycle – Either gravity (for solids) or liquids
10. A buzzer will signify the end of the cycle, hit reset button.
    For specific drying specifications see reverse side.
11. Turn off power and control switches
12. Close the cooling water valve by turning yellow handle perpendicular to the pipe.
13. Close the steam inlet valve by turning blue handle perpendicular to pipe.
    Be careful! The pipe will be very hot and can cause serious burns!

Autoclaving Biohazardous Waste

Be sure to use an autoclavable biohazard bag

All biohazardous waste bags must be autoclaved and properly disposed of every 90 days at the latest!

1. Add 250 mL of water into each bag being autoclaved.
2. Sterilized for 60 minutes (at 121 °C and 15 psi).
3. Place bag in Nalgene tray, leaving bag open for steam to infiltrate the waste.
4. Follow sterilization procedures according to Autoclaving instructions.
5. Upon completion of sterilization, tightly seal biohazard bag and dispose of in a black opaque trash bag.

Further specifications may be found in the Biosafety Manual published by ORCBS.

Autoclaving Liquids (in bottles)

1. Fill bottle a maximum of only HALF WAY full.
2. Loosely screw on cap. (Approximately 1 to 1½ back turns from being snug.) *This creates a vent to relieve any pressure buildup during the sterilization process.*
3. Place bottle in a Nalgene tray
4. Sterilize liquids for 60 minutes (at 121 °C and 15 psi).
5. Follow sterilization procedures according to Autoclaving instructions.
6. Upon completion of sterilization, remove liquids from the autoclave.

Autoclaving Glassware - (pipettes, pasteur pipettes, bottles, beakers)
Be sure the pipettes have been washed prior to sterilization
Pipettes should be in Aluminum holders, sealed with autoclave tape
Glass pipettes can be repeatedly re-autoclaved, Pasteur pipettes are for single use

1. Place Aluminum holders in a Nalgene tray
2. Sterilize for 60 minutes (at 121 °C and 15 psi).
3. Follow sterilization procedures according to Autoclaving instructions.
4. Upon completion of sterilization, release the pressure and steam from the autoclave by opening the door[1]. Then, close the door but do not re-tighten.
5. Leave pipettes in autoclave for 2 to 3 hours after completion of sterilization cycle to evaporate off residual moisture from pipettes.

Autoclaving Pipet Tips
Pipet tips are not re-autoclaveable

1. Place bottle in a Nalgene tray
2. Sterilize for 60 minutes (at 121 °C and 15 psi).
3. Follow sterilization procedures according to Autoclaving instructions.
4. Upon completion of sterilization, release the pressure and steam from the autoclave by opening the door. Then, close the door but do not re-tighten.
5. Leave pipettes in autoclave for 2 to 3 hours after completion of sterilization cycle to evaporate off residual moisture from pipettes.

Instrument Start Up

1. Verify the server computer is on. (This computer should never be turned off.)
2. Turn on the Main Console of ESEM (green button). Press **RETURN** when prompted for a password. (If an error message concerning LANtastics appears, power console off, wait 30 seconds, then restart console.)
3. Verify the "GUN VACUUM" is better than 5.0×10^{-7} Torr.
4. In 1.0 KeV increments, turn up the accelerating voltage until the desired accelerating voltage is reached.
5. At the top of the menu, select "**GUN**" and click on "**HEAT FILAMENT**". Note: Verify emission current, 1.85 A, and ramp time, 1200 sec – Do not adjust these settings.)
6. Remove the objective aperture by turning the aperture knob fully clockwise.
7. Select "**GHOST**", and then select "**SOURCE**" in the "**GUN**" menu to view the filament image.
8. Saturate the filament by minimizing the filament image. Return to normal mode by deselecting "**SOURCE**".
9. Adjust the aperture knob until an image is visible.
10. Focus your specimen at a magnification greater than 8000X .
11. Find a convenient place on the specimen and select the "**WOBBLE**" function found in the "**COLUMN**" menu. Zero the stigmators.
12. Adjust the micrometers of the objective aperture to minimize specimen movement. Turn off the "**WOBBLE**", refocus and stigmate your image.
13. If you need to leave the ESEM for more than 45 minutes, but have not finished your session, cool the filament to 1.0 A, and place the vacuum in standby mode.

Sample Insertion and Exchange

1. Select "**STBY**" then "**VENT**" from the main menu. The chamber will vent for 90 seconds. "**ESC**" will stop the venting cycle.
2. While the stage door is open, select "**STAGE**" from the menu then click "**CALIBRATE**". The stage position will move automatically to center. Select "**Clear All**" to remove previously stored positions. Notice that "**Z Limit is Off**" message is visible in the "**STAGE**" menu now. This will change to 0.0 mm after you have adjusted the Z height of the specimen and selected "**Z SET**". The stage cannot be raised above the 0.0 mm, but can be lowered using the toggle switch. Working distance is measured in positive Z mm.

*****Note: Visibly check the working distance when you raise the specimen to avoid collision with the detector. *****

3. Insert the sample and adjust the Z height of the specimen so that the sample is 1-2 mm below the top of the stage door. This will ensure that the top of the specimen will be below the GSED detector.
4. If you accidentally hit "**HIVAC**" on the controls, don't panic, just wait 3-4 minutes until the vacuum levels reactivate. Then select "**STBY**" and proceed. If you accidentally hit the "**FLOOD**" option, just click it once more to close the valve.
5. To exchange specimens, select "**STBY**", then "**VENT**". The stage will automatically retract 10 mm in the Y-direction and lower the stage 10 mm in the Z-direction. Exchange the specimen, then select "STBY" and then select "**WET**" while holding the stage door shut.

Imaging

1. Select "**WET**" mode. Set pressure to 2.0 to 4.0 Torr.
2. Insert an appropriate objective aperture (one click counterclockwise is the 50 μm aperture followed by the 30, 20 and 10 μm apertures).
3. Increase contrast and brightness until specimen is visible. Increase scan time to 0.48 sec. to reduce the noise in the image.
4. Adjust Z-height to an appropriate working distance and focus.
5. Select "**Disk**" from the main menu. Next to "**Auto Seed**" type the root filename. The first 6 characters are used to identify your specimen, while the last two characters should be 01. The images are incremented by one automatically.
6. In the "Disk" menu, the "**SAVE DIR**" and the "**LIST DIR**" enter the appropriate directories. Note that the user directory should be added to the default E:\ESEM path.
7. To take a photo, focus the image at an appropriate magnification and depress the acquire button on the console. To save the image, select "**SAVE**" on the main menu.

Image Storage and Retrieval

1. Image storage is located on the server drive E:\ESEM. The ESEM user is solely responsible for the data. When you have finished your session, either download your files to another computer, burn the data on a CD, or FTP your files to another computer.

System Shutdown

1. When you have finished your session, remove your sample and put the chamber under vacuum. Go to standby mode.
2. Select "**COOL FILAMENT**" under the "**GUN**" menu.
3. Wait for the filament to cool, and then turn down the accelerating voltage.
4. Turn the console off.

Emergency Shutdown ****Turn the console off**

FOAM PROCESSING

The procedure details the process for foaming porous scaffolds. To foam a porous scaffold with a porosity of 27%, using the HA: KNO_3: H_2O_2 ratio of 43: 55: 2, with 30% H_2O_2 concentration. To foam a porous scaffold with a porosity of 55%, use the HA: KNO_3: H_2O_2 ratio of 36: 58: 6 with 5% H_2O_2 concentration.

All hydroxyapatite powders used were obtained from Hitemco Medical Applications (Old Bethpage, NY)

Procedure

1. Make 10^{-3}M KNO_3 foaming electrolyte in a sterile plastic bottle.
2. Verify the pH of the KNO_3 electrolyte is a neutral 7.2.
3. Clean all of the utensils, beakers, and SIL-molds according to proper lab cleaning procedure.
4. Pre-weigh the HA powder to the desired amount and place into a clean, dry beaker.
5. Add the precisely calculated quantity of the KNO_3 to the HA.
6. Mix vigorously with the flat edge of the metal spatula, until the HA is well coated and the suspension has a consistent texture.
7. Add the precisely calculated quantity of H_2O_2 to the HA suspension.
8. Mix vigorously with the flat edge of the metal spatula until mixture is homogenous.
9. Carefully spoon the foamed HA slurry into the holes of the silicon mold, manipulating the slurry to prevent and eliminate the formation of air pocket along the mold wall.
10. Place the slurry filled mold into the gravity convection oven, and dry the scaffolds for 60 minutes at 125°C.
11. Carefully remove the dried green scaffolds from the SIL-mold and place them on an alumina sintering plate for sintering.
12. Sinter the scaffolds at 1360°C for 4 hours.

HYDROGEN PEROXIDE REDUCTION TITRATION

Hydrogen Peroxide (H_2O_2) decomposes after standing for a period of time. The shelf life the H_2O_2 is extended if stored under refrigerated conditions[1], as opposed to room temperature. Time is not the only factor in the decomposition of H_2O_2. The breakdown of the H_2O_2 is accelerated by *almost anything*, including traces of dirt, heat, water, oxygen and traces of heavy metal ions.

$$2H_2O_2(l) \rightarrow 2H_2O + O_2(g)$$

Equation 8: Decomposition of H_2O_2

Hydrogen peroxide is a weak, colorless acid that freezes at –0.43°C, boils at 150.2°C and has a density of 1.4425 g/mL (at 25°C)

Experimental handling procedures for H_2O_2

1. Non-refrigerated H_2O_2 should only be stored for 2 to 3 months (recommended) unless the H_2O_2 purity has been verified.
2. Verify the purity of the H_2O_2 on a regular basis to insure you are using the assumed concentration.
3. Always make diluted concentrations of the H_2O_2 the day you plan to use them, and do not use if they have been stored for longer than 5 days (unless purity has been verified).
4. Use a vented amber bottle for storing diluted concentrations of the H_2O_2.

Warning: H_2O_2 is a strong oxidizer. Even low concentrations as low as 20% will eat skin, eyes and respiratory tract. Do not inhale and take proper safety precautions.

Procedure: Verifying the Purity of H_2O_2 by Reduction Titration[2]

1. Accurately weight 1mL of H_2O_2 in a tared 100mL volumetric flask.
2. Add distilled H_2O to the H_2O_2 up to the 100mL mark.
3. Mix thoroughly.
4. Fill the buret with 0.1N potassium permanganate, making note of the initial volume of the potassium permanganate in the buret.
5. In a separate beaker, take 20mL of the dilute H_2O_2 and add 20mL diluted sulfuric acid[3]
6. Slowly, titrate the H_2O_2/sulfuric acid mixture with 0.1N potassium permanganate.
7. The potassium permanganate will react with the H_2O_2, when the reaction stops the beaker contents will turn pinkish-purple. STOP Titrating!

---

[1] At this time, the H_2O_2 used in the lab is not stored under refrigerated conditions. In the future, if the H_2O_2 is to be stored in this manner, special considerations must be accounted for.

[2] Reagent Chemicals 8th Edition, American Chemical Society Specifications

[3] To make the diluted sulfuric acid, dilute 1mL of concentrated sulfuric acid into 15mL of distilled H_2O. Remember, "If your doin' what ya ought-a, add the acid to the water."

Procedure: Verifying the Purity of H_2O_2 by Reduction Titration (continued)

8. Once the reaction has occurred. Make note of the final volume of potassium permanganate remaining in the buret.
9. Using the Hydrogen Peroxide Titration Excel Program enter in the mass amount of 1mL of the H_2O_2 under investigation, and the initial and final volumes of the potassium permanganate in the buret.
10. Manual calculation of the accurate percentage of the H_2O_2 can be made using the calculations listed below.

Calculations

M = Mass of 1mL of H_2O_2

V_i = Initial volume of potassium permanganate in the buret

V_f = Final volume of potassium permanganate in the buret

$V = V_f - V_i$

1mL 0.1N Potassium Permanganate = 0.0017 g H_2O_2

$$\frac{M(g\,H_2O_2)}{1mL} = \frac{x(g\,H_2O_2)}{0.2(mL)}$$

$$x = M * 0.2 \rightarrow \textit{Expected amount of } H_2O_2 \textit{ at } 100\% \textit{ concentration}$$

$$V * 1 = V * 0.0017 \rightarrow 0.2mL \textit{ of the total } 100\% \textit{ concentration}$$

$$\frac{V * 0.0017}{x} \times 100 = \textit{Actual percent concentration of the } H_2O_2$$

SPECTROPHOTOMETER INSTRUCTIONS

The spectrophotometer is useful for absorbance assays: AP Quantification, Crystal violet, Calcium/phosphorous determination

Procedure:

1. Turn on power switch located in the back on the right hand side; allow the computer to warm up.
2. Enter 1 (Basic Modes)
3. Enter 1 (Absorbance)
4. Enter the sample number and select F3 if ok.
5. Enter the desired wavelength and select F3 if ok.
6. Load the cuvettes into spectrophotometer. (The blue holder is for the initial reference)
7. Press the green button to take measurements.
8. Reload spectrophotometer if needed for additional samples (Start with the blue holder) and select F3.
9. Press the green button to take measurements.
10. When all measurements have been taken, press the red button to exit and F2 to confirm.

Surface Area (SA) of the Dense Scaffolds

* SA is approximated to the SA of a cylinder

$$SA = 2(\pi(D/2)^2) + (2\pi(D/2) * t$$

Equation 9

SA of the Porous Foamed Scaffolds

1. Obtain an average weight (W) for all like scaffolds.

2. Obtain an average diameter (D) and an average thickness (t) for all like scaffolds.

3. Cumulative Pore Area (CPA) is obtained during mercury porosimetry and for porous HA approximates 0.0035 m^2/g.

4. Calculate the external SA based on the SA equation for dense scaffolds.

5. Determine the pore surface area (PA) of the pores greater than 10μm diameter.

$$PA = CPA * W$$

Equation 10

6. Total the external SA and the pore surface area for the total speciman surface area (TSA).

$$TSA = SA + PA$$

Equation 11

SURFACE ROUGHNESS

The arithmetic mean surface roughness (R_a) is obtained using Hommel RC4000 profilometer (Hommelwerke) in the MSU Forestry department (Professor Pascal). The Turbo Roughness T8000 from Hommel is limited in the type of surface being analyzed. Only dense materials can be measured for surface roughness. Porous scaffolds are problematic in that the pores will catch on the profilometry probe.

Procedure:

Selecting the Measuring Program

1. Open the Turbo Roughness T8000 program and turn on the profilometer.
2. Select the *Options* button on the top menu.
3. Select *Mode*, then *Measurement + Evaluation*
4. Select *Measuring program*, then select *Open* and finally select *Rebecca.*

Note: The parameters of this program have already been set up, suitable for measuring the surface roughness of HA. The parameters are listed below.

Parameters:

1. Lt = 10 mm
2. Vt = 0.5 mm/s
3. Lc = 2 mm
4. Range μm = ± 80
5. Using MI 4777 Filter
6. 4000 values measure

Calibrating the Program

1. Hit the *F6* button on the toolbar to calibrate. (The F6 key on the keyboard also works.)
2. Place the sample on the table and slowly raise or lower the wand to adjust.
3. Calibrate by adjusting the top screw adjustment. This makes fine adjustments; a little turn can go a long way. Calibrate to zero, or a close as possible within the range of ± 0.500.
4. Once you are within the range, removed your hands from the machine and table and ensure the wand stabilizes.
5. Zero the system by hitting the *F8* button on the toolbar.

Collecting Data

1. Start data collection by hitting the *F5* button.
2. The profilometry scan will take just a few seconds. When completed, another screen will pop up; hit *OK,* then enter in a file name for the scan.
3. Hit *OK*
4. Exit the measuring system by hitting *F12*. This takes you to the main menu of the program and displays the results of the scans.

Saving Profiles

1. To save, first select the profile. Go to *Profile* on the top menu.
2. Select *Examine Profile.*

Saving Profiles (continued)

3. Using the mouse, highlight the profile to save. **Only one can be selected at a time.**
4. Hit *OK.*

Note: At this point, you have only selected a profile; you have not saved a profile.

5. Go to *Profile* on the top menu.
6. Select *Export Profile to ASCII.*
7. Hit *OK.*
8. The profile is now saved. Repeat this for each set of surface profiles collected.

Opening Profiles

* ASCII profiles can be opened in Microsoft Excel.

POWDER X-RAY DIFFRACTION

Room 401 Chemistry Building- Rui Huang, 355-9715 x 382 or huangru@msu.edu

Computer Signup for Powder XRD

1. Telnet to period.cem.msu.edu using a Mac (Apple) or Vax computer (PC computer will not work, use the SUN computers to signup if in the EB)
2. Login **period** with the user name **powder** and the password **signup.**
3. At the prompt, type **set term/vt100.**
4. Signing up for time
5. To sign up for time within the current two weeks, type: **edit signup.cur.**
6. To sign up for time in advanced (future two weeks), type: **edit signup.adv.**
7. To enter the edit mode, type **c.**
8. Enter your time in the appropriate area, and then press **control-z** to save the changes.
9. Type exit to return.
10. To view the type schedule, type: **type signup.cur,** or **type signup.adv.**
11. Only one person can log in at a time, and there is a 15 minute time limit for users.
12. During the prime hours (Monday – Friday, 8am to 5pm) there is a two hour limit. There is no time for all other time.

Operating Instructions for the X-Ray Diffractometer

Turning the X-Rays On

1. Check that the flow meters and temperature indicators on the Haskris heat exchanger (Gray Box) indicate values within the acceptable ranges.
2. Ensure that the *TMP* is operating, by checking that the green TMP run light is on, and the three green vacuum lights are on.
3. Verify the *Tube Voltage* is set to its minimum value (20kV) and the *Tube Current* is set to its minimum value (10mA) according to the gray dials.
4. Verify that the doors to the radiation enclosure are closed.
5. Verify that the shutter for both side 1 and side 2 are set to *Close.*
6. Depress the white *T-Rev* button on the X-Ray generator control panel to start the anode rotating. Visually check that the target is revolving. The ready light should come on. If not, recheck steps 3 and 4.
7. Depress the white *X-Ray On* button to obtain X-Rays. The ready light will go off.
8. Slowly increase the *Tube Voltage* to 45kV, by first turning the inside gray dial, and then the outside gray dial.
9. Slowly increase the *Tube Current* to 100mA in the same manner.
10. Turn the shutter control switch (2) to the *EXT* position before starting the scan.

****Note: Be sure the monitor the vacuum level by the meter to be sure the vacuum is good during this period of time.**

Turning the X-Rays Off

1. Slowly turn the *tube current* back to 10mA, step by step.
2. Slowly turn the *tube voltage* back to 20kV, step by step.
3. Wait for a few minutes (approximately 5 – 10 minutes) to allow the diffractometer to stabilize.
4. Depress the red *X-Ray Off* button to turn the X-Rays off.

Setup for the Diffractometer Control Computer

1. Check that the X-Rays are turn on, if not return to "Operating the Powder X-Ray Diffractometer" procedure.
2. If in DOS prompt, and the screen reads A:\), type **c:\ menu** to enter the program. If the screen reads C:\), type **menu** to enter the program.
3. Choose "Qualitative Program", and return to get to the next page.
4. Choose "Qualitative Data Collection" and return to go on.
5. Select the right side and hit return.
6. Choose "Set Datum", to verify the goniometer's zero. (For up to date specifications, refer to the bulletin board in the XRD room.) Hit **Esc** to return back to the previous page.
7. Choose "Set HV/PHA" to verify the goniometer calibration and parameters of the detector. (For up to date specifications, refer to the bulletin board in the XRD room.) Hit **Esc** to return to the previous page.
8. Check the parameters in the "Set Parameters".
   KV = 45, mA = 100, 2 Theta minimum = 0.5, 2 Theta maximum = 140.0
   Focus = Line, Target = Cu, Monochromatic = Yes
9. Choose "Set Scan Conditions" to set the scan conditions for your experiment. Hit **Enter** to make changes to the scanning conditions, and **Control-z** to save updated scanning conditions and to continue.
10. Choose "Measurement" to set up the data file. Make sure you are saving to a floppy disc on the A:\ drive.
11. Once you have verified where the data will be saved, a file log will appear on the screen. Hit **Enter** once and type in sample identification information. Hit **Enter** twice more until the scanning conditions appear on the bottom screen. **Control-z** will save any changed.
12. Hit **Enter** to specify not to list the resulting data to printer.
13. Use **Esc** to exit the data collection program, and return back to the main screen. Select "Real Time Data Display" to monitor the data collection process.
14. While collecting data, use **Esc** key to exit from "Real Time Data Display" or, hit **S** at any time during the collection to STOP collecting data.
15. Once the data collection has all finished, hit **S** for *screen dump* and save the collected data to the floppy disk.
16. **Esc** back to the main menu and select "Chart" program to plot spectrum once the scan has completed.

****Note: Use Ctrl-Z (or sometimes enter) to save and go forward within the program, and Esc to go backwards.**

REFERENCES

1. LeGeros RZ. Properties of Osteoconductive Biomaterials: Calcium Phosphates. *Clin Orthop* 2002(395): 81-98.

2. Ratner BD, Hoffman AS, Schoen FJ, Lemons JE: Biomaterials Science: An Introduction to Materials in Medicine. San Diego: Academic Press, 1996; 484.

3. Finkemeier CG. Current Concepts Review: Bone-Grafting and Bone-Grafting Substitutes. *J Bone and Joint Surg* 2002; 84A(3): 454-464.

4. Burg KJ, Porter S, Kellam JF. Biomaterial Developments for Bone Tissue Engineering. *Biomaterials* 2000; 21(23): 2347-59.

5. Cook SD, Baffes GC, Wolfe MW, Sampath TK, Rueger DC, Whitecloud TS, 3rd. The Effect of Recombinant Human Osteogenic Protein-1 on Healing of Large Segmental Bone Defects. *J Bone Joint Surg Am* 1994; 76(6): 827-38.

6. Zioupos P, Currey JD, Hamer AJ. The Role of Collagen in the Declining Mechanical Properties of Aging Human Cortical Bone. *J Biomed Mater Res* 1999; 45(2): 108-16.

7. Burstein AH, Reilly DT, Martens M. Aging of Bone Tissue: Mechanical Properties. *J Bone Joint Surg Am* 1976; 58(1): 82-6.

8. Zioupos P, Currey JD. Changes in the Stiffness, Strength, and Toughness of Human Cortical Bone with Age. *Bone* 1998; 22(1): 57-66.

9. Hench LL. Bioceramics. *J Am Ceram Soc* 1998; 81(7): 1705-1728.

10. Davies JE: Bone Engineering. Toronto, Canada: em squared Inc, 2000; 656.

11. Anselme K. Osteoblast Adhesion on Biomaterials. *Biomaterials* 2000; 21(7): 667-81.

12. Zhang Y, Zhang M. Three-Dimensional Macroporous Calcium Phosphate Bioceramics with Nested Chitosan Sponges for Load-Bearing Bone Implants. *J Biomed Mater Res* 2002; 61(1): 1-8.

13. de Groot K: Effect of Porosity and Physicochemical Properties on the Stability, Resorption and Strength of Calcium Phosphate Ceramics. In: Ducheyne P, Lemons JE, eds. Bioceramics: Material Characteristic Versus *In Vivo* Behavior, vol 523. New York, 1988; 227-234.

14. Malik MA, Puleo DA, Bizios R, Doremus RH. Osteoblasts on Hydroxyapatite, Alumina and Bone Surfaces *In Vitro*: Morphology During the First 2 H of Attachment. *Biomaterials* 1992; 13(2): 123-8.

15. Cerroni L, Filocamo R, Fabbri M, Piconi C, Caropreso S, Condo S. Growth of Osteoblast-Like Cells on Porous Hydroxyapatite Ceramics: An *In Vitro* Study. *Biomolecular Engineering* 2002; 19: 119-124.

16. Manjubala I, Sivakumar M, Sureshkumar RV, Sastry TP. Bioactivity and Osseointegration Study of Calcium Phosphate Ceramic of Different Chemical Composition. *J Biomed Mater Res* 2002; 63(2): 200-8.

17. Yuan H, Yang Z, Li Y, Zhang X, de Bruijn JD, de Groot K. Osteoinduction by Calcium Phosphate Biomaterials. *Journal of Materials Science: Materials in Medicine* 1998; 9: 723-726.

18. Tampieri A, Celotti G, Sprio S, Delcogliano A, Franzese S. Porosity-Graded Hydroxyapatite Ceramics to Replace Natural Bone. *Biomaterials* 2001; 22(11): 1365-70.

19. Fisher-Brandies E, Dietert E, Bauer G. Zur Morpholgie Synthetischer Calcium-Phosphat-Kermiken *In Vitro. Z. Zahnarztl Implantol* 1987: 87.

20. Krajewski A, Ravaglioli A. A Physico-Chemical Study of Crystal Growth of Hydroxyapatite Bioceramic. *Biomaterials* 1981; 2(2): 105-11.

21. Yuan H, Kurashina K, de Bruijn JD, Li Y, de Groot K, Zhang X. A Preliminary Study on Osteoinduction of Two Kinds of Calcium Phosphate Ceramics. *Biomaterials* 1999; 20(19): 1799-806.

22. Hing K, Best SM, Bonfield W. Characterization of Porous Hydroxyapatite. *J Mater Sci: Mater Med* 1999; 10: 135-145.

23. Sun J-S, Tsuang Y-H, Liao C-J, Liu H-C, Hang Y-S, Lin F-H. The Effects of Calcium Phosphate Particles on the Growth of Osteoblasts. *J Biomed Mater Res* 1997; 37: 324-334.

24. Webster TJ, Ergun C, Doremus RH, Siegel RW, Bizios R. Enhanced Osteoclast-Like Cell Functions on Nanophase Ceramics. *Biomaterials* 2001; 22(11): 1327-33.

25. de Bruijn JD, van Blitterswijk CA, Davies JE. Initial Bone Matrix Formation at the Hydroxyapatite Interface *In Vivo. J Biomed Mater Res* 1995; 29(1): 89-99.

26. Shu J, McMullen R, Baumann M, McCabe L. Hydroxyapatite Accelerates Differentiation and Suppresses Growth of MC3T3-E1 Osteoblasts. *J Biomed Mater Res* 2003; 67A: 1196-1204.

27. Li SH, De Wijn JR, Layrolle P, de Groot K. Synthesis of Macroporous Hydroxyapatite Scaffolds for Bone Tissue Engineering. *J Biomed Mater Res* 2002; 61(1): 109-20.

28. Tamai N, Myoui A, Tomita T, Nakase T, Tanaka J, Ochi T, Yoshikawa H. Novel Hydroxyapatite Ceramics with an Interconnective Porous Structure Exhibit Superior Osteoconduction *In Vivo*. *J Biomed Mater Res* 2002; 59(1): 110-7.

29. Sepulveda P, Bressiani AH, Bressiani JC, Meseguer L, Konig B, Jr. *In Vivo* Evaluation of Hydroxyapatite Foams. *J Biomed Mater Res* 2002; 62(4): 587-92.

30. Engin NO, Tas AC. Preparation of Porous $Ca_{10}(Po_4)_6(OH)_2$ and B-$Ca_3(Po_4)_2$ Bioceramics. *J Am Ceram Soc* 2000; 83(7): 1581-1584.

31. Muller BP, Ensslen S, Dott W, Hollender J. Improved Sample Preparation of Biomaterials for *In Vitro* Genotoxicity Testing Using Reference Materials. *J Biomed Mater Res* 2002; 61(1): 83-90.

32. Kilpadi KL, Chang PL, Bellis SL. Hydroxylapatite Binds More Serum Proteins, Purified Integrins, and Osteoblast Precursor Cells Than Titanium or Steel. *J Biomed Mater Res* 2001; 57(2): 258-67.

33. Koutsopoulos s. Synthesis and Characterization of Hydroxyapatite Crystals: A Review Study on the Analytical Methods. *J Biomed Mater Res* 2002; 62: 600-612.

34. Dong J, Kojima H, Uemura T, Kikuchi M, Tateishi T, Tanaka J. *In Vivo* Evaluation of a Novel Porous Hydroxyapatite to Sustain Osteogenesis of Transplanted Bone Marrow-Derived Osteoblastic Cells. *J Biomed Mater Res* 2001; 57(2): 208-16.

35. Layrolle P, Ito A, Tateishi T. Sol-Gel Synthesis of Amorphous Calcium Phosphate and Sintering into Microporous Hydroxyapatite Bioceramics. *J Am Ceram Soc* 1998; 81(6): 1421-1428.

36. Jarcho M. HA Synthesis and Characterization in Dense Polycrystalline Form. *J Mater Sci* 1976; 11: 2027-2035.

37. Bilezikian J, Raisz L, Rodan GA: Principles of Bone Biology. 2nd ed. New York: Academic Press, 2002.

38. Wang JY, Wicklund BH, Gustilo RB, Tsukayama DT. Titanium, Chromium and Cobalt Ions Modulate the Release of Bone-Associated Cytokines by Human Monocytes/Macrophages *In Vitro*. *Biomaterials* 1996; 17(23): 2233-40.

39. Hench LL. Bioceramics: From Concept to Clinic. *J Am Ceram Soc* 1991; 74: 1487-1510.

40. Klein C, de Groot K, Driessen A, Ven der Lubbe H. Interaction of Biodegradable Beta-Whitlockite with Bone Tissue: An *In Vivo* Study. *Biomaterials* 1985; 6: 189-.

41. Lu J, Flautre B, Anselme K, Hardouin P, Gallur A, Descamps M, Thierry B. Role of Interconnections in Porous Bioceramics on Bone Recolonization *In Vitro* and *In Vivo*. *J Mater Sci: Mater Med* 1999; 10: 111-120.

42. Tancred DC, McCormack BA, Carr AJ. A Quantitative Study of the Sintering and Mechanical Properties of Hydroxyapatite/Phosphate Glass Composites. *Biomaterials* 1998; 19(19): 1735-43.

43. Flautre B, Descamps M, Delecourt C, Blary M. Porous HA Ceramic for Bone Replacement: Role of the Pores and Interconnections - Experimental Study in the Rabbit. *J Mater Sci: Mater Med* 2001; 12: 679-682.

44. Boyan BD, Hummert T, Dean DD, Schwartz Z. Role of Material Surfaces in Regulating Bone and Cartilage Cell Response. *Biomaterials* 1996; 17: 137-146.

45. Hing K, Best S, Tanner K, Bonfield W, Revell P. Quantification of Bone Ingrowth within Bone-Derived Porous Hydroxyapatite Implants of Varying Density. *J Mater Sci: Mater Med* 1999; 10: 663-670.

46. Clarke K, Graves S, Wong A, Triffitt J, Francis M, Czernuszka J. Investigation into the Formation and Mechanical Properties of a Bioactive Material Based on Collagen and Calcium Phosphate. *J Mater Sci: Mater Med* 1993; 4: 107-110.

47. Park J, Lakes R: Biomaterials. New York: Plenum Press, 1992.

48. Jarcho M. Calcium Phosphate Ceramics as Hard Tissue Prosthetics. *Clin Ortho and Rel Res* 1981; 157: 259-278.

49. Metsger D, Rieger M, Foreman D. Mechanical Properties of Sintered Hydroxyapatite and Tricalcium Phosphate Ceramic. *J Mater Sci: Mater Med* 1999; 10: 9-17.

50. Barralet J, Best SM, Bonfield W. Effect of Sintering Parameters on the Density and Microstructure of Carbonate Hydroxyapatite. *J Mater Sci: Mater Med* 2000; 11: 719-724.

51. Tancred DC, Carr AJ, McCormack BA. The Sintering and Mechanical Behavior of Hydroxyapatite with Bioglass Additions. *J Mater Sci: Mater Med* 2001; 12: 81-93.

52. Xu H, Quinn J. Whisker-Reinforced Bioactive Composites Containing Calcium Phosphate Cement Filters: Effects of Filler Ratio and Surface Treatments on Mechanical Properties. *J Biomed Mater Res* 2001; 57: 165-174.

53. Roeder R, Sproul M, Turner C: Hydroxyapatite Whiskers Provide Enhanced, Bone-Like Mechanical Properties in Reinforced Polymer Composites. 48th Annual Meeting of the Orthopaedic Research Society.

54. Koerten HK, van der Meulen J. Degradation of Calcium Phosphate Ceramics. *J Biomed Mater Res* 1999; 44(1): 78-86.

55. Doi Y, Shibutani T, Moriwaki Y, Kajimoto T, Iwayama Y. Sintered Carbonate Apatites as Bioresorbable Bone Substitutes. *J Biomed Mater Res* 1998; 39: 603-610.

56. Lu J, Descamps M, Dejou J, Koubi G, Hardouin P, Lemaitre J, Proust JP. The Biodegradation Mechanism of Calcium Phosphate Biomaterials in Bone. *J Biomed Mater Res* 2002; 63(4): 408-12.

57. Wiltfang J, Merten HA, Schlegel KA, Schultze-Mosgau S, Kloss FR, Rupprecht S, Kessler P. Degradation Characteristics of Alpha and Beta Tri-Calcium-Phosphate (TCP) in Minipigs. *J Biomed Mater Res* 2002; 63(2): 115-21.

58. Ito A, Kawamura H, Miyakawa S, Layrolle P, Kanzaki N, Treboux G, Onuma K, Tsutsumi S. Resorbability and Solubility of Zinc-Containing Tricalcium Phosphate. *J Biomed Mater Res* 2002; 60(2): 224-31.

59. Anselme K, Bigerelle M, Noel B, Dufresne E, Judas D, Iost A, Hardouin P. Qualitative and Quantitative Study of Human Osteoblast Adhesion on Materials with Various Surface Roughnesses. *J Biomed Mater Res* 2000; 49: 155-166.

60. Takebe J, Champagne C, Offenbacher S, Ishibashi K, Cooper L. Titanium Surface Topography Alters Cell Shape and Nodulates Bone Morphogenetic Protein 2 Expression in the J774a.1 Macrophage Cell Line. *J Biomed Mater Res* 2003; 64A: 207-216.

61. Buser D, Schenk R, Steinemann S, Fiorellini J, Fox J, Stich H. Influence of Surface Characteristics on Bone Integration of Titanium Implants. A Histomorphometric Study in Miniature Pigs. *J Biomed Mater Res* 1991; 25: 889-902.

62. Deligianni DD, Katsala ND, Koutsoukos PG, Missirlis YF. Effect of Surface Roughness of Hydroxyapatite on Human Bone Marron Cell Adhesion, Proliferation, Differentiation and Detachment Strength. *Biomaterials* 2001; 22: 87-96.

63. Perizzolo D, Lacefield WR, Brunette DM. Interaction between Topography and Coating in the Formation of Bone Nodules in Culture for Hydroxyapatite- and Titanium-Coated Micromachined Surfaces. *J Biomed Mater Res* 2001; 56(4): 494-503.

64. Wong M, Eulenberger J, Schenk R, Hunziker E. Effect of Surface Topology on the Osseointegration of Implant Materials in Trabecular Bone. *J Biomed Mater Res* 1995; 29(12): 1567-75.

65. Boyan BD, Batzer R, Kieswetter K, Liu Y, Cochran DL, Szmuckler-Moncler S, Dean DD, Schwartz Z. Titanium Surface Roughness Alters Responsiveness of MG63

Osteoblast-Like Cells to 1 Alpha,25-(OH)2d3. *J Biomed Mater Res* 1998; 39(1): 77-85.

66. Bannister S, Lohmann C, Liu Y, Sylvia V, Cochran D, Dean D, Boyan B, Schwartz Z. Shear Force Modulates Osteoblast Response to Surface Roughness. *J Biomed Mater Res* 2002; 60: 167-174.

67. Schwartz Z, Lohmann C, Vocke A, Sylvia V, Cochran D, Dean D, Boyan B. Osteoblast Response to Titanium Surface Roughness and $1\alpha,25\text{-}(OH)_2d_3$ Is Mediated through the Mitogen-Activated Protein Kinase (Mapk) Pathway. *J Biomed Mater Res* 2001; 56: 417-426.

68. Kieswetter K, Schwartz Z, Hummert T, Cochran D, Simpson J, Dean D, Boyan B. Surface Roughness Modulates the Local Production of Growth Factors and Cytokines by Osteoblast-Like MG63 Cells. *J Biomed Mater Res* 1996; 32: 55-63.

69. Suzuki T, Yamamoto T, Toriyama M, Nishizawa K, Yokogawa Y, Mucalo MR, Kawamoto Y, Nagata F, Kameyama T. Surface Instability of Calcium Phosphate Ceramics in Tissue Culture Medium and the Effect on Adhesion and Growth of Anchorage-Dependent Animal Cell. *J Biomed Mater Res* 1997; 34: 507-517.

70. Sisk M, Lohmann C, Cochran DL, Sylvia V, Simpson J, Dean DD, Boyan BD, Schwartz Z. Inhibition of Cyclooxygenase by Indomethacin Modulates Osteoblast Response to Titanium Surface Roughness in a Time-Dependent Manner. *Clin Oral Implants Res* 2001; 12: 52-61.

71. Webster TJ, Ergun C, Doremus RH, Seigel RW, Bizios R. Specific Proteins Mediated Enhanced Osteoblast Adhesion on Nanophase Ceramics. *J Biomed Mater Res* 2000; 51: 475-483.

72. Anselme K, Bigerelle M, Noel B, Iost A, Hardouin P. Effect of Grooved Titanium Substratum on Human Osteoblastic Cell Growth. *J Biomed Mater Res* 2002; 60: 529-540.

73. Lu X, Leng Y. Quantitative Analysis of Osteoblast Behavior on Microgrooved Hydroxyapatite and Titanium Substrata. *J Biomed Mater Res* 2002; 66A: 677-687.

74. Wojciak-Stothard B, Curtis A, Monaghan W, MacDonald K, Wilkinson C. Guidance and Activation of Murine Macrophages by Nanometric Scale Topography. *Exp Cell Res* 1996; 223: 426-435.

75. Brunette DM, Chehroudi B. The Effects of the Surface Topography of Micromachined Titanium Substrata on Cell Behavior *In Vitro* and *In Vivo*. *J Biomech Eng* 1999; 121: 49-57.

76. Curtis A, Wilkinson C. Reactions of Cells to Topography. *J Biomater Sci Polymer Edn* 1998; 9(12): 1313-1329.

77. Curtis A, Wilkinson C. Review: Topographical Control of Cells. *Biomaterials* 1997; 18(24): 1573-1583.

78. Kowalchuk R, Pollack S, Corcoran T. Zeta Potential of Bone Fromo Particle Electrophoresis: Solution Composition and Kinetic Effects. *J Biomed Mater Res* 1995; 29: 47-57.

79. Pollack S. Bioelectric Properties of Bone. *Clin Orthop North Am* 1984; 15: 3-14.

80. Kitano T, Ohashi H, Kadoya Y, Kobayashi A, Yutani Y, Yamano Y. Measurements of Zeta Potentials of Particulate Biomaterials in Protein-Rich Hyaluronan Solution with Changes in pH and Protein Constituents. *J Biomed Mater Res* 1998; 42: 453-457.

81. Ducheyne P, Kim C, Pollack S. The Effect of Phase Differences on the Time-Dependent Variation of the Zeta Potential of Hydroxyapatite. *J Biomed Mater Res* 1992; 26: 147-168.

82. Hyakuna K, Yamamuro T, Kotoura Y, Oka M, Nakamura T, Kitsugi T, Kokubo T, Kushitani H. Surface Reactions of Calcium Phosphate Ceramics to Various Solutions. *J Biomed Mater Res* 1990; 24(4): 471-88.

83. Cozens-Roberts C, Quinn J, Lauffenburger D. Receptor-Mediated Adhesions Phenomena. *Biophys J* 1990; 58: 107-125.

84. Ueshima M, Tanaka S, Nakamura S, Yamashita K. Manipulation of Bacterial Adhesion and Proliferation by Surface Charges of Electrically Polarized Hydroxyapatite. *J Biomed Mater Res* 2002; 60(4): 578-84.

85. Ohgaki M, Kizuki T, Katsura M, Yamashita K. Manipulation of Selective Cell Adhesion and Growth by Surface Charges of Electrically Polarized Hydroxyapatite. *J Biomed Mater Res* 2001; 57: 366-373.

86. Kobayashi T, Nakamura S, Yamashita K. Enhanced Osteobonding by Negative Surface Charges of Electrically Polarized Hydroxyapatite. *J Biomed Mater Res* 2001; 57(4): 477-84.

87. Sudo H, Kodama H-A, Amagai Y, Yamamoto S, Kasai S. *In Vitro* Differentiation and Calcification in a New Clonal Osteogenic Cell Line Derived from Newborn Mouse Calvaria. *J Cell Biol* 1983; 96: 191-198.

88. Nakamura S, Kobayashi T, Yamashita K. Extended Bioactivity in the Proximity of Hydroxyapatite Ceramic Surfaces Induced by Polarization Charges. *J Biomed Mater Res* 2002; 61(4): 593-9.

89. Klein C, Driessen A, de Groot K, van den Hooff A. Biodegradation Behavior of Various Calcium Phosphate Materials in Bone Tissue. *J Biomed Mater Res* 1983; 17: 769-784.

90. Kalfas I. Principles of Bone Healing. *Neurosurgery Focus* 2001; 10: 1-4.

91. Morrison S, Shah N, Anderson D. Regulatory Mechanisms in Stem Cell Biology. *Cell* 1997; 88: 287-298.

92. Boo JS, Yamada Y, Okazaki Y, Hibino Y, Okada K, Hata K, Yoshikawa T, Sugiura Y, Ueda M. Tissue-Engineered Bone Using Mesenchymal Stem Cells and a Biodegradable Scaffold. *J Craniofac Surg* 2002; 13(2): 231-9; discussion 240-3.

93. Yoshikawa T, Ohgushi H, Nakajima H, Yamada E, Ichijima K, Tamai S, Ohta T. *In Vivo* Osteogenic Durability of Cultured Bone in Porous Ceramics: A Novel Method for Autogenous Bone Graft Substitution. *Transplantation* 2000; 69(1): 128-34.

94. Itoh D, Yoneda S, Kuroda S, Konda H, Umezawa A, Ohya K, Ohyama T, Kasugai S. Enhancement of Osteogenesis on Hydroxyapatite Surface Coated with Synthetic Peptide (Eeeeeeeprgdt) *In Vitro. J Biomed Mater Res* 2002; 62: 292-298.

95. Peterson WJ, Tachiki KH, Yamaguchi DT. Extracellular Matrix Alters the Relationship between Tritiated Thymidine Incorporation and Proliferation of MC3T3-E1 Cells During Osteogenesis *In Vitro. Cell Prolif* 2002; 35(1): 9-22.

96. Deckers M, van Bezooijen R, van de Horst G, Hoogendam J, van der Bent C, Papapoulos S, Lowik C. Bone Morphogenetic Proteins Stimulate Angiogenesis through Osteoblast-Derived Vascular Endothelial Growth Factor A. *Endocrinology* 2002; 143: 1545-1553.

97. Mayr-Wohlfart U, Fiedler F, Gunther K, Puhl W, Kessler S. Proliferation and Differentiation Rates of a Human Osteoblast-Like Cell Line (SaOS-2) in Contact with Different Bone Substitute Materials. *J Biomed Mater Res* 2001; 57: 132-139.

98. Basso N, Heersche J. Characteristics of *In Vitro* Osteoblastic Cell Loading Models. *Bone* 2002; 30: 347-351.

99. Hunter A, Archer C, Walker P, Blunn G. Attachment and Proliferation of Osteoblasts and Fibroblasts on Biomaterials for Orthopaedic Use. *Biomaterials* 1995; 16(4): 287-295.

100. Spitzer RS, Perka C, Lindenhayn K, Zippel H. Matrix Engineering for Osteogenic Differentiation of Rabbit Periosteal Cells Using Alpha-Tricalcium Phosphate Particles in a Three-Dimensional Fibrin Culture. *J Biomed Mater Res* 2002; 59(4): 690-6.

101. Yoshida K, Bessho K, Fujimura K, Konishi Y, Kusumoto K, Ogawa Y, Iizuka T. Enhancement by Recombinant Human Bone Morphogenetic Protein-2 of Bone Formation by Means of Porous Hydroxapatite in Mandibular Bone Defects. *J Dent Res* 1999; 79: 1505-1510.

102. Webster TJ, Ergun C, Doremus RH, Bizios R. Hydroxyapatite with Substituted Magnesium, Zinc, Cadmium, and Yttrium. Ii. Mechanisms of Osteoblast Adhesion. *J Biomed Mater Res* 2002; 59: 312-317.

103. Goodman M, Bhumralkar M, Jefferson E, Kwak J, Locradi E. Collagen Mimetics. *Biopoly* 1998; 47: 127-142.

104. Ferrera D, Poggi S, Biassoni C, Dickson GR, Astigiano S, Barbieri O, Favre A, Franzi AT, Strangio A, Federici A, Manduca P. Three-Dimensional Cultures of Normal Human Osteoblasts: Proliferation and Differentiation Potential *In Vitro* and Upon Ectopic Implantation in Nude Mice. *Bone* 2002; 30(5): 718-25.

105. Horwitz AF. Integrins and Health. *Sci Am* 1997; 276(5): 68-75.

106. Doi Y, Iwanaga H, Shibutani T, Moriwaki Y, Iwayama Y. Osteoclastic Responses to Various Calcium Phosphates in Cell Cultures. *J Biomed Mater Res* 1999; 47(3): 424-33.

107. Harada S, Rodan SB, Rodan GA. Expression and Regulation of Vascular Endothelial Growth Factor in Osteoblasts. *Clin Orthop* 1995(313): 76-80.

108. de Groot K. Application of Porous Bioceramics in Surgery. *Mat Tech* 1993; 8: 12-15.

109. Arita I, Castano V, Wilkinson D. Synthesis and Processing of Hydroxyapatite Ceramic Tapes with Controlled Porosity. *J Mater Sci: Mater Med* 1995; 6: 19-23.

110. Smith R, Sambrook R, Binner J: Novel Processing of Foam Ceramics. Material Research Society, 1995.

111. Ryshkewitch E. Compression Strength of Porous Sintered Alumina and Zirconia. *J Am Ceram Soc* 1953; 36: 65-68.

112. Liu D. Fabrication of Hydroxyapatite Ceramic with Controlled Porosity. *J Mater Sci: Mater Med* 1997; 8: 227.

113. Callister WD: Materials Science and Engineering, An Introduction, 4th ed. New York: John Wiley & Sons, Inc., 1997.

114. Yang Z, Yuan H, Zou P, Tong W, Qu S, Zhang X. Osteogenic Responses to Extraskeletally Implanted Synthetic Porous Calcium Phosphate Ceramics: An Early Stage Histomorphological Study in Dogs. *J Mater Sci: Mater Med* 1997; 8: 697-701.

115. Hignite M, Crimp M: A Novel Processing Method for the Fabrication of Porous Ceramics for Applications as Bone Replacements. CIMTEC World Forum on New Materials, 1998.

116. Garofalo E: HA Particle Size Data Results and Discussion. Old Bethpage, NY: Hitemco Medical Applications / IMR Test Labs, 2003.

117. Gadaleta S, Paschalis E, Camacho N, Betts F, Mendelhson R, Boskey A: Fourier Transfrom Infrared Spectroscopy of Synthethic and Biological Apatites. In: Amjad Z, ed. Mineral Scale Formation and Inhibition. New York: Plenum Press, 1995; 283-294.

118. Fowler B. Infrared Studies of Apatite. I. Vibrational Assignments for Calcium, Strontium, and Barium Hydroxyapatites Utilizing Isotopic Substitution. *Inorg Chem* 1974; 13: 194-207.

119. Klee W, Engel G. Infrared Spectra of the Phosphate Ions in Various Apatites. *J Inorg Nucl Chem* 1970; 32: 1837-1843.

120. Ishikawa K, Ducheyne P, Radin S. Determination of the Ca/P Ratio in Calcium-Deficient Hydroxyapatite Using X-Ray Diffraction Analysis. *J Mater Sci: Mater Med* 1993; 4: 165-168.

121. Baddiel C, Berry E. Spectra-Structure Correlations in Hydroxyapatite and Fluorapatite. *Spectrochim Acta A* 1966; 22(1407-1416).

122. Barnard AJ, Desai KD, Fletcher JP, Hale JR, Halpern BD, Jamieson NC, Juvet RS, Link RA, McBride LC, Mehta RV, Moody JR, Pietrzykowski AD, Pouchert CJ, Rao JM, Simon NS, Strengerr VA, Strauss CM, Tuthill SM, Walthall FG, Wantz RH, Wilkins DH, Wilson CM, Lowery C, Bouis PA: Reagent Chemicals: American Chemical Society Specifications. 8th ed. Washington DC: American Chemical Society, 1993; 376-378.

123. de Groot K, Klein C, Wolke J, de Blieck-Hogervorst J: Chemistry of Calcium Phosphate Bioceramics. In: Yamamuro T, Hench LL, Wilson J, eds. Crc Handbook of Bioactive Ceramics, vol II. Boca Raton, FL: CRC Press, 1990; 3-15.

124. Bouler JM, LeGeros RZ, Daculsi G. Biphasic Calcium Phosphates: Influence of Three Synthesis Parameters on the HA/Beta-TCP Ratio. *J Biomed Mater Res* 2000; 51(4): 680-4.

125. Smith I, McCabe L, Baumann M, Griffin M: MC3T3-E1 Are a Suitable Substitute for Primary OBs in Terms of Zeta-Potential Analysis of HA and Beta-TCP *In Vitro*. 7th World Biomaterials Congress, Sydney Australia, May 17 - 21, 2004, 2004.

126. Mosmann T. Rapid Colorimetric Assay for Cellular Growth and Survival: Application to Proliferation and Cytotoxicity Assays. *J Immuno Method* 1983; 65(1-2): 55-63.

127. Okajima T, Nakamura K, Zhang H, Ling N, Tanabe T, Yasuda T, Rosenfeld R. Sensitive Colorimetric Bioassayss for Insulin-Like Growth Factor (Igf)

Stimulation of Cell Proliferation and Glucose Consumption: Use in Studies of Igf Analogs. *Endocrinology* 1992; 130(4): 2201-2212.

128. Cortizo A, Bruzzone L, Molinuevo S, Etcheverry S. A Possible Role of Oxidative Stress in the Vanadium-Induced Cytotoxicity in the MC3T3-E1 Osteoblast and Umr106 Osteosarcoma Cell Lines. *Toxicology* 2000; 147: 89-99.

129. Salice V, Cortizo A, Gomez Dumm C, Etcheverry S. Tyrosine Phosphorylation and Morphological Transformation Inducted by Four Vandium Compounds on MC3T3-E1 Cells. *Molecular and Cellular Biochemistry* 1999; 198: 119-128.

130. McAlinden M, Wilson D. Comparison of Cancellous Bone-Derived Cell Proliferation in Autologous Human and Fetal Bovine Serum. *Cell Transplantation* 2000; 9: 445-451.

131. Fedarko N, D'Avis P, Frazier C, Burrill M, Fergusson V, Tayback M, Sponseller P, Shapiro J. Cell Proliferation of Human Fibroblasts and Osteoblasts in Osteogenesis Imperfecta: Influence of Age. *J Bone Miner Res* 1995; 10(11): 1705-1712.

132. Labarca C, Paigen K. A Simple, Rapid and Sensitive DNA Assay Procedure. *Analytical Biochemistry* 1980; 102: 344-352.

133. Barsoum M: Fundamentals of Ceramics: McGraw-Hill, 1997 Materials Science and Engineering Series).

134. Hatano K, Inoue H, Kojo T, Matsunaga T, Tsujisawa T, Uchiyama C, Uchida Y. Effect of Surface Roughness on Proliferation and Alkaline Phosphatase Expression of Rat Calvarial Cells Cultured on Polystyrene. *Bone* 1999; 25(4): 439-45.

135. Dox I, Melloni B, Eisner G: The Harpercollins Illustrated Medical Dictionary. New York, NY: Harper Perennial, 1993.

136. Rosa A, Beloti M, van Noort R. Osteoblastic Differentiation of Cultured Rat Bone Marrow Cells on Hydroxyapatite with Different Surface Topography. *Dental Materials* 2003; 19: 768-772.

137. Freshney R: Culture of Animal Cells: A Manual of Basic Techniques. New York: Alan R. Liss, Inc, 1987.

138. Bahrami S, Stratmann U, Wiesmann HP, Mokrys K, Bruckner P, Szuwart T. Periosteally Derived Osteoblast-Like Cells Differentiate into Chondrocytes in Suspension Culture in Agarose. *Anat Rec* 2000; 259(2): 124-30.

139. Ehara A, Ogata K, Imazato S, Ebisu S, Nakano T, Umakoshi Y. Effects of Alpha-TCP and Tetra-TCP on MC3T3-E1 Proliferation and Differentiation and Mineralization. *Biomaterials* 2003; 24: 831-836.

140. Sun JS, Lui H, Chang W, Li J, Lin FH, Tai H. Influence of Hydroxyapatite Particle Size on Bone Cell Activity: An *In Vitro* Study. *J Biomed Mater Res* 1998; 39: 390-397.

141. Deng X, Hao J, Wang C. Preparation and Mechanical Properties of Nanocomposites of Poly(D,L-Lactide) with Ca-Deficient Hydroxyapatite Nanocrystals. *Biomaterials* 2001; 22(21): 2867-73.

142. Cuneyt Tas A, Korkusuz F, Timucin M, Akkas N. An Investigation of the Chemical Synthesis and High-Temperature Sintering Behaviour of Calcium Hydroxyapatite (Ha) and Tricalcium Phosphate (TCP) Bioceramics. *J Mater Sci: Mater Med* 1997; 8: 91-96.

143. Rey C, Shimizu M, Collins B, Glimcher MJ. Resolution-Enhanced Fourier-Transform Infrared Spectroscopy Study of the Environment of Phosphate Ion in the Early Deposits of a Solid Phase of Calcium Phosphate in Bone and Enamel and Their Evolution with Age: 2. Investigations in the *V*3 Po4 Domain. *Calcif Tissue Int* 1991; 49: 383-388.

144. Andrade JC, Camilli JA, Kawachi EY, Bertran CA. Behavior of Dense and Porous Hydroxyapatite Implants and Tissue Response in Rat Femoral Defects. *J Biomed Mater Res* 2002; 62(1): 30-6.

145. Roy M, Nishimoto S, Rho J, Bhattacharya S, Lin J, Pharr G. Correlations between Osteocalcin Content, Degree of Mineralization, and Mechanical Properties of *C. Carpio* Rib Bone. *J Biomed Mater Res* 2000; 54: 547-553.

146. Xie J, Baumann M, McCabe L. Osteoblasts Respond to Hydroxyapatite Surfaces with Immediate Changes in Gene Expression. *J Biomed Mater Res* 2004; 71A (1):108.

147. Sikavitsas V, Bancroft G, Mikos A. Formation of Three-Dimensional Cell/Polymer Constructs for Bone Tissue Engineering in a Spinner Flask and a Rotating Wall Vessel Bioreactor. *J Biomed Mater Res* 2002; 32: 136.

148. Bancroft G, Sikavitsas V, Mikos A. Design of a Flow Perfusion Bioreactor System for Bone Tissue-Engineering Applications. *Tissue Engineering* 2003; 9(3): 549-554.

149. Sikavitsas V, Temenoff J, Mikos A. Biomaterials and Bone Mechanotranduction. *Biomaterials* 2001; 22: 2581.

150. Hillsley M, Frangos J. Bone Tissue Engineering: The Role of Interstitial Fluid Flow. *Biotech. Bioeng* 1994; 43: 573.

151. Mueller S, Mizuno S, Gerstenfeld LC, Glowacki J. Medium Perfusion Enhances Osteogenesis by Murine Osteosarcoma Cells in Three-Dimensional Collagen Sponges. *J Bone Miner Res* 1999; 12: 2118 - 2126.

152. Botchwey E, Pollack S, Levine E, Laurencin C. Bone Tissue Engineering in a Rotating Bioreactor Using a Microcarrier Matrix System. *J Biomed Mater Res* 2001; 55: 242.

153. Kurashina K, Kurita H, Wu Q, Ohtsuka A, Kobayashi H. Ectopic Osteogenesis with Biphasic Ceramics of Hydroxyapatite and Tricalcium Phosphate in Rabbits. *Biomaterials* 2002; 23: 407-412.

154. Hashimoto-Uoshima M, Ishibashi I, Kinoshita A. Clinical and Histological Observation on Replacement of Biphasic Calcium Phosphate in Bone Tissue in Monkeys. *Int J Periodont Res Dent* 1995; 15: 204-213.

155. Alam M, Asahina I, Ohmamiuda K, Takashashi K, Yokota S, Enomoto S. Evaluation of Ceramics Composed of Difference Hydroxyapatite to Tricalcium Phosphate Ratios as Carriers for RhBMP-2. *Biomaterials* 2001; 22: 1643-1651.

156. Malard O, Bouler JM, Guicheuz J, Heymann D, Pilet P, Coquard C, Daculsi G. Influence of Biphasic Calcium Phosphate Granulometry on Bone Ingrowth, Ceramic Resportion, and Inflammatory Reactions: Preliminarly *In Vitro* and *In Vivo* Study. *J Biomed Mater Res* 1998; 46(1): 103-111.

157. Christel P, Vert M, Chabot F, Abols Y, Leary J: Polylactic Acid for Intramedullary Plugging. In: Ducheyne P, ed. Biomaterials and Biomechanics. Amsterdam: Elsevier Science Publishers, 1983.

158. Matsusue Y, Yamamuro T, Oka M, Shikinami Y, Hyon S-H, Ikada Y. *In Vitro* and *In Vivo* Studies on Bioabsorbable Ultra High Strength Poly(L-Lactide) Rods. *J Biomed Mater Res* 1992; 26: 1553-1567.

159. Case ED: Laser Scanning Confocal Microscopy in Materials Science and Technology. Current Issues in Multidisciplinary Microscopy Research and Education: Kluwer Academic Publisher, submitted March 2004.

160. Draeger DJ, Case ED. Engineering the Surface Texture and Shape of Channels in Ceramic Substrates. *Materials Science and Engineering* 2003; B97(1): 94-105.

MICHIGAN STATE UNIVERSITY LIBRARIES
3 1293 02732 4874